

Mesoporous Germanium Layer Formation by Electrochemical Etching

Dissertation
zur Erlangung des akademischen Grades
Doktor der Ingenieurwissenschaften
(Dr.-Ing.)
der Technischen Fakultät
der Christian-Albrechts-Universität zu Kiel

Garralaga Rojas, Enrique José

Licenciado en Ciencias Físicas, MSc. Physik, European MSc.
in Renewable Energies (specialisation Photovoltaics)

2010

Erste Gutachter: Prof. Dr. Helmut Föll
Zweite Gutachter: Prof. Dr. Rainer Adlung
Dritte Gutachter: Prof. Dr. Lorenz Kienle
Tag der Promotion: Freitag, den 16 Juli 2010

Try not to become a man of success, but rather try to become a man of value.

[Albert Einstein]

Contents

1	Introduction	3
2	Semiconductors and electrolytes	5
2.1	Introduction to semiconductors	5
2.1.1	Band theory	6
2.1.2	Fermi energy level	9
2.1.3	Doping in semiconductors	10
2.2	General aspects of semiconductor electrochemistry	12
2.2.1	Semiconductor-metal interface	12
2.2.2	Electrolytes	13
2.2.3	Semiconductor-electrolyte interface	15
2.3	Summary and conclusions to Chapter 2	18
3	Basics on porous Si	19
3.1	Porous silicon	19
3.1.1	Current-voltage curves and electrochemical reactions	20
3.1.2	Pore wall passivation mechanisms	22
3.1.3	Effect of the etching conditions	22
3.1.4	Porous layer annealing and reorganization	23
3.2	The Porous Silicon Process	23
3.3	Summary and conclusions to Chapter 3	25
4	Porous Ge fabrication and characterization	27
4.1	Electrochemical etching setup and working procedure	27
4.2	Annealing setup	31
4.3	Porous layer analysis and characterization	31
4.3.1	Microscopy analysis	31
4.3.2	Porosity calculation	32
4.3.3	Etching rate calculation	33
4.3.4	Valence number calculation	34
4.3.5	Micro Raman spectroscopy	34
4.4	Summary and conclusions to Chapter 4	35
5	Electrochemical etching of Ge	37
5.1	Review on porous germanium	37
5.2	Mesoporous Ge layer formation	38

5.2.1	Etching rates	40
5.2.2	Substrate usage	44
5.2.3	Layer porosity	46
5.3	Mesoporous Ge double- and multilayers	49
5.4	Macropore formation	51
5.5	Summary and conclusions to Chapter 5	54
6	Theoretical model for anodic etching of Ge	57
6.1	Theoretical background	57
6.2	Experimental observations	58
6.3	Anodic dissolution model	60
6.4	Results and model interpretation	62
6.5	Valence number calculation	64
6.6	Valence band simulation	65
6.7	HF electrolytes for mesoporous formation in Ge	67
6.8	Summary and conclusions to Chapter 6	69
7	Annealing of porous Ge	71
7.1	Introduction to Ge annealing	71
7.2	Annealing in hydrogen atmosphere	72
7.3	Annealing in other atmospheres	74
7.3.1	Annealing in argon atmosphere	74
7.3.2	Annealing in forming gas atmosphere	75
7.3.3	Annealing in nitrogen atmosphere	77
7.4	Lift-off of single porous layers	77
7.5	Surface characterization	77
7.6	MOCVD epitaxial growth of III-V compounds on reorganized PGe	80
7.7	Outlook and conclusions to Chapter 7	82
8	Summary and conclusions	83
A	Mesoporous GaAs	85
A.1	Experimental	85
A.2	Mesoporous single- and double layer formation	86
A.3	Porous GaAs layer characterization	88
A.4	Summary and conclusions to Appendix A	91
B	Mesoporous Si (100) with 6° off towards (111)	93
B.1	Experimental	93
B.2	Porous double layer formation and characterization	94
B.3	Summary and conclusions to Appendix B	99
C	Mixture of electrolytes	101

Chapter 1

Introduction

Weight reduction of multi-junction III-V semiconductor solar cells is an important budget issue for space applications. Typically, space solar cells are epitaxially formed on a Ge or GaAs substrate wafer. The substrate material determines the lattice constant of the stack, provides mechanical stability during the cell process, and serves as bottom cell [1]. The substrate wafer is typically more than 100 μm thick for reasons of mechanical stability during cell processing, whereas a few μm thickness are sufficient for the bottom cell to match the photogenerated currents in the top and middle cells and not to be current limiting. Unnecessarily heavy substrate wafers hence reduce the available payload for satellite missions.

There are several techniques that permit the production of very-thin lightweight highly-efficient space solar cells. Ge or GaAs substrates are commonly removed by chemical wet etching or grinding, which reduce weight but have the disadvantage that the substrate wafer is lost for further use [2]. Separating the electrically active solar cells from their substrates by a lift-off process could save the substrate and reduce costs. The application of a layer transfer process for multi-junction III-V semiconductor space solar cells is hence of main interest for all space agencies.

Lift-off processes based on epitaxial growth of the absorber layer onto a porous-etched substrate already exist for the fabrication of monocrystalline silicon solar cells. Brendel demonstrated the so-called Porous Silicon (PSI) process for the production of monocrystalline thin-film Si solar cells [3]. This method uses a double layer of mesoporous Si formed by means of electrochemical etching: A mesoporous layer with low porosity at the surface of the substrate is used as a seed layer for the Si epitaxy, while a buried high porosity layer is used as a pre-determined breaking-point.

The formation of porous germanium (PGe) has been not intensively studied and only a few investigations were published [4]-[24]. This work focuses on the fabrication and characterization of porous germanium layers by means of electrochemical etching. The thesis evaluates the potential applications of porous Ge layers for the fabrication of very-thin space solar cells.

Chapter 2 provides the reader with the theoretical background of solid-state physics and electrochemistry of semiconductors necessary for understanding this work.

Chapter 3 explains the electrochemical formation of porous silicon and the PSI process for the fabrication of thin monocrystalline solar cells. These two concepts motivate the work and serve as reference for their implementation in germanium.

Chapter 4 presents the electrochemical etching and annealing setup used as well as various porous layer characterization methods used in this investigation.

Chapter 5 studies the formation of PGe layers by electrochemical etching. Mesoporous germanium single- and multi-layers form by using highly concentrated hydrofluoric acid (HF) electrolytes. Constant electropolishing accompanies porous layer formation. The surface passivates with hydrogen by alternating the etching bias from anodic to cathodic, hence avoiding substrate thinning.

Chapter 6 presents a model for the dissolution mechanism of Ge in highly concentrated HF-based electrolytes that considers chemical and electrochemical dissolution of Ge with different electron valence numbers. The experimental observations and measurements validate the model. The simulation of band bending withing the Si and Ge electrodes at the semiconductor/electrolyte interface presents differences and suggests the cause for the leakage current proposed in the literature [9],[14], which might be responsible of the electropolishing.

Chapter 7 analyses the reorganization of porous Ge layers in different gas atmospheres at temperatures beneath the melting point. The annealing of PGe layers in nitrogen, argon, or forming gas atmospheres yields a reorganized and oxidized unstable porous layer. Annealing in hydrogen prevents oxidation and yields reorganized and stable porous layers. Lift-off of mesoporous single layers and epitaxial growth of III-V compounds on top of reorganized and stable PGe layers is demonstrated.

Finally, Chapter 8 presents the conclusions and the outlook of this work. Annexes A and B present two potential alternatives to mesoporous Ge for the fabrication of very-thin space solar cells that have been additionally investigated in this work: Mesoporous p-type GaAs and mesoporous Si (100) with a miscut of 6° towards (111).

Chapter 2

Semiconductors and electrolytes

The reader has to be acquainted with the basic principles of solid state physics, semiconductors and electrochemistry in order to achieve a complete understanding of the investigations hereby presented. The phenomena that take place at the semiconductor-electrolyte interface must be described in order to understand porous layer formation by means of electrochemical etching. The following chapter presents a brief introduction to semiconductors, band theory, and behavior of electrons and holes within a semiconductor, followed by a description of the semiconductor-metal and semiconductor-electrolyte interfaces and their electronic characteristics. The standard books of solid state physics [25],[26] and electrochemistry [27],[28] present a more detailed discussion of the theory.

2.1 Introduction to semiconductors

The properties of solid state materials are understood by examining their electronic structure. The ability to conduct electricity is commonly used to classify them. According to the Electric Conductivity σ [Scm^{-1}], solid state materials classify into three major groups [29]: Isolators, semiconductors and metals. Table 2.1 shows typical conductivity values for each group.

Material	Conductivity σ [Scm^{-1}]
Isolator	$10^{-18} - 10^{-8}$
Semiconductor	$10^{-8} - 10^4$
Metal	$10^4 - 10^6$

Table 2.1: Materials and conductivity

Germanium is a semiconductor with a conductivity that typically varies in the $10^{-2} - 10^2 Scm^{-1}$ range. The conductivity strongly depends on the temperature and doping concentration, i.e. concentration of foreign atoms added specifically. The addition of dopants changes the value of the resistivity up to several orders of magnitude, taking values in the $10^{-4} - 10^4$ range. Doped semiconductor materials are highly interesting for the manufacture of various electronic devices and solar cells due to their high tuneability.

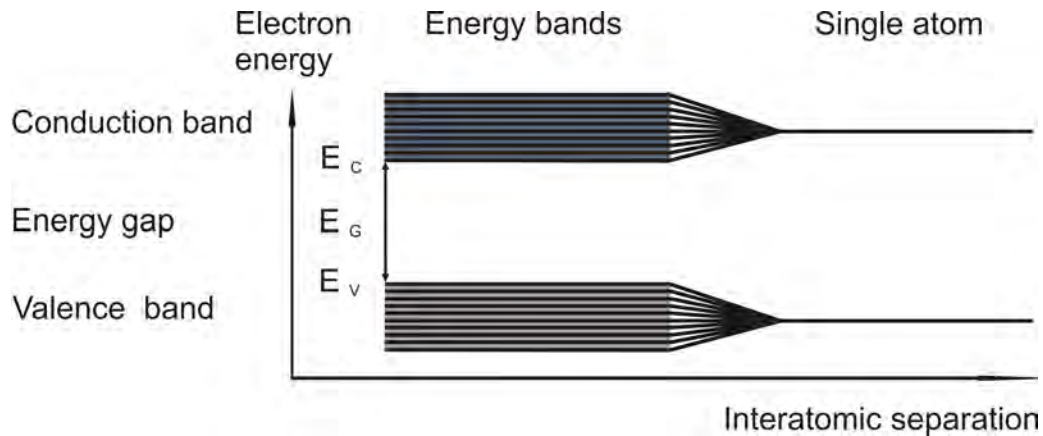


Figure 2.1: Generation of bands in solids from atomic orbitals of single atoms.

2.1.1 Band theory

There are different theories that describe the behavior of materials. The free electron gas model describes some thermal properties of the materials, i.e. heat capacity. However, this model has some deficiencies, since it is not able to discern between metals, semiconductors, and insulators. The band theory is able to classify the materials and simultaneously explain their electronic properties.

Each single atom has discrete atomic orbitals or energy levels which are likely to be occupied by electrons. According to the Pauli's exclusion principle, each energy level hosts a maximum of two electrons with opposite spins. If more atoms are brought together and form a solid, the orbitals overlap, valence electrons interact, and a quasi-continuous energy spectrum, commonly called energy band, forms. Electrons are therefore arranged within energy bands rather than considering discrete energy levels. Electrons tend to occupy the lowest energy levels. The last occupied band is called Valence Band (*VB*) and the first unoccupied band is called Conduction Band (*CB*). The energy difference between the highest energy level of the valence band E_V and the lowest energy level of the conduction band E_C is called Energy Band Gap $E_G = E_C - E_V$. Figure 2.1 shows schematically the variation of the energy levels in dependence of the interatomic separation.

The size of the band gap determines the conductivity and type of material. Materials are classified according to the band gap as shown in Figure 2.2. Semiconductors typically show a band gap in a range of 0.3 to 3 eV. The band gap of semiconductors depends on the external temperature. Ge, Si and GaAs have a band gap of 0.66 eV, 1.12 eV, and 1.42 eV respectively for an external temperature of 300 K. Insulators show band gaps larger than 3 eV. Metals have a band gap lower than 0.3 eV or even show overlap of both conduction and valence bands.

The movement of charge carriers through solid materials requires that electrons occupy free or partially filled orbitals. The valence band is generally filled out and hence occurs at the conduction band, where lots of unoccupied orbitals are still available. Insulators have such a large band gap that electrons cannot excite from VB to the CB and are hence not electrically conductive. On the contrary, the CB and VB overlap in the metal case. As a consequence, electrons coming from the VB migrate to the CB

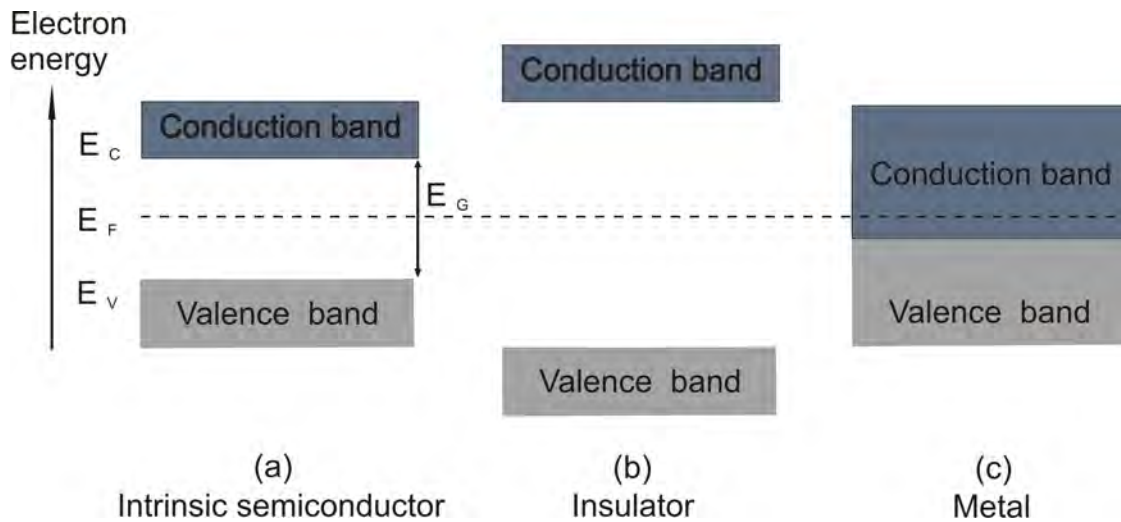


Figure 2.2: Energy band diagrams of (a) an intrinsic semiconductor, (b) insulator, and (c) metal.

and metals are therefore highly conductive. Semiconductors have small band gaps and electrons present at the VB move into the CB if an excitation is applied. Electrons are excited thermally, electrically, or photonically. As electrons migrate from the VB to the CB, they leave a positively charged carrier at the VB called Hole h^+ . The current in semiconductors has therefore two components: Electrons and holes. Both are mobile and have opposite charge. Figure 2.3 shows the electron conduction process within a semiconductor.

The band gap energy determines the light absorption within a semiconductor. Incoming light with a wavelength shorter than the Threshold Wavelength λ is absorbed and generates charge carriers, whereas light with longer wavelengths passes unimpeded throughout the semiconductor. Exceeding absorbed energy transforms into thermal energy and is lost. The adsorption wavelength of a semiconductor is given in nanometers by the following equation:

$$\lambda \leq \frac{1240}{E_G} \quad (2.1)$$

Semiconductors additionally classify according to the band gap type. Photon absorption in indirect band gap semiconductors requires a phonon, i.e. a quantized lattice vibration with a determined energy, which compensates the change in the crystal momentum that is necessary for absorption. On the contrary, direct band gap semiconductors do not need a phonon, and photons with energy equal to the band gap are absorbed and create electron-hole pairs without momentum change. Figure 2.4 shows schematically the differences between direct and indirect semiconductors. Ge and Si are indirect semiconductors and GaAs is a direct semiconductor.

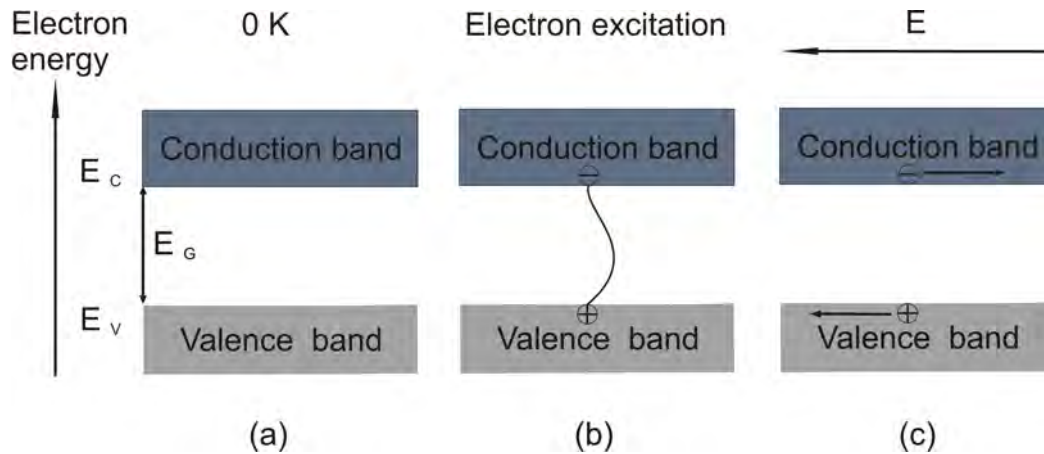


Figure 2.3: Electron conduction. (a) At 0 K, the valence band is complete while the conduction band is empty. (b) An electron is excited, e.g. thermally by increasing temperature, and is able to migrate from the valence band into the conduction band, creating a hole in the valence band. (c) An external field is able to separate the charges.

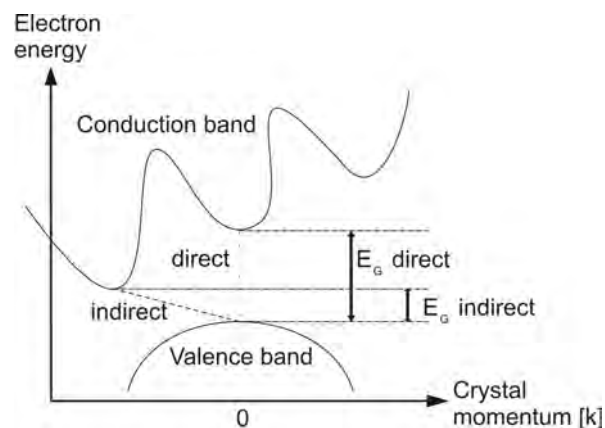


Figure 2.4: Adsorption in direct semiconductors does not imply a change in the crystal momentum. Indirect semiconductors require a phonon additionally in order to adsorb a photon and compensate the change in the crystal momentum.

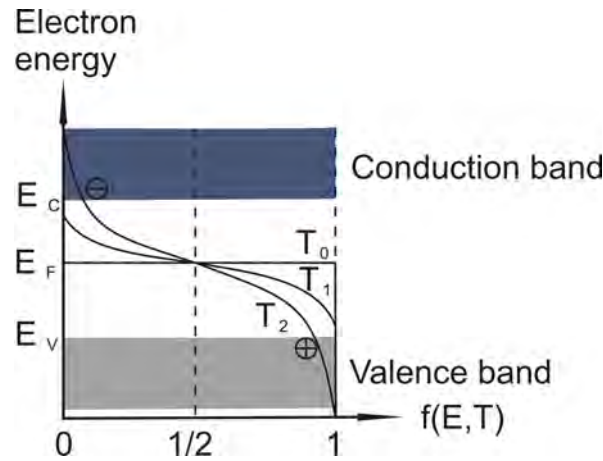


Figure 2.5: Fermi-Dirac distribution in an intrinsic semiconductor. At a temperature $T_0 = 0$ K, the function $f(E, T)$ has a step-like shape with the step at the value E_F . By increasing the temperature, the occupation probability $f(E, T) > 0$ varies for energy values $E > E_F$. In the case of sufficient energy $E > E_C$, electrons coming from VB become thermally excited and create holes at the VB.

2.1.2 Fermi energy level

Electrons and holes are fermions and obey the Pauli's exclusion principle that states that only a quantum state is occupied at a given time. Fermi-Dirac statistics are thus applicable and the Fermi-Dirac distribution function hence describes the probability of a fermion of having an energy E . The Fermi-Dirac distribution function depends on the energy of the particle and the temperature.

$$f(E, T) = \frac{1}{\exp\left(\frac{E - E_F}{kT}\right) + 1} \quad (2.2)$$

E_F represents the Fermi energy level, k is the Boltzmann's constant, and T is the temperature. E_F represents the energy value at which the occupation probability is equal to $1/2$. At absolute zero, all available energy states below the level E_F are filled up with electrons and E_F is equal to the E_V . The occupation probability increases by rising the temperature. Some electrons hence excite to energy levels above the Fermi level. Figure 2.5 shows the Fermi-Dirac distribution function for an intrinsic semiconductor.

Holes are positively charged carriers produced by the migration of an electron from the valence band to the conduction band and behave similarly to a positive charged electron. Intrinsic semiconductors are materials that do not contain impurities. The electron density hence equals the hole density since the activation of an electron from the VB to the CB yields a free electron in the CB as well as a free hole in the VB. The Fermi level is thus located in the mid-point of the band gap. The Concentration of Electrons n_0 and Holes p_0 is calculated using the mass action law shown in equation 2.3 for non-degenerate semiconductors in thermal equilibrium. The charge carrier concentration depends on the energy band gap and the absolute temperature.

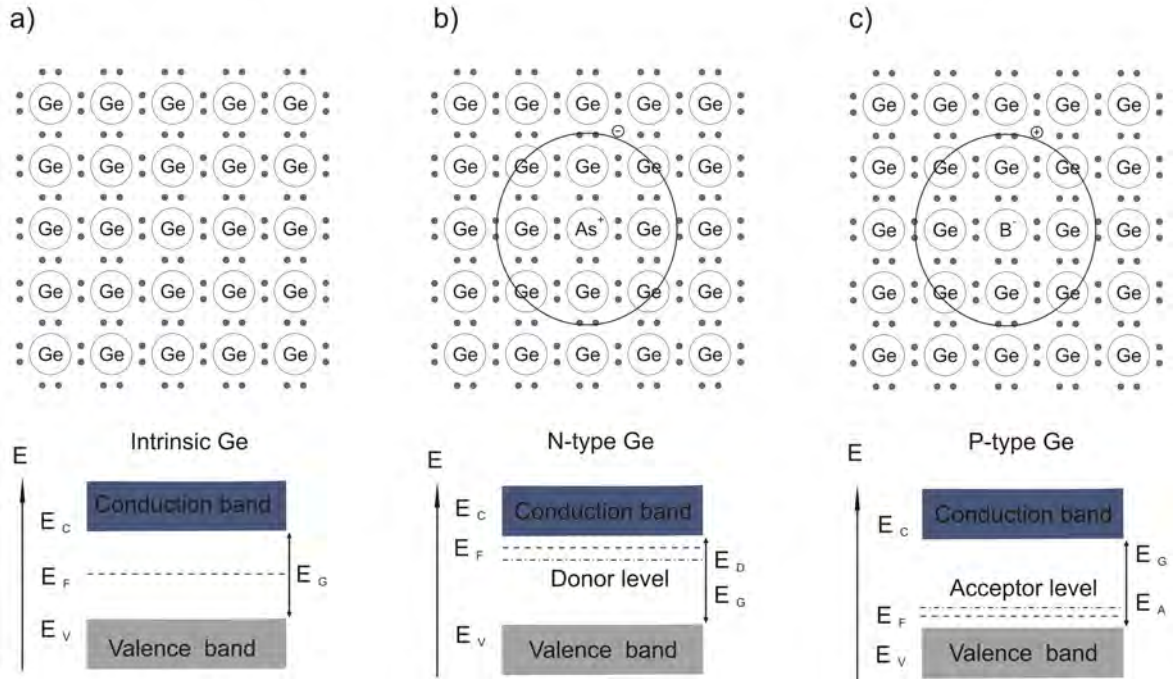


Figure 2.6: Representation of a) intrinsic, b) n-type, and c) p-type semiconductor. The Fermi level depends on the doping level. E_F is located in the middle of the band gap for the intrinsic semiconductor. For n-type semiconductors, the Fermi level is located just above the donor level and for p-type semiconductors, below the acceptor level.

$$n_0 \cdot p_0 = n_i^2 = N_c \cdot N_V \cdot e^{\frac{(E_V - E_C)}{kT}} = N_c \cdot N_V \cdot e^{\frac{-E_G}{kT}} \quad (2.3)$$

Equation 2.4 gives the conductivity of a material, where q is the Elementary Charge and μ_e and μ_h are the Mobilities of Electrons and Holes respectively. Changes in the conductivity of semiconductors are interesting for the industry. They are obtained by varying the amount of charge carriers available. Thermal activation, illumination, and doping of the substrates affect charge carrier concentration.

$$\sigma = q^- n_0 \mu_e + q^+ p_0 \mu_h \quad (2.4)$$

2.1.3 Doping in semiconductors

Intrinsic semiconductors have the same concentration of electrons n_0 and holes p_0 . The number of mobile charge carriers is limited because thermal activation is the only mechanism for carrier generation. The conductivity is thus strongly dependent on the temperature and becomes difficult to control. The development of components in the microelectronic and photovoltaic industry requires controlled variations in the conductivity of the semiconductors. This is obtained by adding in a controlled manner tiny fractions of atoms ($10^{15} - 10^{19}$ atoms/cm³) of various materials, so-called dopants,

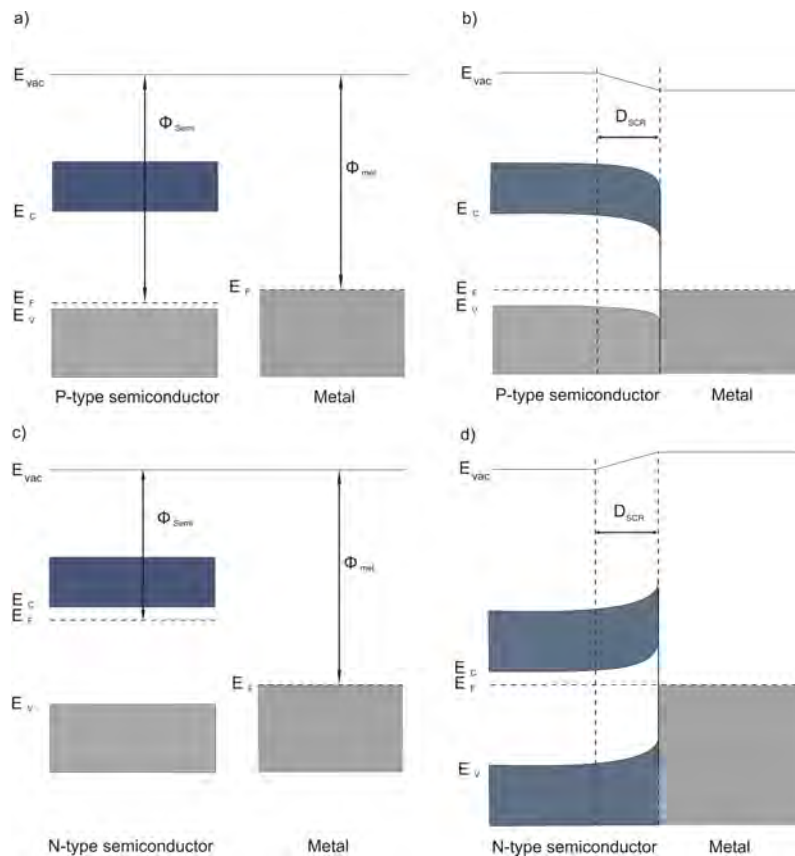


Figure 2.7: Representation of a semiconductor-metal contact. a) Differences between a p-type semiconductor and a metal. b) p-type semiconductor contacted to a metal. Band bending occurs and a space charge region appears. c) Differences between a n-type semiconductor and a metal. d) n-type semiconductor contacted to a metal. Space charge region is formed, but band bending is opposite to p-type

to the semiconductors. The impurities bring additional charge carriers which help to change deliberately the conductivity in a controlled manner.

Doping atoms for Si or Ge are typically elements from the III and V groups. Boron and phosphor are dopants for p- and n-type doping respectively. Phosphor atoms have five valence electrons and donate an electron at room temperature to the conduction band due to the small energetic difference. Supplementary electrons create an additional energy level a few meV beneath the CB, also called donor level. The conductivity is hence dominated by the amount of electrons and is called n-type. In n-type semiconductors, the amount of electrons dominates the conductivity. The electrons and holes are respectively the majority and minority charge carriers. The dopants are also called donors. On the contrary, boron has three electrons and accepts electrons coming from the valence band. An additional energy level called acceptor level forms a few meV above the valence band. The majority charge carriers, i.e. holes, dominate the conductivity and it is called p-type.

The energy band diagrams change substantially by varying the concentration or type of the majority charge carriers. The Fermi level exists at the midpoint of the band gap in the case of intrinsic semiconductors. The Fermi level moves downwards

closer to the valence band in the case of p-type semiconductors due to the increased hole density. On the contrary, the Fermi level moves upwards closer to the conduction band with increased electron density. Figure 2.6 shows schematically the position of the Fermi level.

Equations 2.5 and 2.6 give the position of the Fermi level for p- and n-type respectively, where n_i is the Intrinsic Charge Carrier Concentration and N_A and N_D are the Concentration of Acceptors and Donors respectively.

$$E_F = E_V + \frac{E_G}{2} - k_B T \cdot \ln\left(\frac{n_i}{N_A}\right) \quad (2.5)$$

$$E_F = E_C - \frac{E_G}{2} + k_B T \cdot \ln\left(\frac{n_i}{N_D}\right) \quad (2.6)$$

Photogenerated carriers¹ are characterized by their Lifetime τ , which represents the average time that the carriers walk randomly prior to recombination. The average length that a charge carrier roams, also called Diffusion Length L , is proportional to the Diffusion Constant D and τ according to Equation 2.7.

$$L = \sqrt{D \cdot \tau} \quad (2.7)$$

2.2 General aspects of semiconductor electrochemistry

2.2.1 Semiconductor-metal interface

When two dissimilar metals are brought together and an electrical contact forms, current flows across the contact. The driving force for this process is the difference between the Fermi levels of both materials. Prior to the contact, each metal has its characteristic Fermi level. As metals are contacted, electrons flow from the metal with higher Fermi level to the other metal until both Fermi levels balance. As electrons migrate, the Fermi level diminishes due to the decrease in the electron density. Correspondingly, the Fermi level at the other metal increases and both Fermi level match. The net charge transfer across the interface is thus equal to zero.

A similar process occurs when a semiconductor and a metal are contacted. Figure 2.7 shows the formation of a p-type-metal (a,b) and n-type-metal (c,d) interfaces. In the case of a n-type semiconductor, the majority charge carriers are electrons and the Fermi level of the semiconductor is higher than that of the metal (step c). As both are brought into electrical contact, charge transfer occurs and Fermi levels balance (step

¹Only minority charge carriers produced by illumination are considered. Additional majority charge carriers produced by illumination are negligible in comparison to the large amount of majority charge carriers already present at the semiconductor.

d). At equilibrium, both Fermi levels are equal and the net charge transfer is zero. The majority charge carriers locate at the surface of the semiconductor due to the higher charge carrier concentration within the semiconductor in contrast to the two metals case. Since the Fermi level must be constant across the semiconductor, an electric field appears and the energy bands bend in order compensate the depletion of charge at the surface. The energy bands are bent towards a higher energy because there are less electrons at the surface than in the semiconductor bulk. Similarly, but in an opposite way, happens with p-type semiconductors and metals. The majority charge carriers are holes, thus accept electrons from metal. The energy bands bend towards lower energies to compensate the electric field caused by the holes located at the interface.

The region in which the energy bands are bent is called Space Charge Region *SCR* and extends into the interior of the semiconductor volume due to the low electrical conductivity of semiconductors. The thickness of the SCR is obtained by solving the one-dimensional Poisson's equation, which relates the Charge Density $\rho(x)$ to the Electrostatic Potential V . Equation 2.8 gives the SCR Thickness d_{SCR} assuming that the charge density is proportional to the amount of dopants. N_{DOP} is the Doping Concentration and $\Delta E_F/e$ is the size of band bending. The thickness of the SCR extends from a few Å up to μm depending mainly on the doping density.

$$d_{SCR} = \sqrt{\frac{2 \cdot \epsilon_0 \epsilon_S \cdot (\Delta E_F - e \cdot U_{ext})}{e^2 \cdot N_{DOP}}} \quad (2.8)$$

2.2.2 Electrolytes

Electrolyte solutions represent a more complicated system than crystalline semiconductors and the description of energy levels is therefore complex. Electrolytes are chemical compounds that dissociate into electrically charged ions when dissolved in a solvent. Electrolytes are divided in three major groups: Acids, bases, and salts. Due to their fluid nature, electrolytes composed of charged moving components, i.e. ions, that interact with each other. The transport and movement of ions within the fluid can take place simultaneously with drift, diffusion, convection, or a mixture of all of them.

Different parameters characterize an electrolyte. Specific resistivity values vary typically in the range of 1 to 10 Ωcm . Table 2.2 presents typical ion mobility and diffusion constants of electrolytes. These values and the dielectric constant depend strongly on the electrolyte concentration.

The band theory states that the charge transfer between an electrode and the electrolyte takes place from the energy levels within or from surface states of the electrolyte into the energy levels of the electrolyte, which are located in the orbitals of the ions present in the solution. The addition of solvents to the electrolytes creates a solvent shell in the surroundings of the electrolyte ions. The charge transfer occurs via two parallel reactions: The reduction reaction and the oxidation reaction. The reduction reaction implies the transfer of electrons from the electrode into an orbital of the solution ion. The flow of electrons moving in this direction is called reduction current. Oppositely, the oxidation reaction involves the transfer from electrons coming

Ion Mobility	Diffusion Constant
$\mu_{F^-} = 5.7 \cdot 10^{-3} \frac{cm^2}{Vs}$	$D_{F^-} = 1.5 \cdot 10^{-5} \frac{cm^2}{s}$
$\mu_{H^+} = 3.6 \cdot 10^{-3} \frac{cm^2}{Vs}$	$D_{H^+} = 9.3 \cdot 10^{-5} \frac{cm^2}{s}$
$\mu_{OH^-} = 2.1 \cdot 10^{-3} \frac{cm^2}{Vs}$	$D_{OH^-} = 5.4 \cdot 10^{-5} \frac{cm^2}{s}$

Table 2.2: Ion mobilities and diffusion coefficients in diluted HF-based electrolytes

from the ion orbitals into the electrode. The flow of electrons moving into the electrode is called oxidation current. A pair consisting of both species is called redox couple. Equations 2.9 and 2.10 show the reduction and oxidation reaction respectively. *Red* represents the ions that donate electrons to the electrode, also called reducing species. *Ox* represents the oxidizing species, i.e. ions located at the electrode that accept electrons.



Figure 2.8 shows the Marcus-Gehrischer model [27],[28], which is a generally accepted model that describes the energy levels within an electrolyte. The ions located in the electrolytes have discrete energy states. However, thermal fluctuations cause continuous changes in the energy levels at the solvent shell created at the surface of the ions. The energy levels are therefore not discrete and their occupation probability is given by Gaussian curves, whose peaks are denoted as E_{ox} and E_{red} . These values represent the most probable energy levels of the oxidizing and reducing species respectively. E_{redox} represents the Redox Potential of the electrolyte, which is an extension of the Fermi level concept to electrolytic solutions.

The hydrogen couple H^+/H is used in electrochemistry as potential reference and is also called standard hydrogen electrode. Under standard conditions, the concentration of reacting and oxidizing species is equal and therefore, E_{redox} is placed in the middle between E_{ox} and E_{red} . Compared to the electron energy in vacuum, which is used as reference in solid state physics, the hydrogen couple is located -4.5 eV below the vacuum level. Equation 2.11 relates the Fermi level of the electrolyte $E_{F,redox}$ to the redox potential.

$$E_{F,redox} = -4.5 \text{ eV} - E_{redox} \quad (2.11)$$

Electrochemical equilibrium occurs as the electrode is immersed into the electrolyte. An electrochemical double layer forms subsequently at the electrode-electrolyte interface as shown in Section 2.2.3. The Fermi level of the electrode equals the redox potential of the electrolyte $E_F = E_{redox}$. The Nernst equation gives the redox poten-

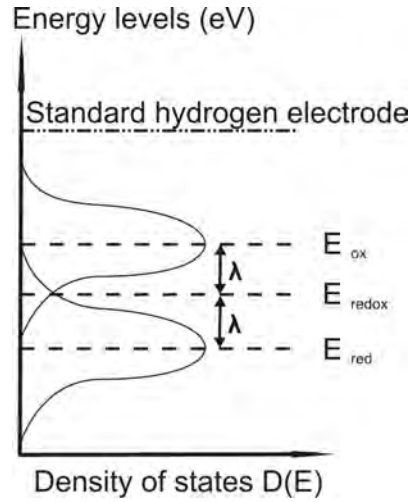


Figure 2.8: Band structure of the semiconductor-electrolyte interface. Once a semiconductor is brought in contact to an electrolyte, the Fermi level within the semiconductor equals the redox potential E_{redox} in the electrolyte. E_{ox} and E_{red} describe the oxidizing and reducing energies of the electrolyte respectively. The energy levels in the electrolyte are not discrete, and their occupation probability is represented by a Gaussian curve.

tial and is obtained as shown in 2.12, where C_{ox} and C_{red} are the Concentrations of Oxidizing and Reducing Species respectively.

$$E_{redox} = \frac{E_{ox} + E_{red}}{2} + k_B T \cdot \ln \left(\frac{C_{ox}}{C_{red}} \right) \quad (2.12)$$

2.2.3 Semiconductor-electrolyte interface

There are several models that describe the semiconductor-electrolyte interface. The behavior of the semiconductor/electrolyte interface presents similarities to the semiconductor/metal interface. Whereas in metals electrons accumulate at the interface to the semiconductor, electrolyte ions accumulate at the interface and form a double layer. The Helmholtz model considers that a layer of ions is located at the surface of the electrode and compensate its charge [30]. The Gouy-Chapman model assumes that ions are mobile due to thermal fluctuations and therefore ions form a diffuse structure called Gouy layer [31],[32]. The Stern model is generally accepted and considers that the interface is a combination of both models [33].

The immersion of a semiconductor in an electrolyte containing redox couples results in a charge-transfer process between parts until electrostatic equilibrium is achieved. The Fermi levels in both semiconductor and electrolyte equalize. An electric field appears at the solid/liquid interface, causing the formation of an electrical double layer as shown in Figure 2.9: the Gouy layer and the intermediate Helmholtz layer form in the electrolyte close to the electrode and the SCR within the electrode. The Helmholtz layer is composed of two layers, the Inner Helmholtz Plane (IHP) and the

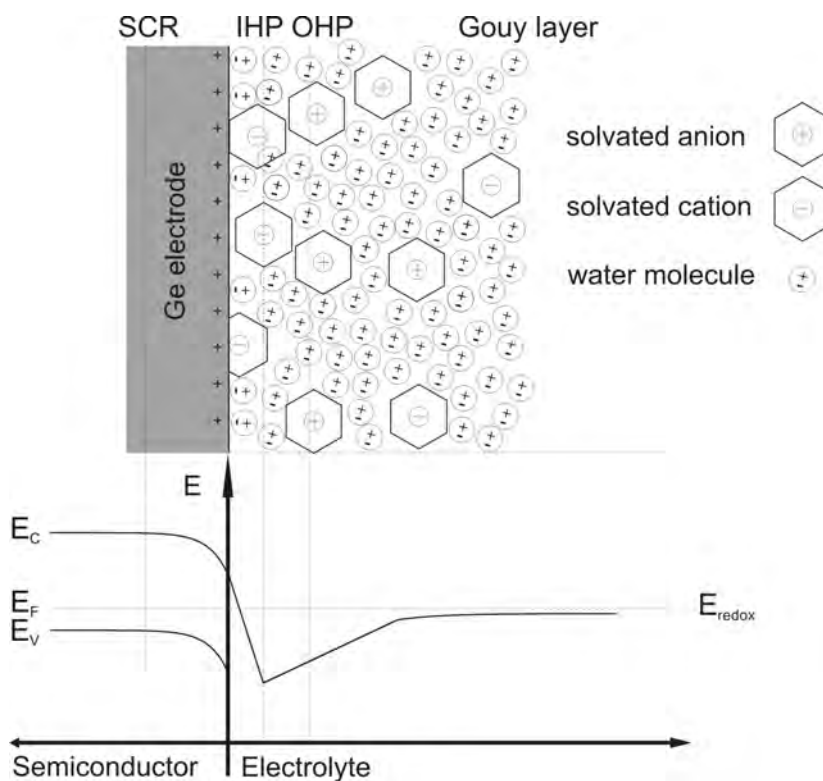


Figure 2.9: Structure of the electrical double layer at the semiconductor-electrolyte interface and the corresponding energy distribution. Note that the drastic change in the energy distribution at the IHP is only possible if the relative positions of E_F and E_{redox} permit the formation of a depletion region within the semiconductor.

Outer Helmholtz Plane (OHP). The ions present at the electrolyte can approach the interface to the distance of the OHP and the solvent dipoles surround the ions forming a solvating shell. The IHP represents the average distance from the electrode at which the polarized solvents and the adsorbed and non-solvated ions are located. The size of both Helmholtz layers together extends up to a maximum of 0.5 nm and is equal to the diameter of a solvated ion. If the charge derived from the ions within the Helmholtz layer is not large enough to influence the charge at the surface's electrode, an additional layer called Gouy layer forms with additional charged ions. The Gouy layer extends out from the electrode about 10 nm, although it depends on the electrolyte concentration. It becomes negligible for highly concentrated electrolytes.

A potential difference Φ_H , also called Helmholtz potential, appears between the outer Helmholtz layer and the semiconductor's surface due to the differences in the charge. The distance between charges corresponds to the ionic radius, including the solvating shell, which acts as a capacitor. Equation 2.13 shows that the overall potential difference, also called galvanic potential Φ_{Gal} , equals the sum of the potential difference at the Helmholtz layer and the additional potential differences at the SCR Φ_{SCR} and Gouy layer Φ_{Gou} . The term Φ_{Gou} is negligible for highly concentrated electrolytes. In the case of lowly doped semiconductors, the potential drops mainly at the SCR and the galvanic potential equals the potential drop across the SCR. For the experiments carried out in this work, highly doped Ge substrates are used and the system complicates.

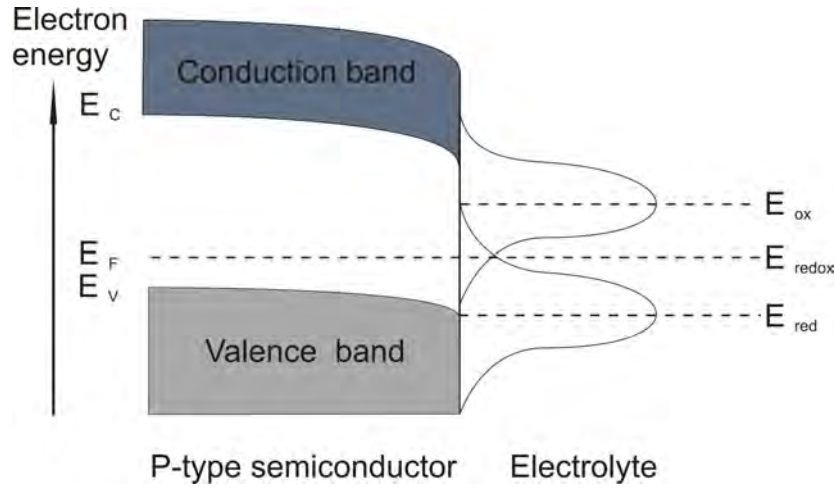


Figure 2.10: Band structure of a Ge p-type semiconductor/electrolyte interface. The Fermi level within the semiconductor equals the redox potential E_{redox} in the electrolyte. E_{ox} and E_{red} describe the oxidizing and reducing energies of the electrolyte respectively. The energy levels in the electrolyte are not discrete and their occupation probability is represented by a Gaussian curve.

Furthermore, there are certainly lots of defects, e.g. dangling bonds, that cause the formation of surface states with energetic states within the band gap, acting as an electron sink.

$$\Phi_{Gal} = \Phi_H + \Phi_{SCR} + \Phi_{Gou} \quad (2.13)$$

Similarly to the semiconductor-metal interface, band bending occurs when semiconductors contact an electrolyte solution. The Fermi levels of the semiconductor and electrolyte are dissimilar. The Fermi level E_F is higher than $E_{F,redox}$ in n-type semiconductors. Band bending hence occurs as a result of depletion of electrons at the semiconductor surface until both values balance. The p-type case shows similar behaviour but opposite. Band bending is equal to $q \cdot \Phi_{SCR}$, where the potential at the SCR is equal to the potential difference at the bulk and at the surface, $\Phi_{SCR} = \Phi_{Bulk} - \Phi_{Surf}$. Equation 2.14 gives the width of the SCR, where N_i is the Doping Concentration, i.e. N_A or N_D for p- and n-type respectively.

$$d = \sqrt{\frac{2\epsilon\epsilon_0\Phi_{SCR}}{q \cdot N_i}} \quad (2.14)$$

The Fermi level is generally lower than the redox potential. Electrons must transfer from the solution to the electrode in order to attain equilibrium. This generates a negative charge in the space charge region, which causes a downward bending in the band edges. Since the majority charge carriers have been removed from this region,

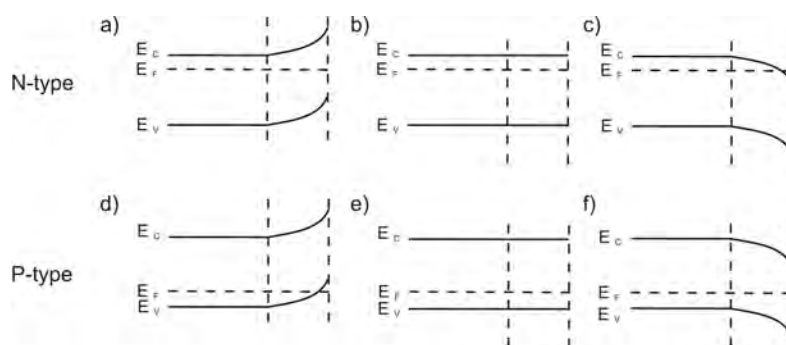


Figure 2.11: Variation of the band edges with applied potential.

it is referred to as depletion layer. Figure 2.10 shows the band structure of a p-type doped Ge semiconductor/electrolyte interface.

The I-V characteristics of a semiconductor/metal and a semiconductor/electrolyte interfaces are similar to those of a diode. Similarly to a Schottky contact, the form and bending of the bands within the SCR vary by applying a potential. Depending on the potential's magnitude and doping type, the Fermi level shifts, hence causing band bending, flattening or even accumulation. Figure 2.11 shows the effect of the applied potential on the band edges on n- and p-type semiconductors. If the Fermi energy lies at the same level as the redox potential of the electrolyte, there is neither net charge transfer nor band bending as shown in Figure 2.11.b and Figure 2.11.e. This potential is used as reference and called flat band potential. A depletion region forms as shown in Figure 2.11.a and Figure 2.11.d by applying a higher potential than the flat band potential. If a lower potential is applied, there is an excess of majority charge carriers in the SCR and it drives to an accumulation region as shown in Figure 2.11.c and Figure 2.11.f.

2.3 Summary and conclusions to Chapter 2

This chapter presented the basics of semiconductor physics and electrochemistry. Solid materials classify according to their conductivity as isolators, semiconductors, and metals. Semiconductors are of interest because the conductivity is tunable by adding dopants. It has been shown that the semiconductor-metal interface has similarities to the semiconductor-electrolyte interface. Energy band bending occurs by bringing into contact a semiconductor and an electrolyte. The Fermi level of the electrolyte and the redox potential at the electrolyte equalize. A multi-layer structure forms at the surface of the electrode. The magnitude of band bending varies with the applied etching current density, electrolyte concentration, and doping type and density. These parameters are hence important since they determine pore formation at the semiconductor.

Chapter 3

Basics on porous Si

This chapter focuses on the application of porous Si for layer-transfer processes after reorganization during high temperature annealing in hydrogen atmosphere. The chapter introduces porous Si and the Porous Silicon Process (PSI Process) to the reader and presents the fundamentals of anodic dissolution and porous silicon formation mechanisms. The reaction mechanisms for electrochemical anodic dissolution at the silicon/electrolyte interface and their current-voltage characteristics are discussed. Finally, sintering and reorganization mechanisms of porous layers in hydrogen atmosphere are explained.

3.1 Porous silicon

Since its discovery by Uhlir in 1956, porous Si has gained importance due to its interesting properties and wide range of applications [34]. It was first in the 1990's when Canham discovered an efficient luminescence emission of porous silicon in the visible region [35],[36]. As a consequence, porous silicon was object of intensive research for its potential applications in many different fields. Further investigations demonstrated its applications for layer transfer processes [3],[37].

Porous Si is generally produced by electrochemical anodization of Si in concentrated hydrofluoric (HF) electrolytes. Due to the electrochemical etching and the redox reactions, atoms coming from the Si substrate move into the solution. However, in contrast to electropolishing, Si atoms are not uniformly removed from the substrate, but in separated pores that grow into the depth leaving a porous structure which is crystalline.

Depending on the specific resistivity of the substrate and the electrolyte composition and concentration, the morphology, the porosity and the size of the pores varies. The International Union of Pure and Applied Chemistry (IUPAC) classifies porous materials in micro-, meso- and macroporous according to the pore's Diameter d [38]. The term microporous refers to pores with a diameter smaller than 2 nm. Mesoporous refers to pores with a diameter between 2 and 50 nm and finally, macroporous refers to pores with diameter larger than 50 nm.

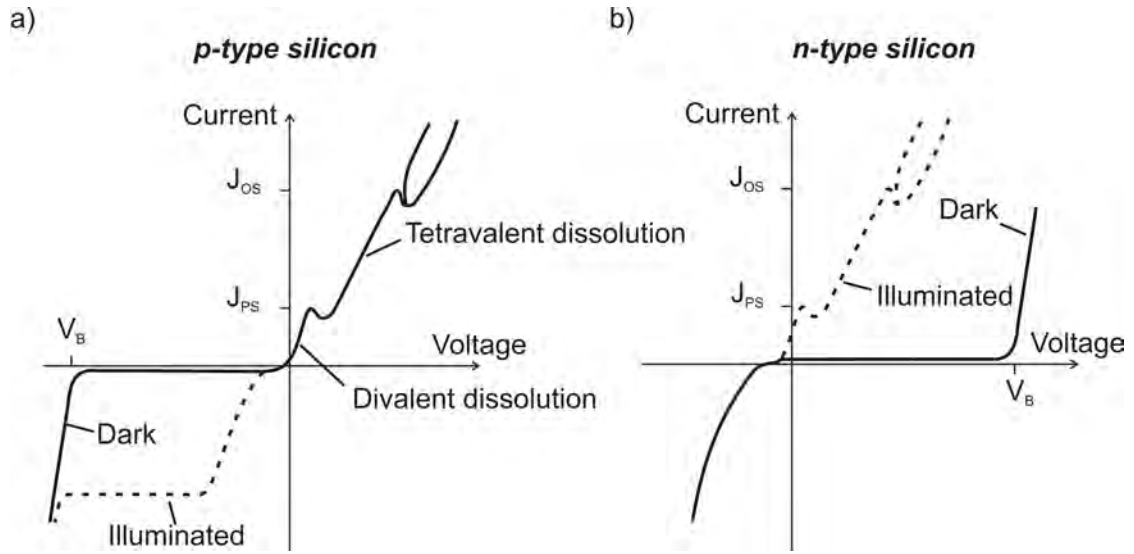


Figure 3.1: Typical I-V curves of Si in HF solutions. Curve a) refers to p-type Si and curve b) refers to n-type Si. Three regions appear under forward bias in curve a): divalent, tetravalent, and current oscillations. Figure adapted from [39].

3.1.1 Current-voltage curves and electrochemical reactions

There are several models that describe the anodization and formation of mesoporous Si. Lehmann proposed a mechanism for anodic dissolution in HF electrolytes which is generally accepted [40],[41]. Figure 3.1 shows schematically the characteristic current-voltage curves of p- and n-doped silicon in HF-based electrolytes according to the studies presented by Föll [42]. Concrete values and the shape of the curve depend on substrate's doping, electrolyte, and illumination of the sample during etching. The Si electrode limits the charge transfer and therefore, the semiconductor/electrolyte junction behaves similarly to a Schottky diode. For example, under dark and reverse bias conditions, i.e. negative bias for p-type Si and positive bias for n-type Si, a tiny leakage current is available and breakdown occurs at a certain voltage denoted as V_b .

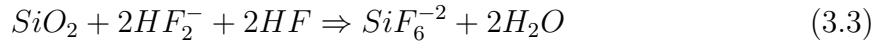
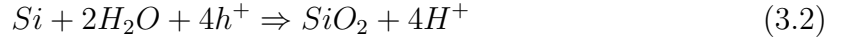
Lehmann's model distinguishes three regions under forward bias conditions in the I-V curves of Si substrates in acidic HF-based electrolytes: Below J_{PS} , between J_{PS} and J_{OSC} , and above J_{OSC} . Lehmann's model states that Si atoms will be removed mainly through the divalent dissolution mechanism for etching processes with etching current density values under the critical current density J_{PS} . Therefore, only two charges are necessary to remove a Si atom from the substrate. Mesopore formation occurs under such conditions. The overall equation for this process is:



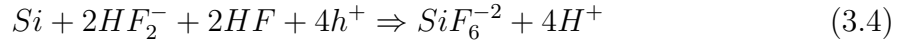
The divalent dissolution mechanism and pore formation is divided in six steps. The dissolution process starts with a hydrogen-terminated surface, which is obtained by introducing the Si electrode into the electrolyte. Hydrogen atoms passivate the surface and cover each Si surface atom with two hydrogen atoms. In step 1, a hole

coming from the Si bulk arrives at the surface, where HF_2^- ions are present and allows the nucleophilic substitution of a hydrogen atom by a fluorine atom. This step limits the etching rate of the reaction mechanism and is proportional to the applied etching current density. Step 2 and 3 comprise the substitution of the second hydrogen atom under injection of an electron. Simultaneously, a volatile H_2 molecule forms and evolves from the electrode. In steps 4 and 5, the Si-F bonds polarise the two Si-Si back bonds which are attacked by HF_2^- ions. Step 6 comprises the formation of a SiF_4 molecule that reacts with two further F^- atoms to form SiF_6^{2-} . Simultaneously, the Si surface is passivated with hydrogen atoms.

Tetravalent dissolution, i.e. four charge carriers needed for single atom dissolution, occurs for etching current density values between J_{PS} and J_{OSC} . In this case, the Si dissolution reaction has two steps and dissolution occurs via an intermediate anodic oxide; first Si atoms react with water to form SiO_2 , which is water insoluble and can only be removed with HF. In the second step, the SiO_2 is removed with HF. Simultaneously, the substrate gets electropolished, resulting in a thinner substrate.



The overall tetravalent dissolution reaction equation is as follows:



Two consecutive current maximum and minimum, marked as J_{PS} and J_{OSC} , appear in the p-type curve under forward bias conditions. The local minimum observed at the critical current density value J_{PS} comes out as a consequence of the change in the dissolution valence from two to four. For etching current densities close to J_{PS} , very strong hydrogen evolution takes place, having thus a stirring effect on the surface. As the critical etching current density is reached, hydrogen evolution virtually stops, thus cancelling the stirring effect and decreasing the rate of mass transfer from the electrolyte into the substrate. The etching current density reduces because the rate of mass transfer diminishes due to the resistance of the oxide formed at the substrate boundary for tetravalent dissolution.

Current oscillations appear for etching current densities exceeding J_{OSC} . A passivation oxide layer forms at the surface of the semiconductor if the anodic potential is sufficient. HF electrolyte etches away the silicon oxide and oxide forms again, causing thus the oscillations. The "Current-Burst" model introduced by Carstensen *et al.* relates the oscillations to the growth and subsequently etch of silicon oxide under such etching conditions [43],[44].

3.1.2 Pore wall passivation mechanisms

The formation of a porous structure requires a mechanism that stops the dissolution of pore walls while etching at the pore tips. Pore wall passivation allows the conservation of the porous structure while the porous etching front etches deeper into the substrate. The mechanism of surface passivation is not fully understood. There are several mechanisms proposed as passivation causing, namely quantum confinement and SCR formation.

Charge's carriers energy increases if they are confined into a small volume. As a consequence, the band gap widens because the energy of electrons and holes increases. Large band gaps prevent the access of charge carriers, i.e. holes, into the porous structure and hence avoids porous dissolution. Pore formation continues at the pore tips, where holes are still available. This effect is observable for structures of a few nm and suggested mechanism for pore wall passivation of microporous Si [45].

The presence of a SCR was suggested as cause for the stop of the dissolution reaction at the pore walls [41],[46],[47]. Several experiments demonstrated the presence of a carrier-depleted layer and that the doping of the substrate, i.e. width of the substrate, correlate with the thickness of the pore walls [41] and with the pore-to-pore distance in the macroporous Si case [47].

The SCR covers the entire surface, including pore tips, where etching continues. There are therefore several mechanisms suggested for the formation of pores including SCR formation. Thermoionic emission is responsible of mesoporous Si formation in p-type and n-type substrates with specific resistivities below 10^{18} cm^{-3} [40] as well as responsible of macropore formation on p-type silicon with doping densities below 10^{16} cm^{-3} [47]. Avalanche breakdown causes etch pits in moderately doped n-type Si [41] and the formation of macropores caused by illumination or injection of charges coming from p-type regions in n-type substrates [48],[49]. Charge carrier tunneling through the SCR causes mesoporous Si formation on n-type and p-type substrates with doping densities exceeding 10^{18} cm^{-3} [41],[50].

3.1.3 Effect of the etching conditions

The electrochemical etching conditions determine pore formation. There are many parameters that affect pore formation: Substrate orientation, electrolyte temperature, sample illumination, substrate roughness, surface passivation, etc ... However, porosity, pore morphology, and etching rate strongly correlate to three main parameters: Etching current density, specific resistivity of the substrate, and electrolyte concentration.

Porosity and etching rate both increase while increasing the applied etching current density. Additional charge carriers present at the semiconductor/electrolyte interface allow higher atom dissolution and porosity. High doping levels, i.e. low substrate resistivities, show high porosities and low etching rates. The SCR width reduces due to the high doping level, allowing thinner pore walls. This effect causes the porosity to increase and the etching rate to diminish. An increase in the porosity requires the removal of more bulk material, what causes a reduction in the etching rate.

An increase in the electrolyte concentration causes a higher etching rate and a reduced porosity. Si atom dissolution, i.e. the etching rate, enhances while increasing

the electrolyte concentration as the amount of HF_2^- ions present at the semiconductor/electrolyte interface increases. The porosity reduces while increasing the electrolyte concentration because a faster Si atom dissolution creates a local current density that decreases the porosity. These effects and their physical interpretation are discussed in depth in Reference [40].

3.1.4 Porous layer annealing and reorganization

Annealing of porous materials at temperatures below the melting point is interesting for layer transfer processes. The porous structure reorganizes by introducing it in a reducing atmosphere at temperatures exceeding 350 °C [51], although temperatures of about 1100 °C serve for a complete reorganization. Depending on the porosity, two different effects take place: a compacted and reinforced structure forms for porosities below 40 % and a collapsed layer with large voids forms for porosities exceeding 40 %.

Thermal activation allows silicon atoms to migrate and rearrange. The crystal structure remains unaffected during reorganization and atoms exchange their position within the crystal lattice. The internal surface diminishes and large voids form caused by the reduction of the surface energy, which is related to the internal surface area. The thermal activation permits Si atoms to move into more energetically advantageous positions, hence reducing the surface-volume ratio. There are three basic diffusion mechanisms in the literature that describe rearrangement of Si atoms during annealing [52]:

- Gas phase diffusion: Si atoms present at pores evaporate from the pore walls, diffuse into another position within the pore matrix, and finally precipitate in another position.
- Volume diffusion: Si atoms or vacancies diffuse throughout the volume and consolidate in another position.
- Surface diffusion: Si atoms move along pore walls within the pore matrix and change their position. This mechanism is the most important diffusion mechanism as shown by Müller *et al.* [53],[54].

3.2 The Porous Silicon Process

The fabrication of thin monocrystalline Si layers was studied by Yonehara *et al.* by applying an epitaxial growth on a porous substrate and subsequently a layer transfer to an insulator by means of wafer bonding [55]. However, Brendel was the first to introduce a porous-based layer transfer process to the photovoltaic community [3]. The PSI process is a layer transfer technique based on the epitaxial growth of monocrystalline thin-film Si layers on top of a mesoporous double layer [3],[56]-[60]. It permits the fabrication of very thin Si devices and is applicable to the production of very thin monocrystalline Si solar cells. Figure 3.1 shows schematically the PSI process. A monocrystalline p-type doped Si wafer with (100) orientation and specific resistivity in the 8-12 mΩcm range serves as starting substrate. In the first step, a mesoporous

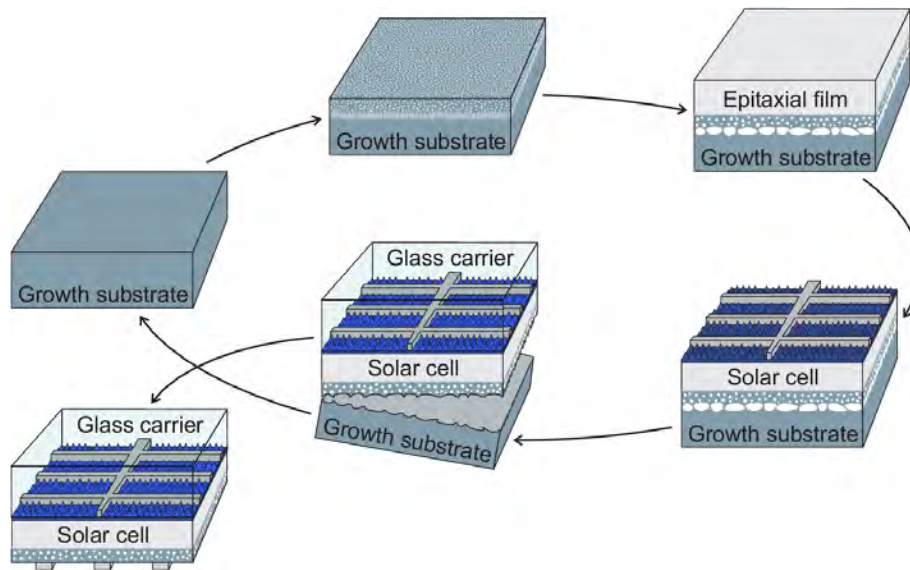


Figure 3.2: Schema of the PSI process. The cycle starts with a porous double layer formation followed by annealing and subsequent epitaxial growth of the Si device. The solar cell is processed and encapsulated for lift-off, transferred to the glass carrier and the back side of the cell can be further processed. Finally, the substrate is cleaned for further re-use. Figure from [39].

double layer is produced on top of the substrate by means of electrochemical etching. The electrolyte is HF (50 wt. %) : ethanol = 2:1 (vol.). An etching current density of 5 mA/cm^2 is applied for 1 min for the upper porous layer, also called starting layer, yielding a porous layer with a porosity in the 20-30 % range. The bottom layer, also called separation layer, is obtained by applying an etching current density in a range of 150 to 250 mA/cm^2 during 100 sec, yielding a layer of about $1 \text{ }\mu\text{m}$ and with a porosity exceeding 40 %. The starting layer is used as a seed layer for the Si epitaxy, while the separation layer is used as a pre-determined breaking-point.

The substrate is annealed in the second step in hydrogen atmosphere at $1100 \text{ }^\circ\text{C}$ for 1 hour, causing thus the reorganization of the porous double layer. Hydrogen atmosphere is compulsory in order to remove oxide rests that might hinder porous reorganization. The starting layer rearranges and the surface becomes nearly closed, allowing thus a subsequent epitaxy. The silicon device is epitaxially deposited onto the porous layer, for instance by means of Chemical Vapour Deposition (CVD). The Si thin-film preserves the crystal orientation of the starting substrate and grows monocrystalline. The separation layer weakens mechanically due to reorganization, allowing thus a later controlled lift-off of the epitaxial film.

In the next step, the front side of the solar cell is processed. The PSI process permits the application of technologies applied in the photovoltaic industry for the fabrication of solar cells, such as wet chemical surface and texturing processes, diffusion for emitter formation, and the deposition of metal contacts. Once front side cell processing is finished, the cell is adhered to a low-cost substrate in the next step, typically a glass carrier, and becomes encapsulated. By applying a mechanical force, the solar cell is removed from the substrate throughout the reorganized separation layer. The rear

side of the solar cell is processed. Finally, the rests of the porous layer present at the substrate are removed and the surface is conditioned for further use and a new PSI cycle. A 10 times re-use of a single substrate coupled to solar cell fabrication was successfully demonstrated [59].

3.3 Summary and conclusions to Chapter 3

This chapter serves as reference for successive studies regarding mesoporous Ge formation. The chapter has shown that porous Si forms by electrochemical etching in HF-based electrolytes. In comparison to Ge, the formation of mesoporous Si has been extensively studied and the dissolution mechanisms are well understood. I-V curves in Si have three different regions: Below J_{PS} , between J_{PS} and J_{OSC} , and above J_{OSC} . Si pore formation occurs for etching current densities below J_{PS} , i.e. divalent dissolution. Tetravalent dissolution occurs for etching current densities between J_{PS} and J_{OSC} and current-voltage oscillations occur for etching current density values exceeding J_{OSC} . An efficient pore wall passivation mechanism is compulsory in order to avoid dissolution of already-formed porous Si.

Porous Si annealing is necessary for porous reorganization. Thermal activation allows Si atoms to rearrange and reorganize in an energetic favourable position. The internal surface diminishes and the morphology depends on the porosity of the layer prior to annealing. The PSI process serves for reproducible layer transfer of thin-film high-efficiency monocrystalline solar cells. The process uses a mesoporous double layer with different porosities that reorganize differently during annealing depending on the porosity. The starting layer with low porosity compacts and its surface gets closed, allowing high quality epitaxial growth, whereas the separation layer with high porosity weakens mechanically allowing controlled separation of the solar cell. A 10-time re-use of the substrate has been already demonstrated.

Chapter 4

Porous Ge fabrication and characterization

This chapter deals with the design of the different etching cells available at the ISFH that allow electrochemical etching and porous formation. The experimental procedure for porous Ge layer formation is hereby discussed with emphasis on safety and sample handling. The second section presents the annealing setup used for porous layer annealing and reorganization after etching. Finally, different techniques used for porous layer characterization and analysis are briefly introduced.

4.1 Electrochemical etching setup and working procedure

An etching setup suited for porous layer formation has to meet different technical and safety requirements. The electrolyte selected and its concentration limit the construction material of the etching cell. Mesopore formation by means of electrochemical etching is commonly carried out using diluted acidic etchants with a concentration in a range of 1 to 50 wt. %. Common electrolytes are hydrofluoric acid (HF), hydrochloric acid (HCl), and sulfuric acid (H₂SO₄) diluted in water or in wetting agents like ethanol (CH₃CH₂OH) or acetic acid (CH₃COOH). The wetting agent increases the wettability of the substrate, helping thus to remove hydrogen bubbles evolving from the substrate during the dissolution process. Ethanoic solutions increase the depth uniformity of the porous layers because ethanol molecules infiltrate into the pores and homogenize porous formation. Other organic solvents like dimethylformamide (DMF, C₃H₇NO) or dimethyl sulfoxide (DMSO, C₂H₆OS) serve as well for macropore formation. Appendix C provides detailed information concerning the preparation and mixture of electrolytes with varying concentrations.

The etching cell must be fabricated in a highly acidic resistant material and is generally produced using polypropylene (PP), polytetrafluorethylene (PTFE), polyetheretherketone (PEEK), polyoxyfluoracetate (PFA), or Teflon[®]. The electrodes are immersed in the electrolyte and made of platinum in order to avoid corrosion. The rubber ring for sample sealing is fabricated in Viton or other similar resistant materials.

The use of highly concentrated acids is very dangerous and sample handling must be

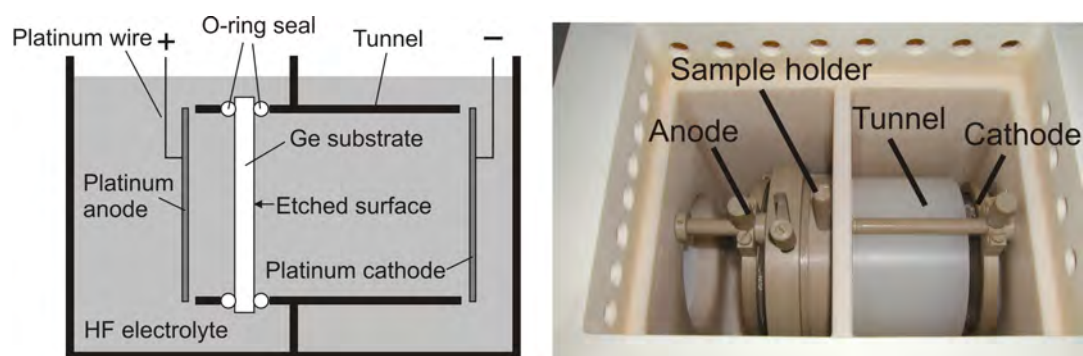


Figure 4.1: The figure on the left hand side shows a schematic cross section of the double cell reactor. The figure on the right hand side shows a photograph of the double cell reactor used for 4 inch substrate etching.

adapted. HF is toxic, corrosive and hazardous to waters, specially in the concentration regime used in this work. Exposure to skin, ingestion, or inhalation of vapors are deadly. The use of protective clothings, boots, gloves, face masks, and air inhalation filters is hence necessary. An extractor hood ensures adequate ventilation and prevents vapor inhalation. Manual handling of parts exposed to hydrofluoric acid must be avoided. Any part in contact with HF must be rinsed carefully with water before and after use. Workers must have an emergency set with calcium gluconate gel and be instructed in the event of a HF-accident.

The experiments realized in this thesis are carried out in three different etching cells. A detailed overview on different etching cell constructions is given in Reference [40].

Double cell reactor: Figure 4.1 presents the so-called double cell reactor, which consists of two chambers separated by a wall with a circular opening with a diameter of 86 mm. Wafers are mounted on a Viton-sealed sample holder and placed in the circular opening at the anodic chamber side between the anode and the cathode. A bayonet locker fixes the sample holder to the etching cell and ensures electrical isolation of both chambers. A tunnel placed between the cathode and the circular opening increases the field homogeneity through the etching cell, thus allowing a more homogeneous pore distribution. The electrolyte is responsible for current conduction from cathode to anode. The electrolyte is at room temperature and covers the entire substrate. Approximately 3.5 litres of electrolyte are necessary to complete coverage of the substrate and electrodes. The sample holder, electrode holder, tunnel, and bayonet locker are fabricated in PEEK and the cell chambers in PP. The chambers are cuboidally-shaped and their size is 9 x 16 x 15 cm (width x height x depth).

The etching procedure starts with substrate mounting and fastening to the sample holder. The sample is thus rinsed using deionized water and introduced into the etching cell, which was previously filled in with the electrolyte. The electrolyte rapidly dissolves water soluble native oxides formed at the substrate. An etching current density - time profile etches the sample. A computer controlled 8872-130 (Toellner) power supply with a maximum of 130 V and 25 A serves as a potentiostat. The etching duration varies in a range from a few seconds up to 12 hours. Once etching is finished, the

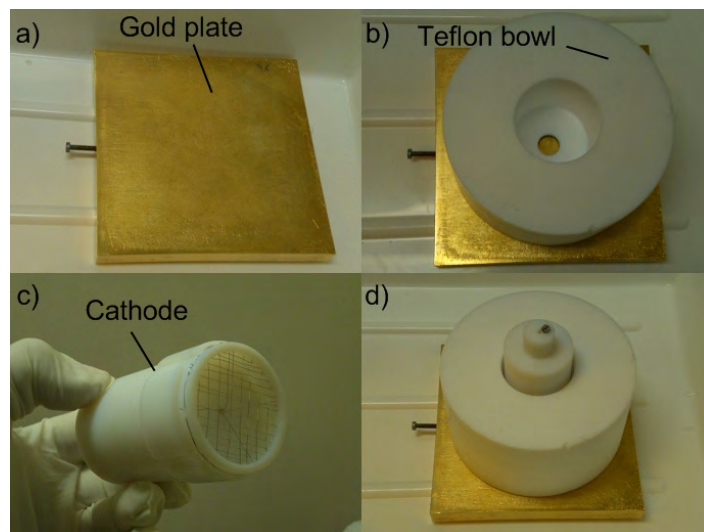


Figure 4.2: Single parts of the back contacted cell. Figure a) shows the gold coated plate which serves as anode. Figure b) shows the Teflon[®] bowl and the aperture with rubber ring where the sample is placed. Figure c) shows the cathode with the platinum dragnet. Finally Figure d) shows the mounted back contact etching cell.

sample is dismounted, rinsed, and dried in nitrogen flow. Samples are preserved in nitrogen atmosphere in order to avoid oxidation.

An increased concentration of HF at the bottom of the etching cell is observable for long anodization experiments, due to higher density of HF compared to that of water. The etching process in Ge is very sensitive to the electrolyte concentration. The etching cell does not have a pumping system to mix the electrolyte. The electrolyte must be poured out after each experiment in order to obtain a better distribution of the HF concentration in the electrolyte. The HF concentration is uniform when the etching cell is filled again with the same electrolyte.

Back contacted cell: This home-made electrochemical cell etches small samples of 1.77 cm^2 . It consists of three parts: A gold coated plate which acts as anode, a cathode mounted on a Teflon[®] structure, and finally a Teflon[®] bowl with a hole to insert the sample as shown in Figure 4.2. A rubber ring seals the sample and avoids the electrolyte to flow away. The electrolyte is at room temperature.

The procedure starts by placing the sample between the gold coated plate and the Teflon[®] bowl. Good ohmic contact is easily obtained due to the sample's high doping concentration. Aluminum foils underneath the sample ensure an improved contact and avoid gold contamination for further processes. Lowly doped samples are contacted using eutectic GaIn. The electrolyte is poured into the Teflon[®] bowl and the cathode is subsequently deposited on top of it. The computer controlled 8872-130 (Toellner) power supply provides the etching profile. Alternatively, the potentiostat Elypor 3 (ET&TE Etch & Technology GmbH) allows various etching profiles, i.e. current or voltage vs. time profiles, to be programmed. The etching current density is set to a fixed value and the etching potential is automatically adjusted to obtain the desired etching current density. After the etching process, the sample is dismounted, rinsed,

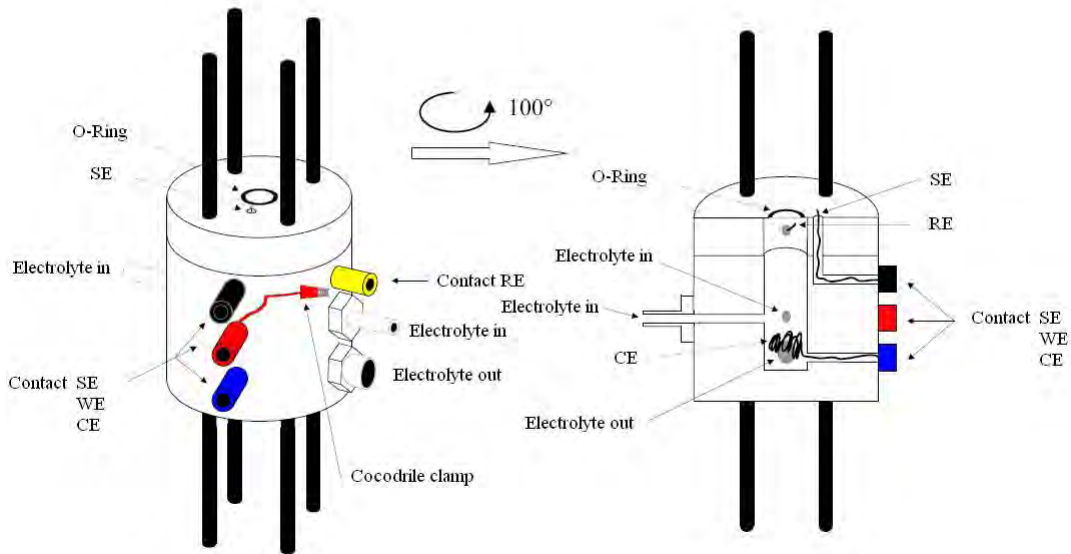


Figure 4.3: Schematic view of the laboratory etching cell. Figure from ET&TE Etch & Technology GmbH.

and dried in nitrogen flow. Samples are preserved in nitrogen atmosphere in order to avoid oxidation.

Laboratory etching cell: This etching cell has an area of 1 cm^2 . The cell uses four platinum wire electrodes, two for applying the desired etching current density, and two for measuring the potential drop within the sample. The so-called Reference Electrode (RE) and Counter Electrode (CE) are located within the etching cell and in contact with the electrolyte. Both electrodes are separated from the sample 4 and 12 mm respectively. The Working Electrode (WE) and Sense Electrode (SE) are connected to the sample but are not short circuited. The WE is connected to the sample by using a back contacted plate. The potentiostat Elypor 3 (ET&TE Etch & Technology GmbH) with SiPor software provides the power supply. A manually controlled peristaltic pump introduces the electrolyte into the etching cell from a reservoir. A computer controlled water circulator controls the temperature of the electrolyte. The etching cell is manufactured in solid PTFE and has a working temperature range of $-5 \text{ }^\circ\text{C}$ to $+65 \text{ }^\circ\text{C}$. The cell includes a LED-array for back side illumination in case of etching n-type substrates. The software allows additionally impedance spectroscopy measurements.

The etching procedure starts as the sample is placed at the aperture and fixed using the back-contact plate. In order to ensure a good and continuous contact to the electrolyte, the etching cell is turned 180° and the sample is located at the lowest part of the etching cell. The peristaltic pump removes the electrolyte once the experiment is finished. The etching cell is turned back to its stationary position, and the sample is now dismantled. Afterwards it is rinsed and dried in nitrogen flow. Samples are preserved in nitrogen atmosphere in order to avoid oxidation.

4.2 Annealing setup

The reorganization of porous Ge layers is investigated by applying a subsequent high temperature process. Two different annealing furnaces serve for annealing: an Annealing Furnace (Thermco) and Serie Sirius Lab 1000 (LPT).

Thermco Annealing Furnace: This annealing furnace is suitable for annealing in nitrogen, forming gas (95% N₂ + 5% H₂), and argon atmospheres. The Thermco Annealing Furnace consists of a 1.85 m large quartz tube with a diameter of 142 mm. The maximum temperature of the oven is limited to 1000 °C and has a maximum capacity of 50 wafers with a maximum size of 4 inches. Before introducing the porous samples, the process chamber is fluted during 15 min with the corresponding atmosphere in order to avoid oxygen traces. The samples are mounted on a quartz boat and introduced into the furnace; the temperature is increased up to the desired temperature. The annealing control unit increases the temperature and controls the heating rate, temperature stabilisation, and duration of the plateau. The furnace is air cooled and the process is carried out at atmospheric pressure. Gas flows are in the 1-10 L/min range and annealing temperatures in the 450-750 °C range.

LPT Serie Sirius Lab 100: This annealing furnace is suitable for sample annealing in nitrogen, argon, and hydrogen atmospheres. However, it is solely used for hydrogen annealing due to its high gas flow requirements. After electrochemical etching, samples are mounted in a quartz boat and introduced into the quartz tube. The load door is vacuum sealed due to explosion hazard. Annealing first starts as the oven tube is fluted with nitrogen atmosphere at room temperature for at least 30 min in order to avoid oxygen traces. Once the atmosphere inside the tube is oxygen-free, hydrogen atmosphere substitutes the nitrogen atmosphere. A three component flame treatment unit burns hydrogen at the gas exit. A minimum H₂ flow of 15 L/min is compulsory due to the size and design of the furnace. The maximum capacity of the furnace is 25 wafers with a maximum size of 6 inches. The heat control unit applies various time-temperature profiles with varying hydrogen gas flows. The maximum temperature of the oven is limited to 1100 °C and the maximum heating rate is 18 °C/min. The chamber is evacuated once the annealing process has finished and is subsequently filled in with nitrogen. Residual hydrogen burns at the flame unit. The entire system is water cooled and the process is carried out at a pressure of a few millibars over atmospheric pressure.

4.3 Porous layer analysis and characterization

4.3.1 Microscopy analysis

Microscopy is an excellent tool for qualitative and quantitative analysis of porous materials. The Scanning Electron Microscope (SEM) S-4800 series (Hitachi) at the ISFH permits a very high magnification with a relatively low effort. The orientation, homogeneity, pore size and distribution as well as the porous layer thickness are obtained by analyzing the cross section and the top view of each sample. Energy Dispersive X-ray Spectrometry analysis (EDX) serves for composition analysis of the porous layers.

A SEM/FIB Dual Beam Strata DB235 with DigiView 1612 CCD Camera (TSL Company) located at the Chair of Functional Materials lead by Prof. Dr. Mücklich at the Universität des Saarlandes serves for Electron Back Scatter Diffraction (EBSD) analysis. EBSD measurements are useful for determining whether the substrate orientation varies after electrochemical etching and likewise after porous layer reorganization.

Surface roughness is investigated using a Digital Instruments MultiMode Atomic Force Microscope (AFM) with a Nanoscope III controller located in the Chair of Nanostructures lead by Prof. Dr. Haug at the Leibniz Universität Hannover. Further information regarding the working principle of these and other microscopy techniques can be found in standard books of electron microscopy [61] - [63].

4.3.2 Porosity calculation

The Porosity P is defined as the ratio of the volume of all the pores in a layer to the volume of the layer. This is an important parameter for the characterization of porous layers and process control. Porosity determines drastically the lift-off and surface closure for epitaxial growth. The gravimetric method is applied in this thesis for determining the porosity of the sample. However, porous Ge layer formation is always accompanied by substrate thinning as will be shown in section 5.2.1. The gravimetric method must be therefore adapted. Otherwise, the weighing of the sample would account for the amount of material that gets dissolved into the electrolyte.

The procedure starts with an electrochemically etched porous Ge wafer. A Coherent Laser (AviaX) with a power of 10 W and a wavelength of 355 nm serves for substrate cutting. From a 4 inch wafer, a sample of an Area (A) of 6×6 cm² is cut off. Figure 4.4 shows an electrochemically etched 4 inch Ge wafer with a dashed line representing the laser cut. The sample has a homogeneous porous layer with a maximum thickness variation of 30 nm.

A precision balance AUW120D (Shimadzu) with wind protection weighs the sample (m_1) of 36 cm². The balance is calibrated before weighing and placed at the sample holder, waiting about 1 min until the value becomes stable. This balance has a maximum weight of 42 g and a standard deviation of $\sigma = 20$ μ g. A lowly concentrated potassium hydroxide (KOH) bath at room temperature removes selectively the porous Ge layer. The substrate remains unaffected and does not get etched. The mass of the substrate without porous layer is determined by weighing the substrate after the KOH bath (m_2).

The thickness of the electrochemically etched porous layer (Z) is determined by inspecting with a SEM the Ge rests after laser cutting or another reference sample with the same etching parameters. Equation 4.1 gives the mass of a bulk Ge layer with the same thickness than the electrochemically etched porous layer (m_{layer}), where ρ_{Ge} is the bulk density of Ge ($\rho_{Ge} = 5.323$ g/cm³).

$$m_{layer} (g) = \rho_{Ge} \left(\frac{g}{cm^3} \right) \cdot Area (cm^2) \cdot Z (cm) \quad (4.1)$$

The mass difference ($m_1 - m_2$) is the mass of the porous Ge layer that has been removed. The ratio of removed mass ($m_1 - m_2$) to m_{layer} is the fraction of material that

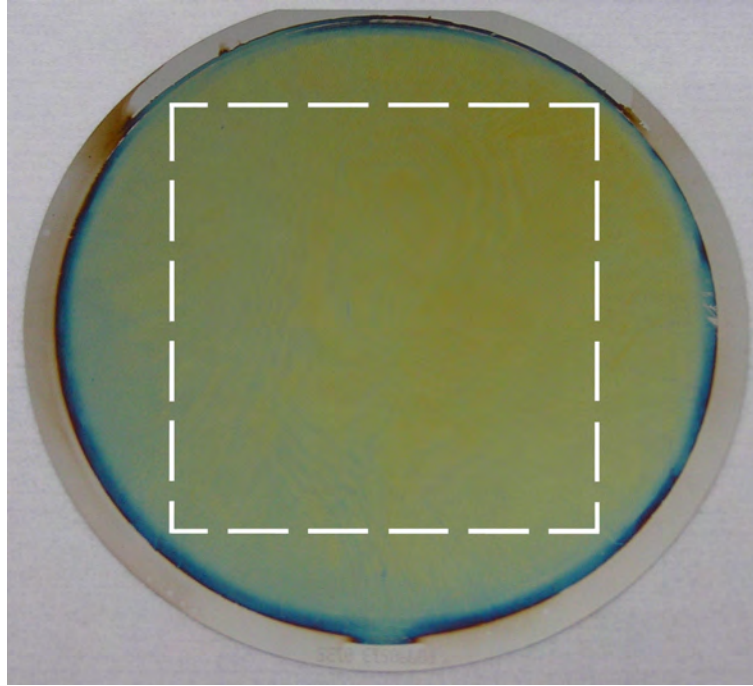


Figure 4.4: Ge wafer electrochemically etched (100) p-type Ge, HF 50 wt. %, $j = 1$ mA/cm², $t = 3$ h. Note that the dashed line represents the region which is cut out of the substrate with a laser for porosity measurements.

still remains after the electrochemical etching process. Equation 4.2 gives the porosity of the PGe layer.

$$P = \left(1 - \frac{m_1 - m_2}{m_{layer}} \right) \quad (4.2)$$

4.3.3 Etching rate calculation

Porous Ge formation is accompanied by constant dissolution of the already porosified surface [14],[21]. There are two etching fronts with different etching rates as the porous layer grows into depth. On the one hand, the etching front at the bottom of the PGe layer is responsible of its growth. The porous layer etching rate R_{etch} quantifies the velocity at which the porous layer grows into the sample. On the other hand, the already formed porous layer is continuously dissolved at its upper surface. The porous layer dissolution rate R_{diss} denotes the velocity at which the porous layer dissolves, limiting thus the growth rate of the porous layer. The difference between etching rate and dissolution rate gives the growth rate of the mesoporous layer R_{growth} .

R_{diss} is obtained by linearly fitting the remaining thickness of the substrate plus the thickness of the porous layer as a function of the etching duration. The slope of the linear fit gives the porous layer dissolution rate for each etching current density and electrolyte. The slope of a linear fit to the porous layer thicknesses measured by SEM as a function of the etching duration gives R_{growth} for both aqueous and ethanoic electrolytes, and for several current density values. The addition of both terms gives

R_{etch} . Note that R_{etch} and R_{diss} are given in $\mu\text{m}/\text{min}$ and R_{growth} is given in nm/min .

4.3.4 Valence number calculation

The valence number of the dissolution process is calculated by means of Faraday's law of electrolysis shown in Equation 4.3. This electrochemical basic relation states that the mass of a substance altered at an electrode during electrolysis is directly proportional to the quantity of electricity transferred to the electrode. Assuming that the amount of material removed from the substrate follows a unique dissolution reaction mechanism with a determined valence number, it is possible to determine the Valence Number (Z) of the process.

$$Z = \frac{Q \cdot M}{F \cdot m} \quad (4.3)$$

Porous layer growth on Ge substrates is investigated for various etching times and etching current densities in aqueous HF 40 wt. % electrolyte at room temperature. Samples are weighed before and after etching in order to estimate the amount of Ge that has been dissolved (m). Knowing the applied etching current density, the Charge (Q) is obtained by multiplying it by the etched area and etching time. The Molar Mass (M) and the Faraday's constant (F) are constants and the valence number is derived for different etching current densities.

The assumption regarding valence is not strictly correct, since there are different dissolution mechanisms competing simultaneously. It additionally computes material that is removed by means of pure chemical dissolution. As a consequence, the obtained valence numbers are shifted upwards and take higher values than predicted.

4.3.5 Micro Raman spectroscopy

The optical structure of the μ -Raman spectroscopy is based on a confocal design. A focused laser beam stimulates the sample and the confocal setup carries out signal detection for each point. It is therefore possible to obtain a local analysis imaging by rastering the sample. A pinhole located before the detector unit is decisive for the confocal setup, since it fades out the information that does not come from the focal plane. Thanks to the lateral resolution, it is possible to carry out a 3-dimensional analysis of the surface of the sample.

The setup consists of a lens with fixed focus. A 3-dimensional positioning scanner with an accuracy of 2 nm is used for sample rastering. The lateral and axial scanning ranges are 200 μm (x,y) and 20 μm (z) respectively. A diode-pumped solid state laser MSL50 (Impex) with single frequency at a wavelength of 532 nm provides sample excitation. The laser beam is focused through a Plan SL 100X OBJ (Mitutoyo) lens to a confocal plane of the sample. Raman and Rayleigh scattered light is collected by the lens, passes through the confocal pinhole, and is collected through a lens at the monochromator. The Holospec f/1.8i (KOSI) monochromator has an adapted CCD camera (Andor Newton) which provides the detection system. A notch filter is responsible of the separation of the Rayleigh scattered light and inelastic diffused light.

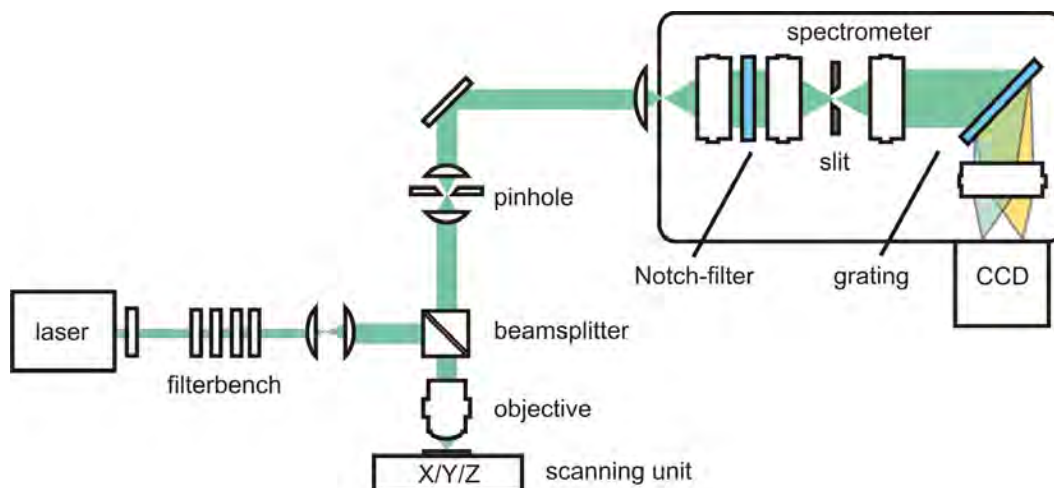


Figure 4.5: Schematic drawing of the μ -Raman setup. Figure from Dr. Gerhard Berth.

The detection signal is diffracted into two traces at the monochromator and collected at the CCD camera, which is displayed in a large wavenumber range ($0\text{--}4000\text{ cm}^{-1}$). Figure 4.1 presents the experimental setup used for μm -Raman spectroscopy analysis. This setup is located at the Centre for Optoelectronics and Photonics of the Paderborn University (Germany).

4.4 Summary and conclusions to Chapter 4

This chapter presented the experimental setup used for PGe fabrication. The experimental procedure used for the three different electrochemical cells available at the ISFH for PGe formation was shown. Mesoporous Ge layers reorganize in two different annealing furnaces available at the ISFH. The experimental procedure for porous layer reorganization in various atmospheres was presented. Finally, the measurement procedures for porosity, valence number, and etching rate calculation were described.

Chapter 5

Electrochemical etching of Ge

The following chapter presents the results of pore formation and growth on highly doped p-type Ge wafers. Electrochemical etching experiments are carried out using HCl and HF electrolytes with varying concentrations and diluted in different aqueous and organic solvents. Mesoporous single- and double layer formation are demonstrated in highly concentrated HF. The etching rates and porosities are analyzed. Macroporous Ge is obtained by using HF-based electrolytes with a concentration below 30 wt. % or in HCl in every concentration. Various etching conditions and pre-treatments for an optimized nucleation and pore growth are investigated.

5.1 Review on porous germanium

The first transistors were fabricated and tested in the early 1950's using Ge as basis material. Germanium was therefore of high interest and several investigations focused on electrochemical etching of Ge [64]-[70]. No pore formation was reported and only etch pits with varying shape were obtained. However, as the industry focused later on Si, Ge research was set aside and only a few investigations were carried out regarding PGe formation. Nevertheless, renewed interest on porous materials appeared as Canham and Lehmann discovered the luminescence of microporous Si [35],[45]. An increased interest in PGe has been observable in the past ten years and several publications appeared [4]-[24].

On the one hand, porous germanium formation was demonstrated by means of electrochemical etching. Buriak *et al.* produced porous Ge layers with thicknesses in a range of 1 μm to 15 μm by applying a cathodization process after previous anodization of the surface using highly concentrated HCl-based electrolytes diluted in ethanol [4],[5]. No structural details regarding the germanium layer were reported.

The University of Kiel has extensively studied the production of macropores and nanowires by electrochemical etching on Ge [9]-[15]. Crystallographically oriented macropores were reported using various substrate orientations, etching conditions, and electrolytes, mainly HCl, HF and H_2SO_4 . The results showed that pore formation on Ge always takes place simultaneously with electropolishing of the substrate and that nucleation is troublesome, making the PGe formation substantially more difficult in comparison to porous Si. Flamand *et al.* from IMEC in Belgium studied PGe formation using HF as electrolyte and the possibility of using it for a lift-off process [8].

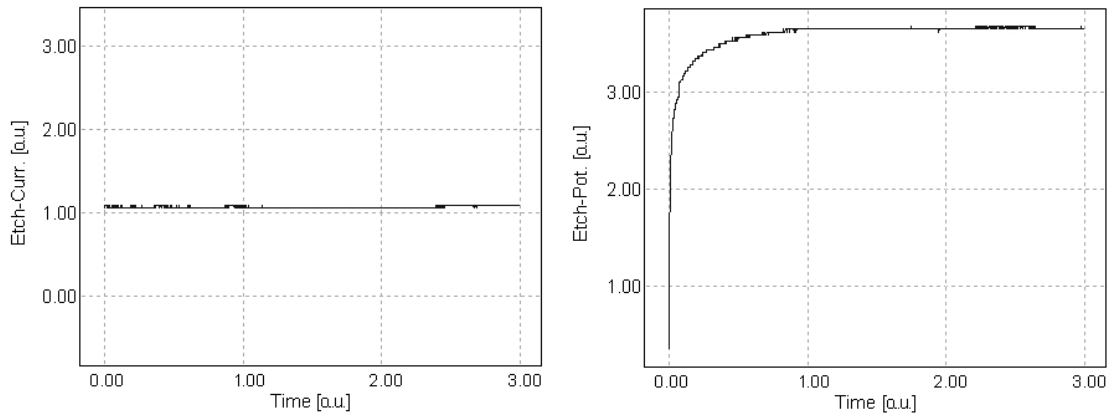


Figure 5.1: Anodic galvanostatic etching profile. The figure on the left hand side shows the etching current density, which typically takes a constant value. On the right hand side, the figure shows the corresponding potential profile, which is automatically adjusted.

However, they were not able to determine suitable conditions for lift-off and they only obtained strongly non-uniform macropores, etch pits and a porous film that could not sustain a large field intensity. They concluded that under those conditions, lift-off of PGe films was virtually impossible.

On the other hand, PGe was obtained using vapour deposition techniques. Shieh *et al.* produced PGe using a nanoparticle-assisted growth [6]. PGe films were produced by means of an Inductively Coupled Plasma Chemical Vapor Deposition (ICPCVD) on SiO₂ substrates. The process consisted on depositing gold nanoparticles on silicon dioxide. Ge vapor dissolved preferentially into gold and PGe layers formed. Van Vugt *et al.* deposited Ge electrochemically using a dried suspension of silica spheres as template [7]. The pores were filled subsequently using a plating bath, yielding a macroporous amorphous Ge layer.

A complex technique called surfactant templating was recently used for the production of mesoporous Ge. This process involves the self-assembly of inorganic compounds due to their electrostatic interactions and charge matching. An ordered PGe structure is obtained as the surfactants are removed. Sun *et al.* from the University of California and Armatas *et al.* from the Michigan State University have achieved nanoporous and mesoporous organized structures respectively by using different Ge precursors like K₂Ge₉, GeCl₄, or Mg₂Ge and their self-assembly properties [16],[17]. Mesoporous Ge shows to be an efficient hydrogen purifier, separating efficiently hydrogen from carbon dioxide or any other complex gas structures [18],[19]. It has been recently demonstrated the production of stable porous Ge films with photoluminescence emission by annealing GeO₂ films in H₂ atmosphere [20].

5.2 Mesoporous Ge layer formation

The substrates used in this investigation are epi-ready p-type Ge monocrystalline, 4 inch in diameter, and one-side polished. The thickness of the wafers is (150 ± 10) μm

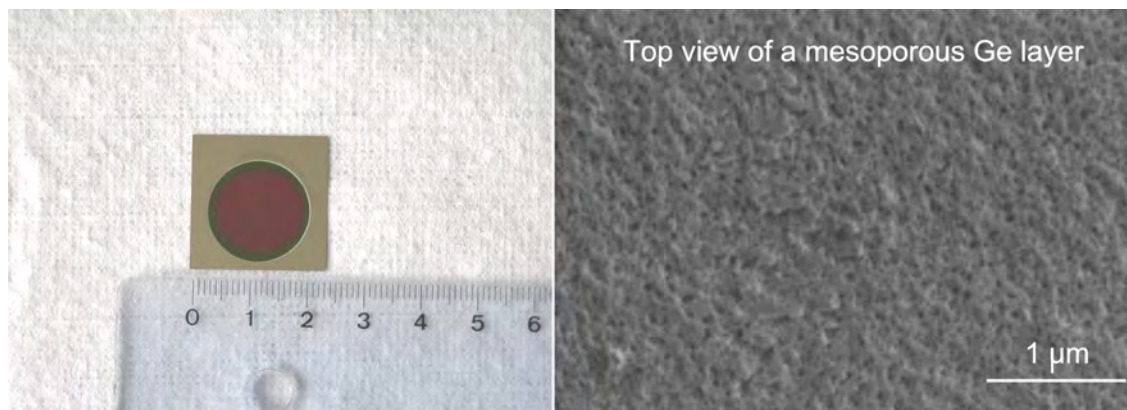


Figure 5.2: On the left hand side, a small electrochemically etched sample after porous layer formation. On the right hand side, a SEM top view of the porous layer after etching.

and the specific resistivity is $(25 \pm 15) \text{ m}\Omega\text{cm}$. The orientation of the substrates is $\{100\}$ or $\{100\}$ with a miscut of 6° off towards $\{111\}$.

Electrochemical etching experiments are carried out in galvanostatic or potentiostatic mode and in anodic or cathodic bias. Etching current densities lie typically in the $0.1\text{-}350 \text{ mA/cm}^2$ range. The corresponding voltage varies in the $0.1\text{-}25 \text{ V}$ range. The experiments are carried out without external illumination. The etching duration varies in a range of one minute to several hours. Figure 5.1 shows an anodic galvanostatic etching profile.

Uniform mesoporous Ge layers form by means of electrochemical etching using highly concentrated HF-based electrolytes in a range of 30 wt. % to 50 wt. % and etching current densities in the $0.1\text{-}100 \text{ mA/cm}^2$ range. Figure 5.2 shows on the left hand side a small sample after electrochemical etching. The porous layer presents different colors at the surface of the sample. The colored surface comes out as a consequence of the constructive and destructive Fabry-Perot interference fringes originating from reflections at the air/PGe and at the PGe/Substrate interfaces. This effect makes the porous layer seem to be colored and to present many different tonalities. The color varies depending on the thickness and porosity of the PGe layer. Very thick porous layers present characteristic grey color, typical of bulk Ge, since the reflected light coming back from the PGe/substrate interface does not reach the surface.

Figure 5.2 shows on the right hand side a SEM top view of the porous layer after etching. Randomly distributed mesopores are uniformly distributed at the surface of the sample. Fang *et al.* used various etching profiles for nucleation improvement [14]. Figure 5.3 shows two schematic profiles utilized for PGe layer formation. The figure on the left hand side shows a galvanostatic profile with a starting pulse and subsequently the etching current density is ramped up constantly. The figure on the right hand side shows a galvanostatic profile where the etching current density decreases exponentially. The results derived from these investigations did not show any improvement regarding nucleation and pore growth control. It can be stated that homogeneous nucleation and pore distribution is not troublesome for mesoporous layer growth.

The scalability of the process is proven on 4" Ge wafers which are uniformly porosi-

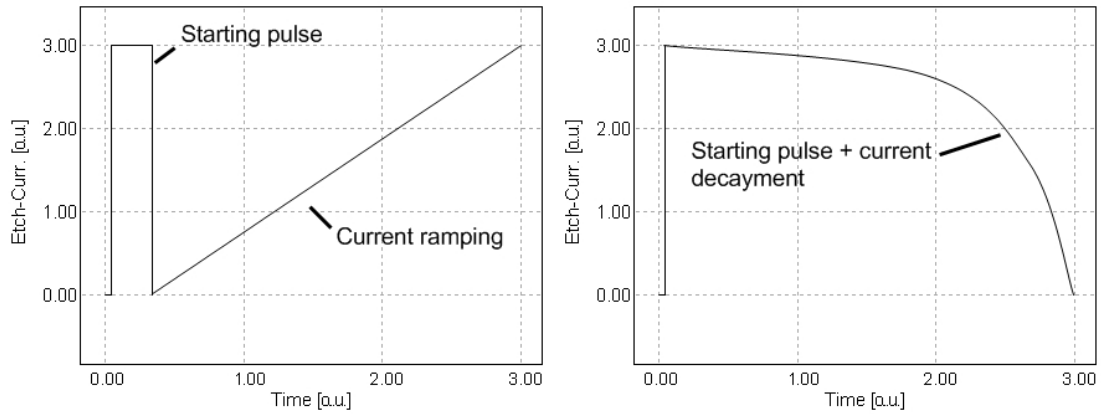


Figure 5.3: Examples of galvanostatic etching profiles for enhanced passivation. On the left hand side, the figure shows a single pulse followed by current ramping. The figure on the right hand side shows an etching profile with decreasing current density.

fied. Figure 5.4 shows the top view of a 4 inch Ge wafer after etching. The inner part of the wafer is homogeneously colored, indicating that also the porosity and thickness of the porous layer are homogeneous. SEM analysis shows indeed a mean porous layer thickness of 160 nm with a maximum variation in thickness of 30 nm within the dashed line shown in Figure 5.4. At the rim of the wafer, the sample holder causes inhomogeneous current flow and hence a stripe of different color forms.

Figure 5.5 shows the cross-sectional SEM image of a 4 inch Ge wafer. The diameter of the pores lies in a range of 1 nm to 40 nm and the mean diameter of the pores is 14.9 nm. The porous Ge layer is thus composed of mesopores. The surface roughness is less than 20 nm and the roughness at the PGe/Substrate interface is less than 20 nm.

Mesoporous layer formation in Ge is a sensitive process and many terms may affect noticeably the results obtained. The influence of the electrolyte selected and its concentration, applied potential or etching current density, etching time, and doping level of the substrate are the most important parameters that affect porous Ge layer growth.

5.2.1 Etching rates

Porous Ge formation is always accompanied by the constant dissolution of the already porosified surface. This effect has been already reported in the literature [9],[14]. Figure 5.6 introduces two etching rates, R_{etch} and R_{diss} . The porous layer etching rate R_{etch} is the velocity at which the porous layer grows into the sample. On the other hand, the already formed porous layer is continuously dissolved into the electrolyte at its upper surface. The porous layer dissolution rate R_{diss} denotes the velocity at which the porous layer dissolves, limiting thus the growth rate of the porous layer. The growth rate of the mesoporous layer $R_{growth} = R_{etch} - R_{diss}$ is the difference between etching rate and dissolution rate.

Both growth and dissolution rates are systematically studied by varying the etching time for different etching current density values in a range between 0.1 mA/cm² and



Figure 5.4: Ge wafer electrochemically etched (100) p-type Ge, HF 50% wt., $j = 1 \text{ mA/cm}^2$, $t = 3 \text{ h}$. Note that the dashed line represents the region at which the porous layer thickness has a maximum variation of 30 nm.

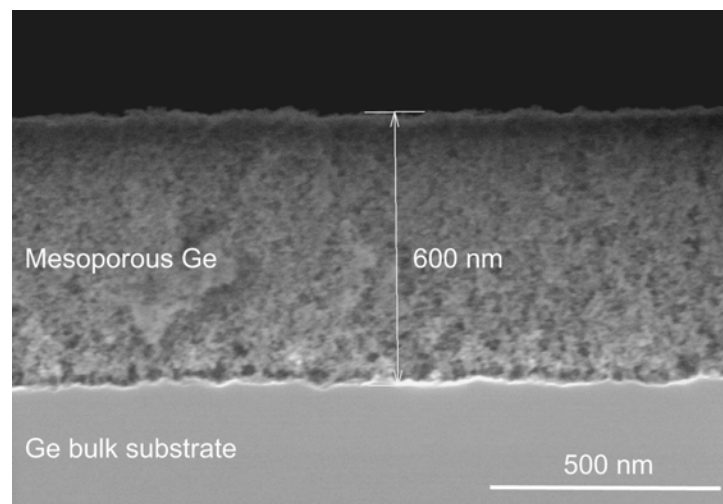


Figure 5.5: SEM image of the cross section of a PGe layer. (100) p-type Ge, HF 50 wt. %, $j = 8.85 \text{ mA/cm}^2$, $t = 75 \text{ min}$.

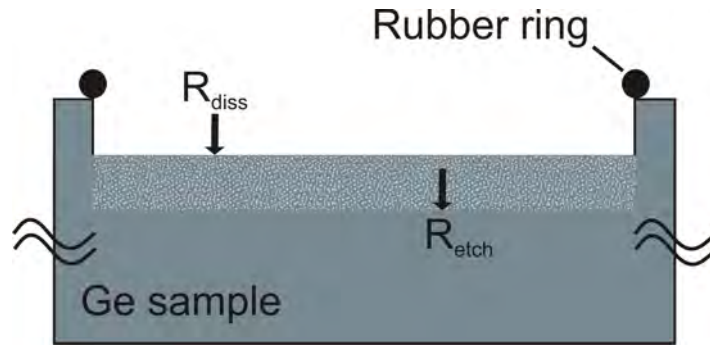


Figure 5.6: Schematic view of the cross section of a porous Ge layer and the etching rates present.

100 mA/cm² in HF-based electrolytes diluted in water or ethanol with a concentration of 40 wt. %. The thickness of the porous layer and the remaining thickness of the substrate including the porous layer are measured for each electrochemical etching experiment. The current density values are linearly fitted for ethanoic and aqueous electrolytes. The growth rate of the porous layer is thus obtained from the slope of the linear fit of the experimental data.

R_{diss} is calculated by linearly fitting the remaining thickness of the substrate plus the thickness of the porous layer as a function of the etching duration. The slope of the linear fit gives the porous layer dissolution rate. Figure 5.7 shows the porous layer dissolution rates obtained for HF 40 wt. % in water and in ethanol respectively as a function of the etching current density. Dissolution rates of 0.011 $\mu\text{m}/\text{min}$ to 1.33 $\mu\text{m}/\text{min}$ are obtained depending on the applied etching current density and the solvent used. Two linear regimes are observable in a semilogarithmic plot of the dissolution rates of the PGe layer shown in Figure 5.7: Below and above 7.5 mA/cm².

Figure 5.7 shows that ethanoic-based electrolytes dissolve more amount of substrate than aqueous electrolytes. This effect is related to the wetting properties of ethanol, as it enhances the wettability of the substrate and helps to remove hydrogen bubbles that are produced through the electrochemical etching of Ge. Since H₂ bubbles hinder PGe formation and etching, the use of ethanoic electrolytes allows a faster dissolution of the substrate into the electrolyte.

Very high etching current densities exceeding 60 mA/cm² result in a decrease in the porous layer growth rate or do not even present a mesoporous Ge layer if etching current densities exceeding 80 mA/cm² are applied. In these cases, the surface gets porosified, but the high dissolution rate avoids porous layer formation. Therefore, an increase in the dissolution rate causes a reduction of the porous layer growth. In order to reduce the dissolution of the PGe layer, very low etching current densities must be applied.

R_{growth} is obtained from the slope of a linear fit to the porous layer thicknesses measured by SEM as a function of the etching duration, for both aqueous and ethanoic electrolytes, and for several current density values. R_{growth} lies in the range between 0.071 nm/min and 2.7 nm/min for etching currents between 0.1 mA/cm² and 80 mA/cm². Figure 5.8 shows the porous layer growth rate as a function of the etching current density.

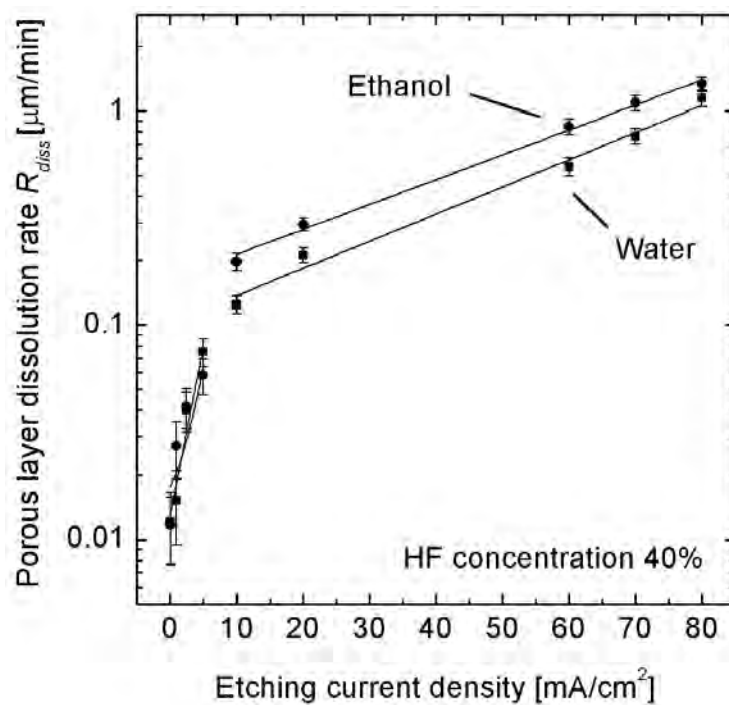


Figure 5.7: Porous layer dissolution rate vs. etching current density.

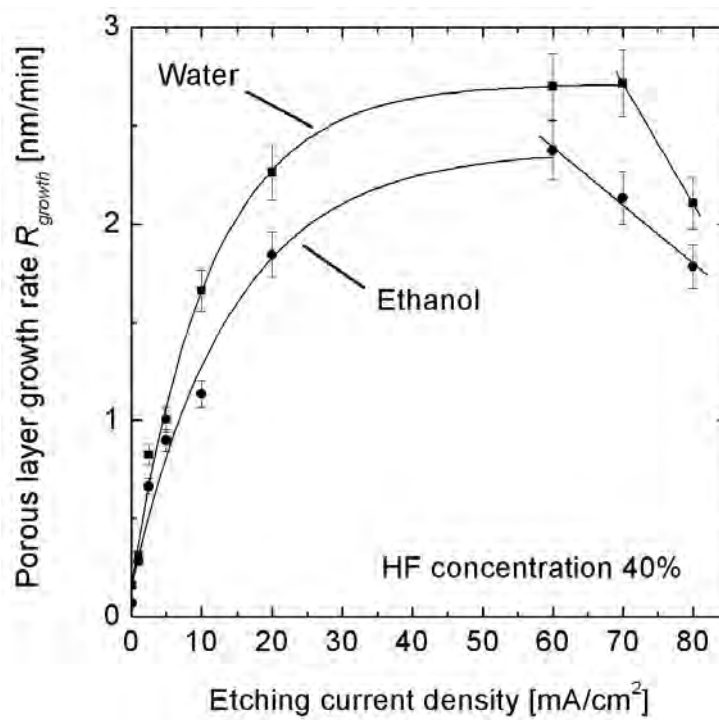


Figure 5.8: Porous layer growth rate vs. etching current density.

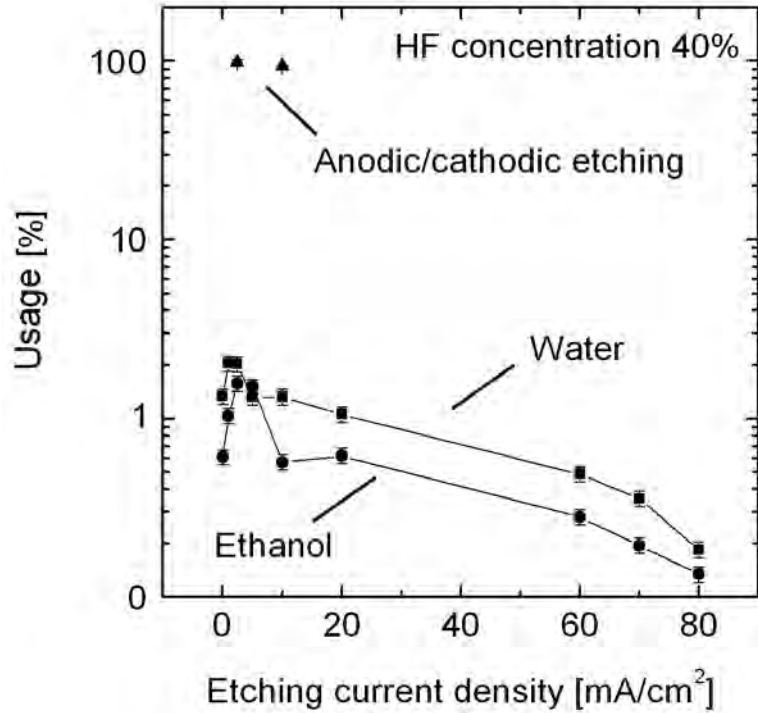


Figure 5.9: Usage vs etching current density for anodic PGe layers formed in aqueous and ethanoic based electrolytes with a HF concentration of 40 wt. %. In comparison, the usage value of two samples etched using anodic/cathodic etching is presented.

Aqueous solutions show higher growth rates R_{growth} than ethanoic solutions. As mentioned before, this effect is related to the increased dissolution rate of the porous layer in ethanol. Since R_{growth} is given by the difference between the R_{etch} and R_{diss} , the porous layer growth rate is limited by R_{diss} . Ethanoic electrolytes present high dissolution rates R_{diss} and the fast dissolution of the porous layer therefore limits R_{growth} . High etching current densities above 60 mA/cm² lead to a decrease of R_{growth} for both ethanoic and aqueous electrolytes due to the increasing R_{diss} . Etching current densities higher than 80 mA/cm² do not even allow porous layer formation as the increased R_{diss} simply leads to electropolishing of the wafer.

5.2.2 Substrate usage

Substrate thinning diminishes substantially the material conversion efficiency, i.e. the amount of material that is necessary to dissolve in order to obtain PGe. Equation 5.1 defines the substrate usage U [%] as the ratio of the growth rate to the etch rate. This is an important parameter, since it quantifies the volume efficiency for transforming non-porous bulk material into porous material.

$$U = \frac{R_{growth}}{R_{etch}} \cdot 100 \quad (5.1)$$

Low usage rates imply strong electropolishing of the already formed porous layer, thus yielding a thin substrate with a porous layer on its top. Electropolishing is not desirable as material costs increase drastically. Obtaining high usage rates is a key issue in order to permit potential cost and material savings derived from a subsequent layer transfer process. Figure 5.9 shows a semilogarithmic plot of the substrate usage of anodic porous Ge formation as a function of the etching current.

Since R_{growth} is around 2 to 3 orders of magnitude smaller than R_{etch} , the usage is very low. It lies in the range of 0.2 % to 2.0 %, showing thus very inefficient porous layer growth. Several μm of material are consumed in order to obtain a porous layer of a few hundreds of nanometers. However, higher usage values are obtained using a new etching technique called anodic/cathodic etching, which consists of alternating periodically the etching bias from anodic to cathodic.

Hydrogen passivation of the surface reduces substrate thinning. Turner carried out oscillographic investigations of the Ge surface by constantly changing the polarization direction [71]. He found that cathodic reactions proceed in two steps: Firstly the Ge oxide at the surface is reduced. Secondly, hydrogen atoms bond to Ge surface atoms. The surface is thereby passivated, the porous layer stops to grow, and germane (soluble or gas) compounds form at the surface of the cathode [70]. The reaction equation is:



Choi and Buriak produced PGe by changing once the etching bias from anodic to cathodic [4]. Fang *et al.* proposed a mechanism that increases the passivation of the Ge surface by switching the system periodically from anodic to cathodic bias [14]. The passivation provided by the cathodic step inhibits the dissolution of the already formed porous layer and avoids substrate thinning. However, the duration of the passivation is limited. It depends mainly on the etching current density of the subsequent anodic step and the electrolyte concentration. High etching current densities and electrolyte concentrations decrease the duration of the passivation effect. Typically, passivation lasts from 1 to 10 min. A new cathodic step is afterwards necessary in order to further passivate the surface. Figure 5.10 shows the etching current density and etching potential profiles in arbitrary units. The system is pulsed eight times from anodic to cathodic bias by changing the etching current density in order to passivate the surface.

Due to the increased passivation, R_{diss} decreases substantially, becoming almost zero. The passivation also affects R_{etch} , reducing the rate down to values similar to R_{growth} in the nm range. Since both, R_{growth} and R_{etch} , take similar values, the substrate usage increases substantially. Figure 5.9 shows that usage values in a range of 93 % to 98 % are obtained using this technique. The initial phase of porous layer growth, also called nucleation phase, causes substrate thinning until pore growth starts. This phase, common to all materials, usually removes a few microns of substrate until homogeneous nucleation is achieved. Higher usage values are therefore hardly possible due to initial substrate electropolishing.

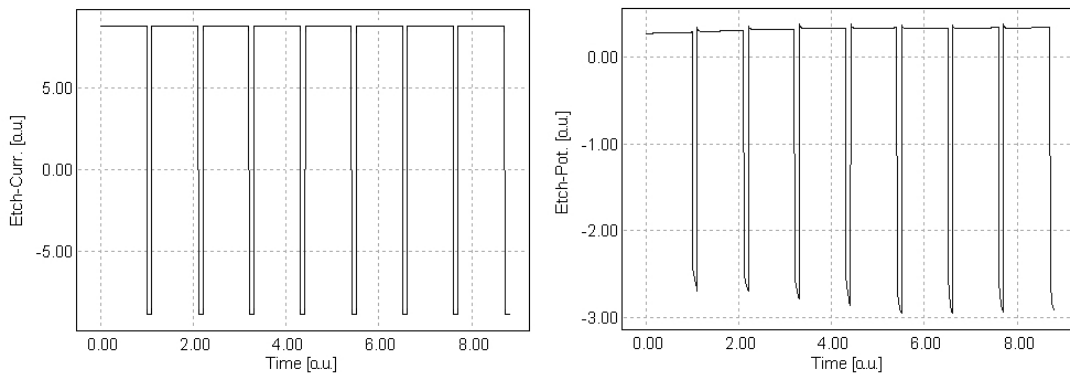


Figure 5.10: Etching profile in galvanostatic mode. The figure on the left hand side shows the applied galvanostatic profile, which periodically changes from anodic to cathodic bias. During anodic bias, the substrate is porosified, while during cathodic bias, the pore walls and the surface are passivated with hydrogen atoms. On the right hand side is shown the corresponding voltage-time profile.

5.2.3 Layer porosity

The porosity of a layer is defined as the ratio of the volume of all the pores in a layer to the volume of the layer without pores. It plays a very important role for lift-off processes, as it determines the thermal reorganization of the already formed porous layer in the subsequent annealing step during epitaxial growth.

The impact of the specific resistivity of the substrate and the etching current density on the porosity of the porous layers are investigated. The electrolyte concentration is set to HF 40 % wt. Figure 5.11 shows the porosity as a function of the specific substrate resistivity for two etching currents, 5 mA/cm² and 15 mA/cm². Porosity values in a range of 39 % to 67 % are obtained for specific resistivities in the 12-32 mΩcm range. Both porosity curves show a step-like shape. The porosity tends to saturate at its upper level when decreasing the specific resistivity.

The porosity of the PGe layer strongly depends on the etching current density. The porosity increases with increasing etching current density for a given specific resistivity value. Variations in the etching current density from 5 mA/cm² to 15 mA/cm² lead to strong variations in the porosity of the wafers from 38 % to 67 % for specific resistivity values of 31 mΩcm and 15 mΩcm respectively. Higher etching current densities increase the electric field strength, thus permitting more charge carriers to pass through the space charge region by tunneling and increasing the porosity. A similar effect is observed in the highly doped p-type mesoporous silicon case, where the porosity increases with increasing etching current density [40].

It is also observable that the porosity increases while decreasing the specific resistivity. This effect is a consequence of charge carriers tunneling through the space charge region, which is dependent on the doping of the substrate, i.e. the specific resistivity. With increasing doping density, the electric field increases, the width of the depletion region decreases, and the tunneling of charge carriers through the space charge region dominates. This effect has been also found in the highly doped p-type mesoporous silicon case.

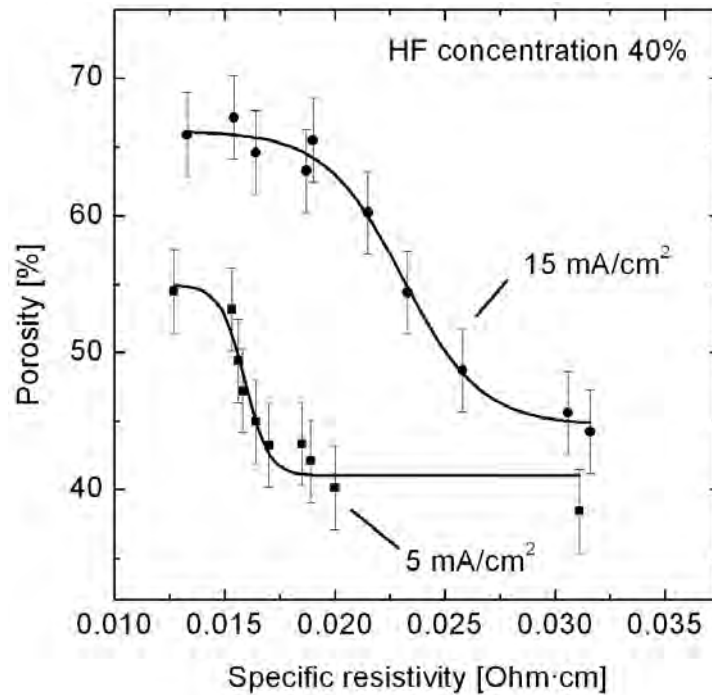


Figure 5.11: Porosity vs. substrate specific resistivity for two different etching currents. Note that the solid line is a guide to the eye.

Porosities lower than 35 % are likely to be suitable as starting layers for subsequent epitaxial deposition of multijunction solar cells [53]. Such starting layers will reorganize during annealing before the epitaxy, yielding thus a closed surface for the following epitaxial growth and lift-off. Layers with porosities larger than 35 % are likely to collapse during the reorganization process. Lower porosities than presented in Figure 5.11 are obtained by etching in highly concentrated electrolytes and by decreasing the etching current density. Low etching current densities, less than 3 mA/cm², and highly concentrated electrolytes above HF 40 wt. % are necessary in order to obtain porosities in a range below 35 %. Porosities in the 27.5 % range are obtained by anodizing the samples in HF 50 wt. % and decreasing the etching current density down to 1 mA/cm². However, due to the reduced etching current density, the porous layer growth becomes substantially slower and time consuming. The homogeneity of the porous layer thickness is also substantially reduced due to the lower sensitivity of the potentiostat for small etching current densities.

The dependence of the porosity on the electrolyte concentration is investigated for an etching current density of 5 mA/cm² and a specific resistivity of 13 mΩcm. Figure 5.12 shows the measured porosity for electrolyte concentrations in a range of 35 wt. % to 50 wt. %. The curve shows an almost linear decrease in the porosity from 58 % to 44 % by increasing the HF concentration in the electrolyte from 35 wt. % to 50 wt. %. This effect has been observed in porous Si as well [72],[73].

The porosity is assumed to be constant over the porous layer volume. However, this is only correct for short anodization times and thin layers. The HF concentration and renewal of fluorine atoms decrease due to diffusional limitations at the bottom of the

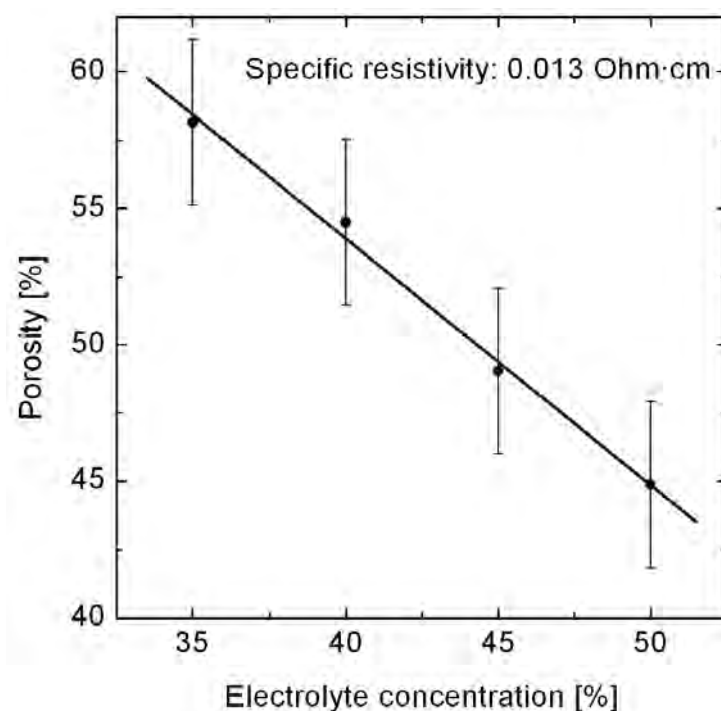


Figure 5.12: Porosity vs. electrolyte concentration for a specific resistivity of $13 \text{ m}\Omega\text{cm}$ and an etching current density of $5 \text{ mA}/\text{cm}^2$. Note that the solid line is a linear fit to the experimental data.

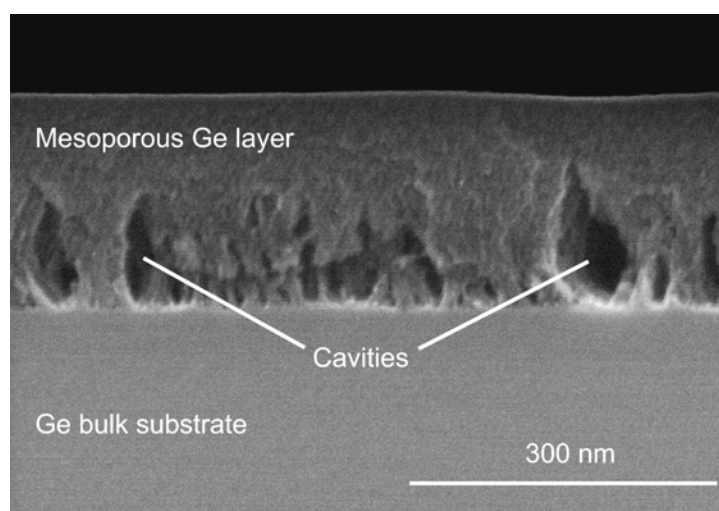


Figure 5.13: SEM cross section caption of a mesoporous Ge etched 22 hours in HF 50 wt. % with an etching current density of $0.5 \text{ mA}/\text{cm}^2$. The bottom of the porous layer presents an increased porosity caused by lower HF concentrations. The increase in the porosity drives to cavity formation.

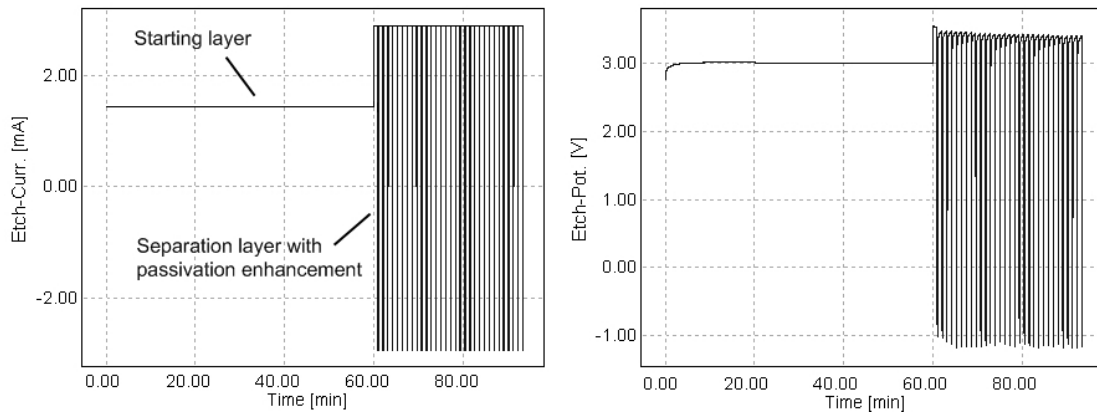


Figure 5.14: Etching profile in galvanostatic mode for electrochemical etching of porous double layers. On the left hand side it is shown the applied galvanostatic profile for the formation of a porous double layer. On the right hand side is shown the corresponding voltage-time profile.

porous layer while increasing the porous layer thickness and increasing the duration of the experiment. The porosity therefore increases with pore depths and time consuming experiments, hence showing a gradient in the porosity within the porous layer with a peak at the bottom of the porous layer. This effect is also observed in mesoporous Si [40]. In case of very long electrochemical etching experiments with very low etching current densities, the increase in the porosity drives in extreme cases to cavity formation as shown in Figure 5.13.

5.3 Mesoporous Ge double- and multilayers

The formation of mesoporous Si double layers occurs by varying the etching current density and the etching time as shown in Section 3.2. Depending on both parameters, the porosity and thickness of the porous layers are adjusted. Such porous double layers are of interest for layer transfer processes like the PSI process. However, in contrast to Si, a simple change in the etching current density does not lead to the formation of porous Ge double layers. Due to the constant thinning of the sample plus porous layer shown in Section 5.2.1, the starting layer dissolves into the electrolyte while etching the bottom layer, yielding thus a single porous layer on the top of a thinner substrate.

It is therefore compulsory to passivate the surface and pore walls with hydrogen in order to stabilize pore growth and avoid dissolution of PGe and substrate thinning. Fang *et al.* increased the passivation of the surface by switching the etching bias from anodic to cathodic [14]. It has been shown in section 5.2.2 that this technique is able to passivate the surface during the cathodic step. The pore walls and the surface are covered with hydrogen atoms, hence avoiding thinning. The passivation typically lasts from 0.5 min to 5 min, which makes it necessary to repeat the cathodic step in order to further passivate the surface of the pore walls and avoid thinning.

Alternate bias is used for producing porous double layers consisting of a low porosity layer at the wafer surface and a buried high porosity layer. Figure 5.14 shows the

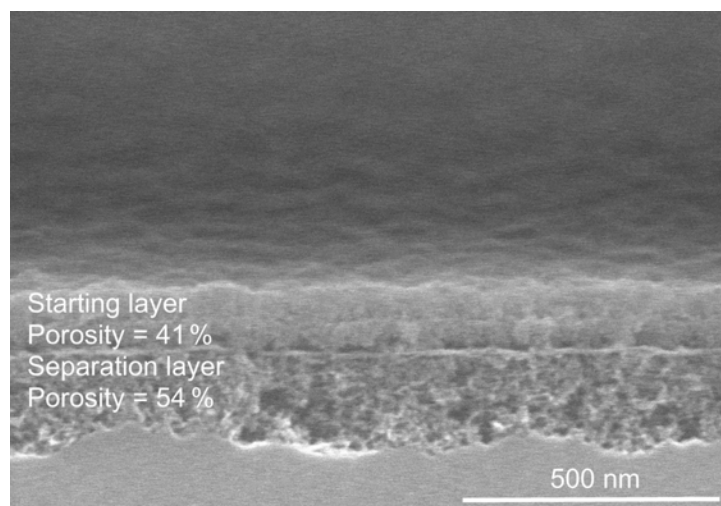


Figure 5.15: Mesoporous double layer with different porosities obtained from the etching profile presented in Figure 5.14.

etching profile of a porous double layer etched in galvanostatic mode. Firstly, the starting layer with low porosity is produced by applying a constant current density of 1.77 mA/cm^2 during 60 min. Lately, the system is pulsed 75 times from anodic to cathodic bias in order to passivate the pore walls and avoid substrate plus porous layer thinning while producing the highly-porous layer. The cathodic step lasts 6 seconds and is enough to passivate the surface of the starting PGe layer for more than one minute, avoiding thus thinning. Afterwards it is necessary to repeat the cathodic step in order to further passivate the pore wall surface. The buried highly-porous layer forms during anodic etching regime.

Figure 5.15 shows the sample etched with the etching profile shown in Figure 5.14. A uniform porous double layer is obtained. The specific resistivity of the substrate is $23 \text{ m}\Omega\text{cm}$. The porous layers are composed of micro and mesopores. The diameter of the pores in the starting layer lies in a range of 1 nm to 36 nm and the mean diameter of the pores is 13.2 nm as measured with imaging recognition software. The surface roughness is less than 50 nm. The diameter of the pores at the high porosity layer lies in a range of 5 nm to 50 nm. The mean diameter of the pores is 32.8 nm and the roughness at the PGe/Substrate interface is less than 100 nm.

The difference in the porosity of both layers is achieved by changing the electrolyte concentration and by varying the etching current density. The electrolyte concentration used for the starting layer is 50 wt. % and for the separation layer 35 wt. %. The etching current density is increased for the separation layer. The porosities of each single layer are measured separately. The starting and separation layers have a porosity of 41 % and 54 % respectively.

The fabrication of mesoporous multilayers is also possible by applying alternating bias. Figure 5.16 shows a mesoporous Ge multilayer with a thickness of about 400 nm consisting of three single mesoporous layers with varying thicknesses and porosities in a range of 27 % to 47 % for the starting, second, and third layer respectively. The porosity step is obtained by varying the etching current density and the HF concentration in the electrolyte. The electrolyte used is HF 50 wt. % for the starting layer and HF 40

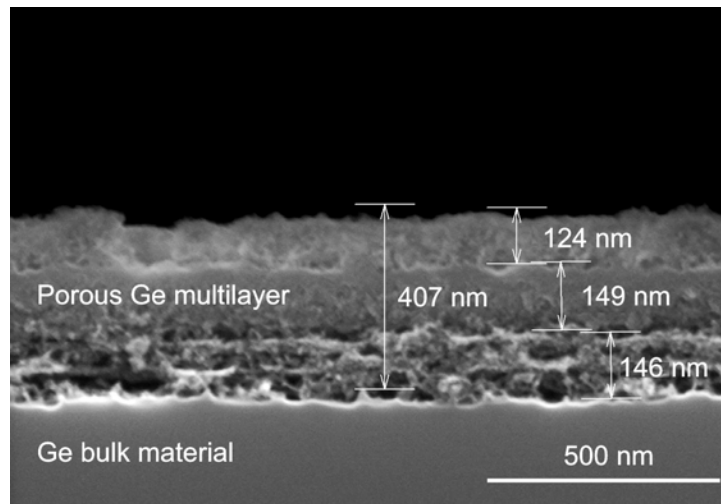


Figure 5.16: Mesoporous Ge multilayer composed of three layers. The multilayer has a thickness of about 400 nm. The thickness of the starting third layer is approximately 125 nm and 150 nm for the second and third layers. The porosity values are 27 %, 35 %, and 47 % for the starting, second, and third layer respectively.

wt. % for the second and third layers.

Figure 5.17 shows the etching current density vs. time profile used for the multilayer presented in Figure 5.16. The starting layer is formed by constantly alternating the etching bias during 27 min from 0.9 mA/cm² to -0.9 mA/cm². The system is pulsed 25 times from anodic to cathodic bias, where the cathodic step lasts 5 sec and the anodic step 1 min. The electrolyte used is HF 50 wt. %. The second layer forms by alternating the etching bias 35 times from 1.4 mA/cm² to -1.4 mA/cm². The cathodic steps lasts 7 sec and anodic step 1 min. The entire process for the second layer lasts approximately 39 min and the electrolyte used is HF 40 wt. %. The third layer is produced by alternating 35 times from 2.9 mA/cm² to -2.9 mA/cm² with an entire duration of 38 min. The anodic step lasts 1 min and the cathodic step 9 sec. The electrolyte used for the third layer is HF 40 wt. % and the complete process for the multilayer takes 103 min.

The procedure is scalable and allows the formation of multilayers with additional layers with varying porosities by subsequently adding etching steps. The etching current density, the specific resistivity of the substrate, and the electrolyte concentration determine the porosity of each single layer.

5.4 Macropore formation

Germanium shows macropore formation while electrochemical etching in HCl, H₂SO₄, and in HF-based electrolytes with a concentration below 30 wt. %. Strong electropolishing of the Ge surface always occurs in all electrolytes and concentrations, thus yielding a thinner substrate after etching. Different macropore shapes, sizes, and orientations form depending on the etching current density, electrolyte concentration, and electrolyte used.

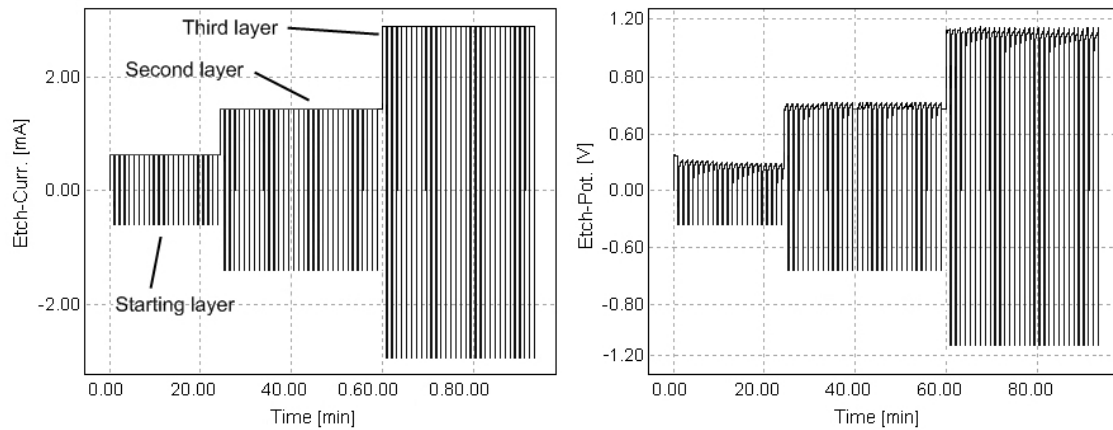


Figure 5.17: Etching profile corresponding to Figure 5.16. The figure on the left hand side shows the etching current density. Alternating bias permits pore wall passivation and avoids substrate thinning. On the right hand side, the figure shows the corresponding potential profile, which is automatically adjusted. The changes in the etching current density and electrolyte concentration determine the porosity of the layers.

HCl aqueous electrolytes show pyramid formation at the surface and oxide accumulation. Electrolytes with a HF concentration below 5 wt. % present H^- surface passivation as suggested by Fang *et al.* [14]. Figure 5.18 shows pyramid and oxide formation obtained in HCl 3 wt. %. The oxide accumulations present at Figure 5.18 are water soluble and they were not removed deliberately for their analysis.

OH^- and Cl^- passivation dominate for highly concentrated electrolytes exceeding 5 wt. %. Randomly distributed macropores appear with $\{110\}$ stopping planes. Macropores grow locally at the surface where small crystal defects, a badly passivated atom, a dangling bond, or just an abraded point on the surface are located. Prior to pore formation, the voltage increases as long as pore growth does not start. Thus breakdown occurs when pore growth starts. The etching current flows through the defects etching the sample and forming the macropore.

Ethanoic-based electrolytes do not differ from aqueous electrolytes and present similar results to HCl aqueous electrolytes. The addition of organic compounds like DMF or DMSO enhances the crystallographical properties and macropores grow following the $\langle 111 \rangle$ direction. Crystallographically-oriented macropores are randomly distributed throughout the surface of the sample in macroporous accumulations with varying shape and size. New defects and dangling bonds appear during pore etching. Pore wall passivation is difficult during etching. Therefore new defects appear at the pore surface and cannot become passivated. As a consequence, pores start to grow all together in pore domains or "islands". Figure 5.19 shows a typical crystallographically-induced pore island with pores growing into the depth up to 60 μm . Pores grow in the $\langle 111 \rangle$ direction and stopping planes are $\{110\}$.

Pore islands are randomly distributed throughout the surface and separated from each other. The rest of the substrate remains unaffected and macropores only grow locally in pore islands. Their distribution depends on the starting passivation and surface defects.

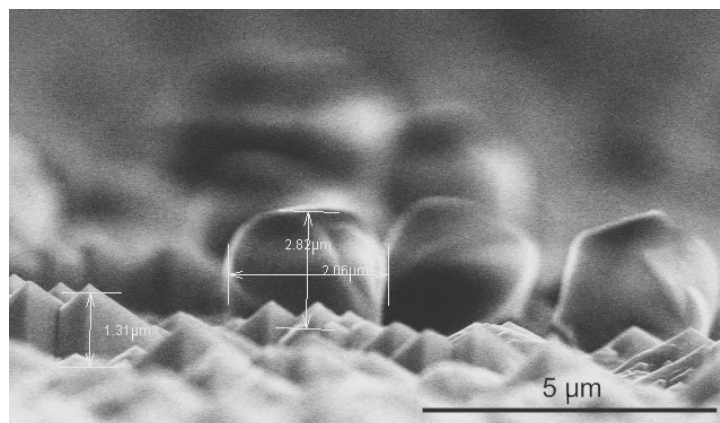


Figure 5.18: Surface textured with pyramids and large oxide accumulations not rinsed deliberately. Etched 120 min at 1 mA/cm² in HCl 3 wt. %.

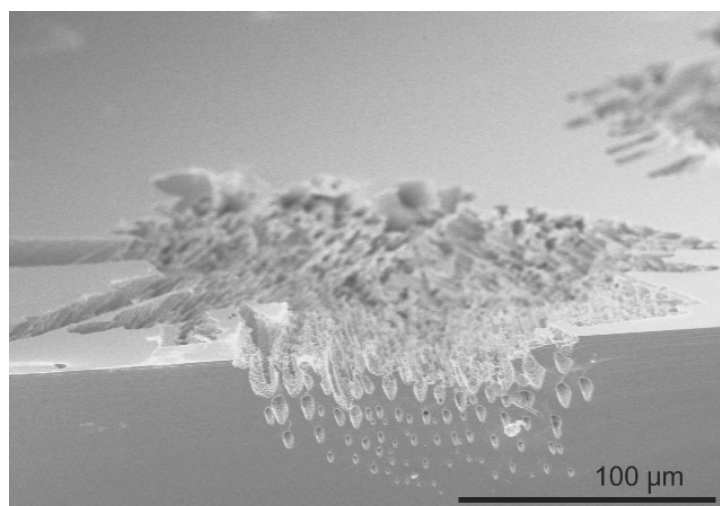


Figure 5.19: Crystallographically-oriented pore island. Etched 90 min at 2.5 mA/cm² in HCl 5 wt. % in DMSO.

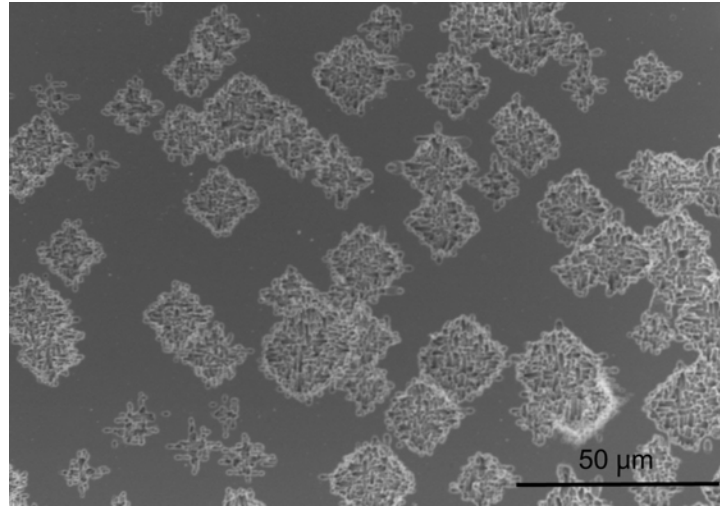


Figure 5.20: Nucleation enhancement by combining current ramping and surface passivation.

Homogeneous nucleation is a major concern for macropore etching. Fang *et al.* applied different methods for nucleation optimization, like current ramping or etching rough surfaces rather than polished surfaces in order to avoid pore islanding and achieve a good nucleation throughout the surface [14]. The starting passivation of the surface additionally influences the nucleation. Figure 5.20 shows the combination of both effects, i.e. current ramping and homogeneous passivation prior to pore formation.

The experiments carried out in HF electrolytes with low concentration (in water or ethanol) present similar results to the HCl case, yielding a uniform pyramid formation in the {110} plane throughout the surface. Pyramids form at the surface with sizes varying in a range of 250 nm to 5 μm . The obtained etch pits are similar to those presented by Flammand *et al.* [8]. Strong electropolishing effects and crater formation occur while increasing the electrolyte concentration from 10 wt. % up to 30 wt. % or applying etching current densities exceeding 5 mA/cm^2 .

5.5 Summary and conclusions to Chapter 5

This chapter has presented electrochemical etching experiments for the production of porous Ge. The use of highly concentrated HF-based electrolytes with a concentration exceeding 30 wt. % shows mesoporous Ge layer formation. Reproducible and uniform mesoporous layers with varying thicknesses up to 700 nm are obtained. The formation of mesoporous layers drives to a constant dissolution of the already formed porous layer, yielding a thinner substrate with a porous layer on its top. The dissolution rate of the already formed PGe lies in the range of 0.011 $\mu\text{m}/\text{min}$ to 1.33 $\mu\text{m}/\text{min}$ for etching current densities of 0.1 mA/cm^2 to 80 mA/cm^2 respectively. The growth rate of the porous layer lies in the range of 0.071 nm/min to 2.7 nm/min . In comparison to aqueous electrolytes, ethanoic solutions do have a higher dissolution rate, thus yielding a thinner sample. The porosity of the mesoporous layer lies in a range of 25 % to 65 % for specific resistivity values in a range of 32 $\text{m}\Omega\text{cm}$ to 20 $\text{m}\Omega\text{cm}$.

Changes in the etching bias passivate the pore walls and avoid substrate thinning. By means of alternating from anodic to cathodic bias, the substrate usage increases from values in a range of 0.002 to 0.02 for anodically etched samples to values of 0.98 for samples using this technique. Well defined mesoporous double layers are obtained by switching the etching bias. The porosity of the starting layer is 41 % and the porosity of the separation layer is 54 %. Such double layers are susceptible of being used for lift-off processes similar to the PSI process. Multilayer formation is possible by applying successive alternating bias steps.

Electrolytes with low HF concentration show pyramid formation and strong electropolishing effects, but no porous layer formation. Electrochemical etching using HCl-based electrolytes shows macropore formation. Strong electropolishing effects take place at the semiconductor-electrolyte interface and lowly concentrated electrolytes and etching currents are needed in order to avoid surface damage. Crystallographically-induced pores growing in the $\langle 111 \rangle$ direction have been obtained, where $\{110\}$ planes act as stopping planes. Nucleation is troublesome and the starting passivation and current-time etching profiles play an important role for obtaining homogeneous nucleation. No porous layers have been produced using HCl-based electrolytes and only dispersed pore accumulations are obtained with optimized parameters.

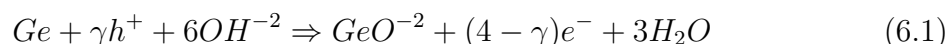
Chapter 6

Theoretical model for anodic etching of Ge

This chapter presents a new model of anodic dissolution of germanium in highly concentrated HF solutions. The model accounts for the electrochemical divalent and tetravalent anodic dissolution of Ge as well as for chemical and electrochemical dissolution of Ge oxides in water and HF. The experimental observations and measurements that suggest the model are presented. The dissolution valence of the electrochemical etching process is calculated using Faraday's law of electrolysis, confirming as well the proposed mechanism. The porous layer dissolution rate is used to determine the threshold in etching current at which the Ge dissolution process changes from a tetravalent to a divalent mechanism. The band diagram within the semiconductor is studied and the differences between Si and Ge are investigated. Finally, based on electronegativity differences, the formation of mesoporous Ge in highly concentrated HF-based electrolytes is explained.

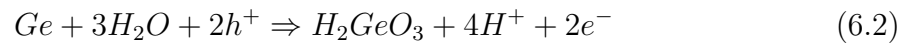
6.1 Theoretical background

The electrochemical etching and the anodic dissolution of Ge were intensively studied in the early stages of semiconductor electrochemistry. Jirsa first published in 1952 an investigation regarding anodic dissolution of Ge in dilute acids and alkalis [64]. He showed that Ge dissolves in the form of tetravalent complex ions, i.e. the number of valence electrons of the overall reaction is four. Therefore, four charges are required to remove a Ge atom from the bulk substrate. Further investigations confirmed that holes participate in the anodic dissolution of p-type Ge substrates [34],[65],[66]. These investigations proposed the following overall reaction equation for the anodic dissolution:



Equation 6.1 states that four charges are needed for the dissolution of a Ge atom, so that $0 \leq \gamma \leq 4$. By means of the thin slice method, a value $\gamma = 2.4$ was measured for electropolishing experiments [66], hence confirming that Ge dissolution does not

only take place simultaneously with the diffusion of holes from the bulk, but also with injection of electrons via the conduction band. Later, Turner proposed in 1956 a model that described the anodic dissolution and cathodic reduction of Ge in acidic and neutral solutions while studying changes in the polarization in sulphuric acid [67]. The model suggests that the anodic dissolution of Ge takes place in two successive steps: In the first step, two holes coming from the bulk substrate break the covalent bonds and the Ge substrate present at the electrolyte boundary dissolves into the solution with hydroxyl radicals attached to it. In the second step, the dissolved Ge atom reacts with water to form metagermanic acid (H_2GeO_3), which remains into the electrolyte. Finally, the Ge surface oxidizes again with water, leaving a hydroxyl-passivated surface. The overall equation of the reaction is:



The first step is slow, as it is determined by the diffusion of holes from the bulk into the substrate-electrolyte interface, thus limiting the dissolution rate. This model states that four charge carriers, i.e. two electrons and two holes, are needed to remove a Ge surface atom from the bulk. At high anodic etching current densities, the h^+ is obviously no longer rate determining. The dissolution rate increases drastically and Ge cannot longer dissolve, forming thus white GeO_2 and yellowish GeO . The model has obviously some defects, as it neglects the possibility of a reaction with more than two holes. Furthermore, the oxidation of Ge is more complicated than presented and the model did not account for the possibility of anodic dissolution in HF electrolytes and their influence.

Beck and Gerischer proposed in 1959 a detailed mechanism for the anodic dissolution of Ge in alkaline solutions. The model stated that the kinetics of Ge dissolution depend, not only on the applied etching current density, but on the concentration of hydroxyl ions in the electrolyte [68],[69]. The model only accounted for the tetravalent dissolution of Ge, hence being necessary four charges for removing an atom from the substrate. Additionally the model did not account for Ge dissolution in highly acidic HF electrolytes and pore formation.

Except for these models, the electrochemical dissolution mechanisms of Ge have not been further investigated. Additionally, the anodic dissolution models are incomplete, as they do not account for etching and pore formation in highly concentrated HF solutions [21],[22].

6.2 Experimental observations

Depending on the pH of the electrolyte, different water soluble and insoluble oxides and oxide compounds form at the semiconductor-electrolyte interface [77],[78]. GeO and GeO_2 always appear as solids at the Ge-electrolyte interface. Strongly acidic solutions with very low pH values show $GeOOH^-$ formation as well. For neutral or lightly alkaline solutions, $Ge_x(OH)_{2x}$ forms at the electrolyte boundary instead of $GeOOH^-$. In highly alkaline electrolytes, other metagermanic compounds are formed rather than

$\text{Ge}_x(\text{OH})_{2x}$ or GeOOH^- .

GeO_2 , i.e. Ge with valence number IV, occurs in three different phases: One amorphous and two crystalline (hexagonal and tetragonal) [79]. Two phases are water-soluble and thus dissolve automatically in water or HF as they are in contact with the electrolyte. In contrast to SiO_2 , which is not water soluble and can only be removed with HF, the GeO_2 tetragonal phase is not water soluble and has a limited solubility in HF. Similar considerations apply to GeO , i.e. Ge with valence number II. It presents three phases and only one of them is not water soluble. The non-soluble phase has a limited solubility in highly concentrated HF. The solubility of Ge oxides thus depends on the pH, electrolyte concentration, and etching current density. The addition of HF reduces the insoluble phases of GeO (II) and GeO_2 (IV) to water-soluble germanates.

Ge oxides are partially water-soluble, but the insoluble phases of Ge oxides are found to be resistant to etching experiments with highly concentrated electrolytes with a concentration of HF 50 wt. % and low etching current densities for a few hours. Characteristic yellow GeO is observable after the etching experiments if low etching current densities are applied, thus proving that insoluble oxide phases grow. If the etching current density is increased substantially for values above 10 mA/cm^2 , yellow GeO does not form and oxygen traces are no longer observable with EDX.

The polymerization of GeO insoluble is also observable. If GeO is in contact with the atmosphere, it oxidizes to water-soluble GeO_2 or other water-soluble oxide compounds, changing its color to brown. As a consequence, the GeO still present at the porous layers becomes oxidized in air and dissolves automatically in subsequent water or HF dip.

The etching process and pore formation in Ge is very slow in comparison to Si substrates. Oxide growth during etching slows down the dissolution process. Insoluble Ge phases additionally delay the process at low etching current densities as they have a limited solubility into the electrolyte. The solubility increases with increasing etching current density and electrolyte concentration.

Simultaneously to the anodic dissolution and pore formation, hydrogen gas evolution is observed at the germanium anode. The amount of H_2 evolving from the electrode increases linearly with etching time. Low etching current densities almost do not show hydrogen formation. Only residual hydrogen formation is observed while applying very low etching current densities below 2.5 mA/cm^2 .

Figure 6.1 shows the I-V curve obtained for a Ge sample immersed in HF 40 wt. %. The sample has the expected Schottky diode shape. The I-V curve in Si shows a local minimum and a local maximum at the critical etching current density which is caused by the change in the dissolution valence from divalent to tetravalent [40],[44]. The stirring effect caused by H_2 bubble evolution during the divalent dissolution mechanism stops when the tetravalent dissolution mechanism dominates, causing the mass transfer rate to reduce and hence, the I-V curve to have its typical local maximum and minimum. The local maximum and minimum are not observable in the Ge case. Note that the slope and shape of the I-V curve is strongly determined by the resistance in the experimental setup.

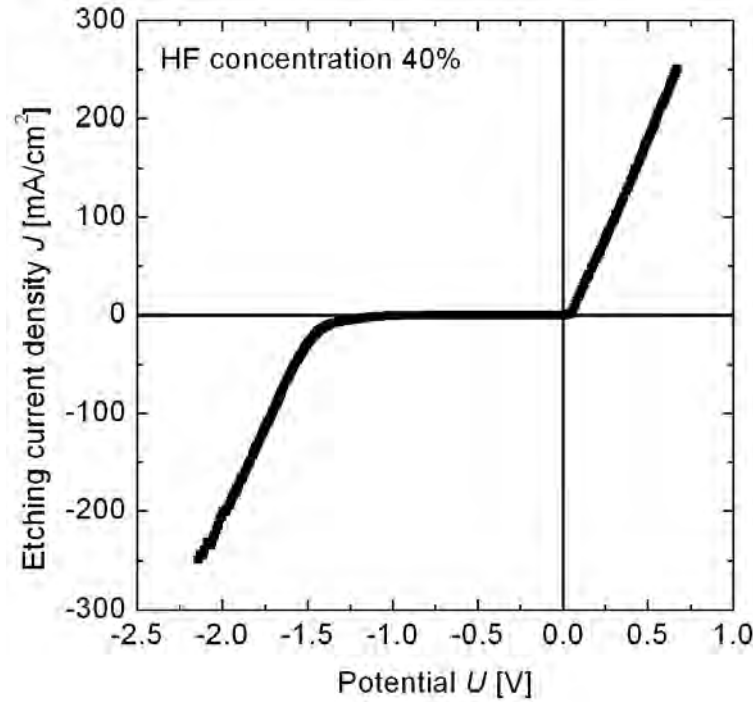
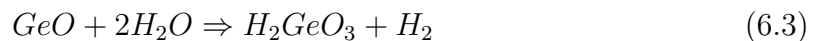


Figure 6.1: I-V curve. Specific resistivity: 13.9 mΩcm. Note that the curve has been measured for a HF with a concentration of 40 wt. %.

6.3 Anodic dissolution model

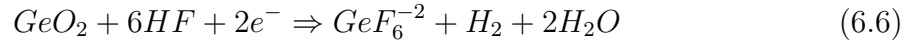
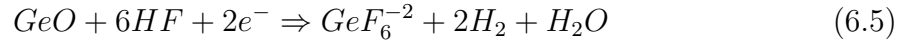
Based in the experimental observations carried out during this work, a mechanism of anodic dissolution of Ge is proposed. This model accounts the tetravalent and divalent dissolution of Ge and likewise, chemical and electrochemical dissolution of Ge oxides in water or in HF. In contrast to Si [40],[43], the tetravalent dissolution is the main dissolution mechanism for low current densities below 7.5 mA/cm². With increasing etching current density, the divalent dissolution starts to dominate and at high current densities, the divalent dissolution becomes the main dissolution mechanism.

Oxide dissolution: As mentioned above, water-soluble phases of GeO and GeO₂ react automatically with water as the sample is immersed in the electrolyte and dissolve. As a reaction product, water-soluble metagermanic acid is produced, which dissolves automatically in the electrolyte. Equations 6.3 and 6.4 show the dissolution reactions. Note that hydrogen evolution is possible, agreeing with the observation of hydrogen formation for very low etching current densities.

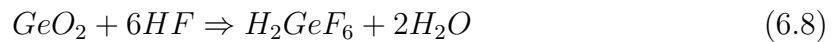
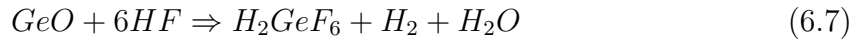


Water-insoluble phases of GeO and GeO₂ only dissolve in HF. However, the solubility of water-insoluble Ge oxides is limited in HF and depends on the electrolyte

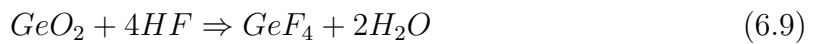
concentration and the applied etching current density. The dissolution of the water-insoluble phases of GeO and GeO₂ can occur via electrochemical etching of the Ge oxides as shown in Equations 6.5 and 6.6. These reactions are very sensitive to changes in the etching current density and also foresee hydrogen formation.



The dissolution of water-insoluble Ge oxides can furthermore occur via chemical dissolution in HF as shown in Equations 6.7 and 6.8. In the case of very low etching current densities and long experiments, the solubility is only limited by the HF concentration. Highly concentrated electrolytes are able to dissolve a larger amount of insoluble Ge oxides. Hydrogen gas formation is also possible with this dissolution reaction.

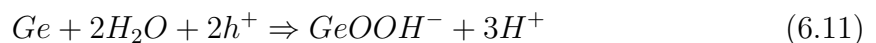


The chemical dissolution of Ge oxides in HF can occur via an intermediate stage, where the Ge oxide first reacts with HF to produce GeF₄ and it further reacts with water to produce water soluble GeO₂ and H₂GeF₆. Equations 6.9 and 6.10 show the reactions proposed.

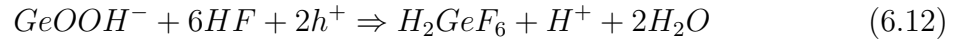


Tetravalent dissolution: Ge atoms dissolve mainly via the tetravalent dissolution mechanism for low etching current density values. Similarly to Si, the tetravalent dissolution reaction consists of two steps. In the first step, oxide grows at the surface of the substrate as Ge gets in contact with water. As mentioned above, GeOOH⁻ is the oxidation reaction product in acidic solutions. This step is slow, as the amount of holes is limited due to the diffusion or thermionic emission of holes through the space charge region as shown in Equation 6.11.

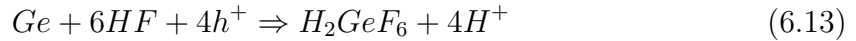
Step 1:



Step 2:



In the second step, GeOOH^- gets electrochemically etched in HF as shown in Equation 6.12. The overall equation for the tetravalent dissolution presented in Equation 6.13 shows that in this case, four charge carriers are needed to remove a Ge atom from the substrate. Note that similarly to Si, the tetravalent dissolution of Ge does not foresee hydrogen formation.



Divalent dissolution: Similarly to Si, Ge can dissolve in HF-based electrolytes through a divalent dissolution mechanism. This reaction consists of six steps shown in Figure 6.2 starting from a hydrogen passivated Ge surface, due to substrate immersion in HF. In the first step, an HF_2^- ion present at the electrolyte reacts with a Ge atom in the presence of a hole coming from the substrate bulk, enabling thus the nucleophilic substitution of a hydrogen atom by a fluorine atom. This step is responsible for the porous structure and limits the dissolution rate. The dissolution rate increases with the applied etching current density and electrolyte concentration because the dissolution of Ge requires a charge transfer through the interface and HF_2^- ions for the nucleophilic attack.

In steps two and three, the remaining hydrogen atom is replaced by a fluorine atom under injection of an electron, producing a H_2 molecule which evolves from the surface of the substrate. Steps four and five show that HF_2^- ions attack Ge back-bonds, being thus capable of removing the Ge atom from the bulk substrate. The Ge atom is thus dissolved in the electrolyte and the Ge bulk surface becomes H-passivated. By binding two F^- ions, the dissolved GeF_4 molecule reacts to GeF_6^{2-} . Equation 6.14 shows the overall reaction equation for the divalent dissolution of Ge. Note that the divalent dissolution mechanism foresees hydrogen formation.



6.4 Results and model interpretation

Turner reported in 1967 that the Ge dissolution valence is four at low current densities and it becomes two for higher etching current densities, which agrees with the model regarding dissolution valence [71]. The experiments show residual hydrogen evolution for low etching current densities below 2.5 mA/cm². This agrees with the electrochemical dissolution of germanium insoluble oxides, which foresees hydrogen evolution. The formation of H_2 stops with increasing etching current density up to etching current

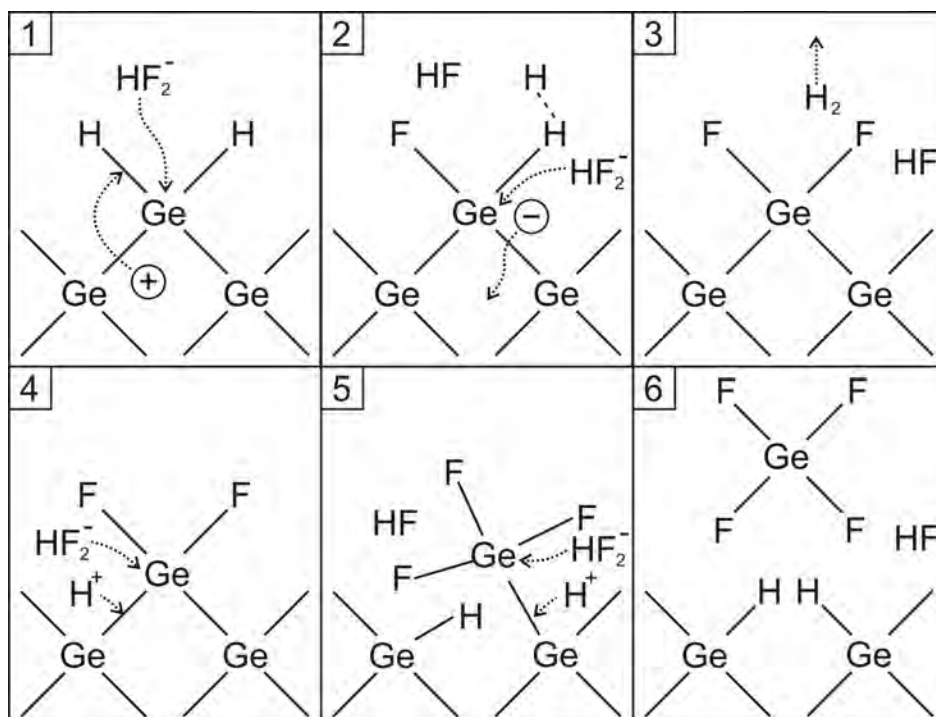


Figure 6.2: Divalent dissolution of Ge in highly concentrated HF. Two charge carriers are needed in order to remove one Ge atom from the substrate. Figure adapted from [39].

densities in the 7-10 mA/cm² range. This is related to the tetravalent dissolution mechanism, which does not predict hydrogen formation. Under anodic bias, H₂ formation is only possible if Ge is dissolved in the divalent state. Hydrogen bubbles form if etching current densities above 10 mA/cm² are applied, thus suggesting that the divalent dissolution mechanism is dominating.

The I-V curve shown in Figure 6.1 supports the assumption regarding the dissolution valence. In contrast to Si, the change in the dissolution valence in Ge does not imply a reduction in the mass transfer rate. The change from tetravalent to divalent dissolution mechanism does not cause a reduction in the mass transfer rate reduce because hydrogen formation first starts with divalent dissolution. As a consequence, the I-V curve does not show any local minimum and maximum similar to the typical I-V curves in silicon. A constant slope in the positive quadrant is observed, validating thus the considerations of the model regarding valence.

The presence of oxides at low and very low etching current densities after etching also suggests that the tetravalent dissolution mechanism dominates for these etching current density regimes. Ge samples with applied etching current densities exceeding 10 mA/cm² do not show oxide formation after etching. High etching current densities dissolve more amount of insoluble Ge oxides and the divalent dissolution becomes the main Ge dissolution mechanism. The divalent dissolution mechanism of Ge is a very fast process which allows a quickly atom removal from the surface. As a consequence, anodic dissolution and porous formation rates increase drastically.

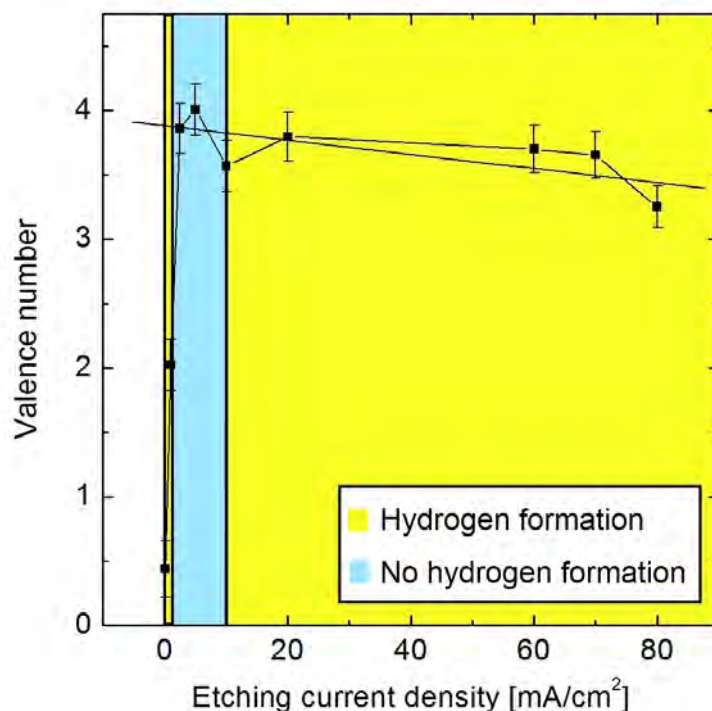


Figure 6.3: Valence number vs. etching current density calculated from experimental results using Faraday's law of electrolysis. The valence numbers presented are the mean values of all of the experiments carried out. The solid line is a linear fit of etching current density values exceeding 2.5 mA/cm^2 . The blue coloured region represents the etching current density values at which hydrogen evolution is not observed. The yellow coloured region represents the etching current density values at which hydrogen evolution from the substrate is observed.

6.5 Valence number calculation

The dissolution valence of the electrochemical etching experiments is determined in order to validate the model. According to Faraday's law of electrolysis shown in Equation 4.3, the mass of a substance altered at an electrode during electrolysis is directly proportional to the quantity of electricity transferred to the electrode.

Since divalent and tetravalent dissolution are the two parallel dominant and competing mechanisms, the dissolution model predicts a dissolution valence value between two and four with a decreasing tendency in the valence from four to two. At low etching current densities, the tetravalent dissolution (valence four) dominates and valence values closer to four are expected. With increasing etching current density, the divalent dissolution starts to dominate and the valence shall decrease. Figure 6.3 shows the calculated valence number with Faraday's law as shown in Section 4.3.4 for different etching current densities.

The valence number lies in the 0-2 range for very low etching current densities below 2.5 mA/cm^2 although values close to four are expected. The accuracy of such a simple method is limited while dissolving very low amounts of material. Therefore, unreal valence number values between zero and two are obtained. The experiment duration

increases up to more than 20 hours in case of very low etching current densities. The effect of chemical dissolution of native oxides or water-soluble oxides formed during electrochemical etching in water or HF cannot be neglected as shown in Section 5.2.3 during cavity formation in very long experiments. Ge atoms dissolve electrochemically but simultaneously, oxides formed during electrochemical etching further dissolve either chemically following the reaction mechanisms shown in Section 6.3.

The model does not predict hydrogen formation with tetravalent dissolution. However, hydrogen formation is observed experimentally for very low etching current densities. This observation confirms the chemical dissolution of electrochemically-formed oxides during Ge atom dissolution, as the model predicts hydrogen formation during chemical dissolution of Ge oxides.

Etching current densities exceeding 2.5 mA/cm^2 and below 10 mA/cm^2 show valence numbers increasing up to about four. This fact agrees with the model prediction that states that low etching current densities dissolve via tetravalent dissolution mechanism. No hydrogen evolution is observed, thus agreeing with the tetravalent dissolution mechanism, that does not foresee hydrogen formation. On the contrary, etching current densities exceeding 10 mA/cm^2 show strong hydrogen bubble formation. This fact suggests that the divalent dissolution dominates for this etching current density range. The slight decreasing tendency of the linear fit shows an increase in the divalent dissolution. This agrees with the model and with Turner's statement regarding Ge dissolution valence [71].

Figure 5.7 shown in Section 5.2.1 represents the dissolution rate R_{diss} measured for different etching current densities for ethanoic and aqueous electrolytes. Two different etching regimes are identified in the semilogarithmic plot of the dissolution rates of the PGe layer: Below and above 7.5 mA/cm^2 . The tetravalent dissolution mechanism is a slow dissolution process due to intermediate oxide formation. On the contrary, the divalent dissolution mechanism is a much faster dissolution process. The drastic change in the dissolution rate at 7.5 mA/cm^2 suggests that the etching mechanism has changed from tetravalent to divalent. This etching current density value nearly corresponds as well to the value at which hydrogen formation stops, hence confirming the change in the dissolution mechanism.

6.6 Valence band simulation

Several authors have suggested that electropolishing in Ge is caused by a leakage current during electrochemical etching, which causes the already formed porous surface to dissolve into the electrolyte [9],[14]. The computer program AFORS-HET created at the Helmholtz Zentrum Berlin is commonly used for the numerical simulation of heterojunction solar cells and measurements [76]. AFORS-HET additionally permits the simulation of band diagrams of metal/semiconductor interfaces, which behave similarly to electrolyte/semiconductor interfaces as shown in Section 2.2.3.

Figure 6.4 shows the simulation of the band bending diagram within a Si electrode as it is in contact with a metal. This simulation serves as a reference for the Ge electrode, as it is well known that porous Si formation does not lead to electropolishing of the surface excepting the nucleation phase prior to porous formation. The doping

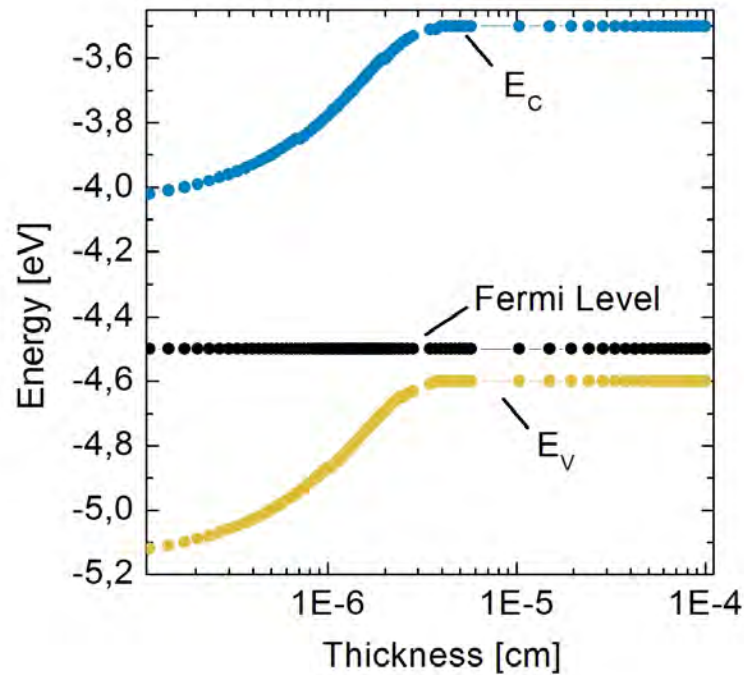


Figure 6.4: Band bending within a Si electrode/metal interface with same doping concentration as the experimental Ge samples. The metal contact is placed at the left side of the graphic and it is not drawn.

Material	Electronegativity
Germanium	2.01
Silicon	1.9
Fluorine	3.98
Chlorine	3.16
Sulphur	2.6

Table 6.1: Electronegativity values of different atoms. Data from [74].

concentration of the substrate is $7 \cdot 10^{17} \text{ cm}^{-3}$, characteristic of Ge samples used in the experimental work. The applied etching current density is 5 mA/cm^2 , a typical etching current density value used experimentally for pore formation. The metal contact is not shown and is located at the left side of the image with a work function placed at a level of -4.5 eV and equal to the Fermi level within the semiconductor.

Diffusion and thermionic emission of holes through the SCR are the dominant mechanism for mesoporous Si formation in p-type substrates with doping densities below 10^{18} cm^{-3} . The width of the SCR extends up to approximately 50 nm and the energy difference is about 0.5 eV . The tunneling probability is $4.38 \cdot 10^{-235}$ as calculated with the simulation parameters with the equation presented in [75] and therefore negligible. The wide SCR and the pronounced band bending limit spontaneous diffusion and thermionic emission of holes through the SCR and hence avoid the presence of a leakage current that could cause electropolishing.

Figure 6.5 shows the simulation of a Ge band bending in a Ge/metal interface

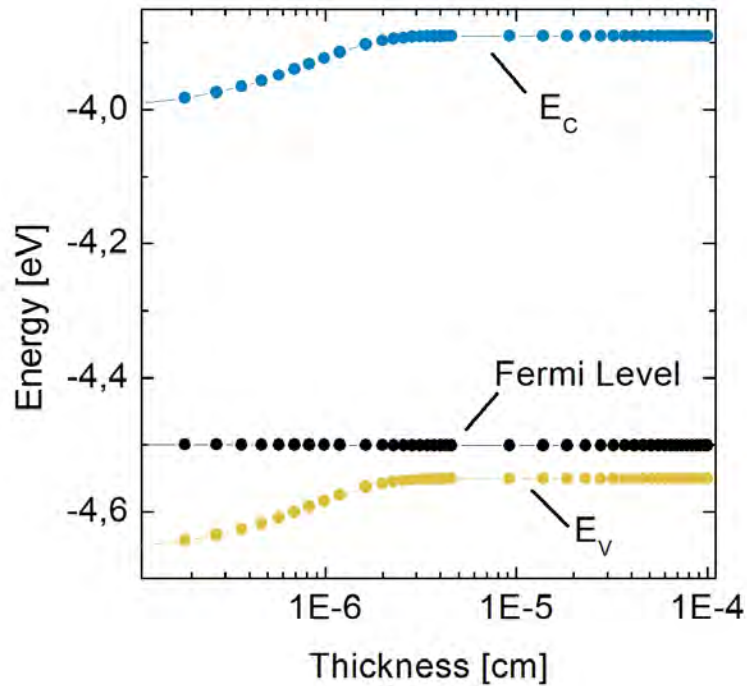


Figure 6.5: Band bending of a Ge/metal interface. The doping concentration of the substrate is $7 \cdot 10^{17} \text{ cm}^{-3}$. The metal contact is placed at the left side of the graphic and it is not drawn.

with the same doping concentration as in the Si simulation. The width of the SCR extends up to approximately 35 nm and the energy difference is about 0.1 eV. The tunneling probability is $1.33 \cdot 10^{-52}$ and therefore also negligible. Ge shows a much flatter band bending and a reduced SCR width. Ge hence allows a much easier charge carrier diffusion or thermionic emission from the semiconductor bulk into the interface through the SCR. As a consequence, a much larger hole density is available at the semiconductor surface, the so-called leakage current, that causes electropolishing as suggested in References [9],[14].

6.7 HF electrolytes for mesoporous formation in Ge

Ge is a very stable and insoluble material and it does not readily react with other substances and strong acids like sulphuric or hydrochloric acid. Mesoporous formation of Ge, as well as of Si, is only possible in HF solutions. A possible explanation for this fact could be related to the electronegativity differences between F and Ge. The electronegativity is a concept introduced by Pauling, which describes, on a relative basis, the power of an atom or group of atoms to attract electrons from the same molecular entity. If the electronegativity difference of two atoms is lower than 1.7, the bond is covalent. A chemical bond is said to be ionic if the electronegativity difference exceeds 1.7. Table 6.1 presents some electronegativity values for comparison.

As Ge (or Si) atoms located at the surface of the substrate are in contact with HF,

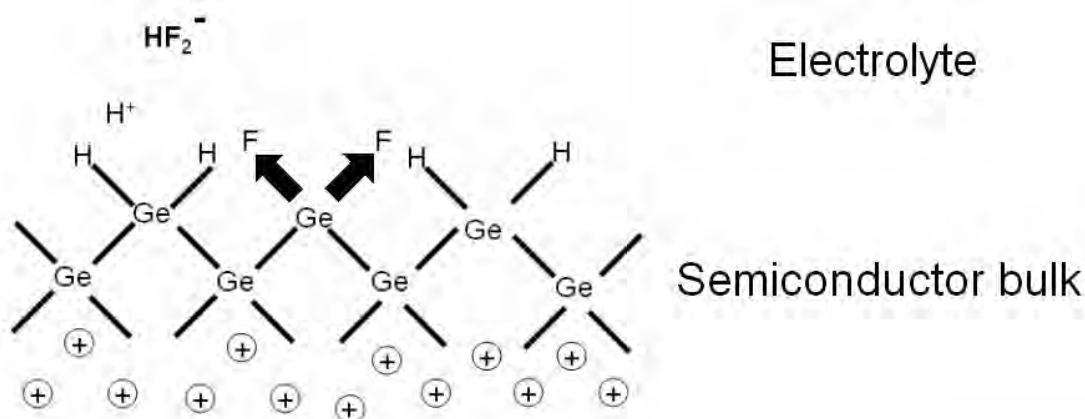


Figure 6.6: Ge substrate surface gets attacked with F-ions. The fluorine ions replace the hydrogen passivation and, due to the difference in electronegativity, weaken the Ge-Ge back-bonds.

the surface becomes H-passivated [77]-[79]. However, with increasing etching current density, F^- ions or HF_2^- ions attack the Ge-H bonds, replacing the H atoms. Thus, as a consequence of this attack, the surface bonds of the Ge atom become F passivated as shown schematically in Figure 6.6. Due to high electronegativity difference between Ge and F, the Ge atom is pulled out from the bulk and Ge-Ge back-bonds weaken. It is hence easy for other F^- or HF_2^- ions to attack the theoretically more stable back-bonds and to release an atom from the surface.

Mesoporous formation does not take place in Ge for HF electrolyte concentrations below 30 wt. %. This effect is probably related to the amount of F^- ions able to get to the substrate-electrolyte interface. Low etching current densities show oxide formation and, according to the dissolution model, the tetravalent dissolution mechanism dominates. The chemical dissolution of Ge oxides is limited for electrolyte concentrations below 30 wt. %, as the solubility is limited both by the electrolyte concentration and by the applied etching current. F or HF_2^- ions are thus consumed in the chemical etching process of Ge oxides and not in producing mesoporous layers. Therefore, strong electropolishing effects appear and mesoporous layers do not form. Higher etching current densities just strengthen this effect and strong electropolishing is observed. Ge mesoporous formation can hence only take place in highly concentrated HF solutions over 30 wt. %.

On the contrary, if the electrolytes applied are HCl or H_2SO_4 , the electronegativity difference is not large enough to pull out the Ge atoms and to weaken the back-bonds. As a consequence, Ge atoms cannot be etched, the surface becomes Cl- or S-passivated, and the substrate does not become porous. Choi and Buriak produced porous Ge layers by using HCl-based electrolytes with a concentration of 70 wt. % and by applying alternating bias with very high etching current densities about 300 mA/cm^2 [4]. Under such extreme etching conditions, other effects might play an important role and it is therefore possible to produce PGe layers. The morphology of the layers was not described in the study.

6.8 Summary and conclusions to Chapter 6

Based in experimental observations, a new model for anodic dissolution of Ge and mesoporous formation in highly concentrated HF electrolytes has been proposed. The model, as in the case of Si, takes into account the divalent and tetravalent dissolution mechanisms. Additionally, it accounts for the formation and chemical and electrochemical dissolution of Ge oxides in water or HF. In contrast to Si, the tetravalent dissolution mechanism dominates for low etching current density values. For higher etching current densities, the divalent dissolution mechanism tends to dominate. Using Faraday's law of electrolysis, an overall valence number between 4 and 3 is calculated for current densities varying between 0.1 and 80 mA/cm² respectively. The shape of the I-V curve also supports the assumptions regarding the valence presented in the model.

The critical etching current density is alternatively determined by using the dissolution rates of the already formed porous layer. A value of 7.5 mA/cm² is experimentally found. The differences in the band bending and the width of the SCR of Ge and Si suggest that the leakage current is responsible for constant electropolishing during Ge etching. The sole formation of mesoporous Ge in highly concentrated HF is explained based on electronegativity considerations of the involved atoms. Due to the high electronegativity difference between F and H atoms, Ge back-bonds become weakened, allowing thus Ge dissolution and mesoporous formation. On the contrary, HCl or H₂SO₄ based electrolytes cannot produce mesoporous Ge layers because the electronegativity difference between Ge and chlorine or sulphur is not large enough to weaken Ge substrate atoms.

Chapter 7

Annealing of porous Ge

Annealing induces a thermal reorganization of the porous layers, which is a key step in the PSI process. It determines whether the lift-off and epitaxy are possible. This chapter presents the results of annealing of porous Ge layers. The dependence of the reorganization on the porosity and the annealing atmosphere is investigated. AFM measurements and μ -Raman spectroscopy serve for layer characterization after annealing. MOCVD epitaxy of III-V compounds on reorganized Ge layers is demonstrated.

7.1 Introduction to Ge annealing

A thermally induced change in the porous structure occurs while annealing a porous layer at sufficient temperature. Annealing is always carried out at a temperature below the melting point of the substrate. Atoms become thermally activated at high temperatures and they are hence able to migrate and reorganize. The annealing process produces an enlargement of the internal pore surface and the porous layers reorganize depending on the porosity of the porous layer. Porous layers with high porosity collapse during annealing whereas porous layers with low porosity form a compacted and reinforced surface. These properties are well known and of interest for the metallurgical and ceramic industry. However, annealing processes and thermal-induced changes in porous semiconductors have not yet been intensively studied.

Different authors have studied the annealing and reorganization of porous Si under different conditions [83]-[85]. Müller *et al.* proposed a model based on experimental observations and Montecarlo simulations which describes the annealing and reorganization of single or double porous Si layers with different porosities and etching temperatures [53],[54]. The annealing of PSi always takes place at a temperature below the melting point, commonly in a range between 800 °C and 1100 °C. The atoms become thermally activated at temperatures in this range and they are able to migrate and reorganize. However, if Si oxide is present at the substrate, the surface mobility of the atoms becomes limited, thus hindering a complete reorganization of the porous layers [83]. Since the H-passivation of Si only lasts a few hours, Si oxide forms rapidly at the porous walls, as the sample is in contact with the atmosphere. The annealing process must be therefore carried out in oxygen-free atmospheres (hydrogen or argon) in order to avoid Si oxide formation.

Concerning Ge, only a few papers regarding annealing of chemically etched porous

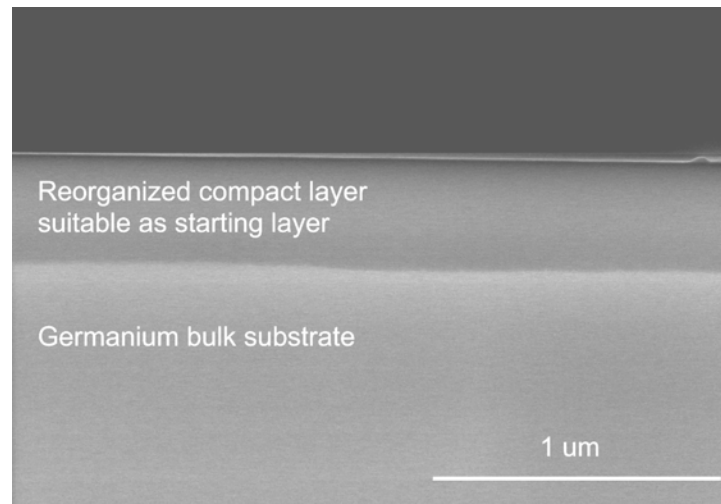


Figure 7.1: Porous layer reorganized and compacted after 30 min annealing process in hydrogen atmosphere at 575 °C. Porosity of the layer prior to annealing: 26 %.

Ge in various atmospheres were published. Annealing processes were used for crystalline enhancement, passivation of dangling bonds, or oxidation removal at the surface. PGe layers were annealed in N₂ atmosphere by studying the behavior of chemically etched Ge nanocrystals (NCs) [86]. No details concerning structure or reorganization were presented. Annealing of porous stain etched Ge in H₂ or in air at 600 °C for 30 min was used for strain removal, crystalline improvement, oxidation removal, and dangling bond passivation. However, no reorganization was presented [87],[88]. By investigating the structural composition of chemically etched Ge, an annealing step at 600 °C in H₂ atmosphere during 30 min served for passivation of dangling bonds and removing stress at the interface to the porous substrate [89],[90]. The authors concluded that an annealing step at such temperature cannot give rise to any structural change in pores like collapse, pore size changes, and NCs formation.

7.2 Annealing in hydrogen atmosphere

Reorganization of porous layers has to be carried out in a oxygen-free atmosphere. Oxides penetrate into the pores, hence reducing the mobility of the atoms and avoiding reorganization in silicon [83]. Porous samples become quickly oxidized as they are exposed to air. If annealing is carried out in a reducing atmosphere like hydrogen, native oxides are removed. The advantage of a reducing atmosphere is that hydrogen reduces Si oxides formed at the surface and enables porous layer reorganization even after oxidation.

Hydrogen samples serve for PGe layer annealing with varying porosities with a porosity step of 2 % in the range of 25 % to 65 %. Annealing of PGe layers with porosity values less than 30 % prior to annealing yields a compact closed layer. Figure 7.1 shows a reorganized and compacted mesoporous Ge layer with a thickness of about 400 nm. The PGe layer had a porosity of 26 % prior to annealing and a thickness of about 510 nm. The sample has a specific resistivity of 23 mΩcm, the applied etching

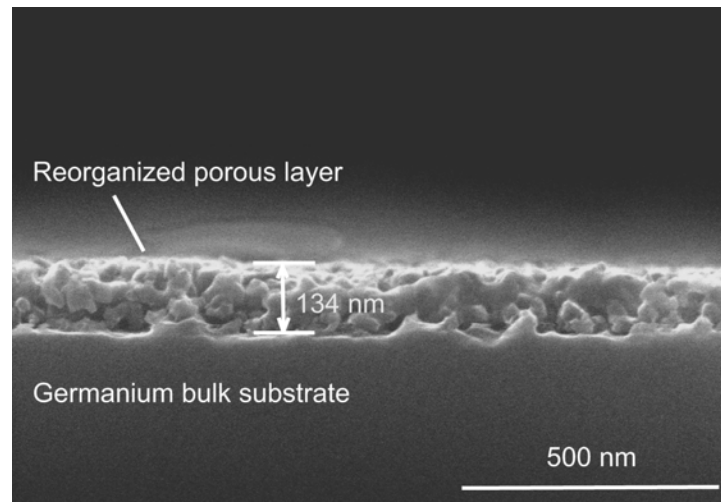


Figure 7.2: Non-uniformly reorganized PGe layer after 1 h annealing process in hydrogen atmosphere at 550 °C. Porosity of the layer prior to annealing: 44 %.

current density is 1 mA/cm² and the electrolyte is HF 50 wt. %. The reorganized layer has a porosity of 0 %. Careful inspection with high resolution SEM does not show any pore within the compacted layer.

Layers with porosities less than 30 % are of interest for their use as starting layers in the PSI process. Reorganized PGe is stable for further processing. EDX analysis corroborates that no oxygen traces are observable due to hydrogen annealing. It is possible to reorganize very thin porous layers with a thickness of less than 50 nm and obtain compacted layers. This effect comes out as a consequence of the smaller mean diameter of the Ge mesopores in comparison to those of Si. The mean diameter of mesopores in Ge lies in a range of 10 nm to 20 nm as shown in section 5.2 and 5.3. The small size of the pores is caused by the use of highly concentrated electrolytes.

Annealing of PGe layers with porosities in the 30 % to 50 % range yields a non-uniformly reorganized porous layer as shown in Figure 7.2. The sample has a specific resistivity of 13 mΩcm, the applied etching current density is 5 mA/cm², and the electrolyte is HF 50 wt. %. The thickness of the PGe layer was 180 nm prior to annealing and 134 nm after annealing. These PGe layers cannot serve neither as starting nor as separation layers.

Porous Ge layers with porosities exceeding 50 % prior to annealing completely collapse during the annealing process. The PGe layer reorganizes during annealing, yielding a surface with increased roughness. No compacted or reorganized porous layer is observable. Layers with porosities exceeding 50 % are hence of interest for their use as separation layers. Figure 7.3 shows a collapsed PGe layer with a porosity of 63 % and a thickness of 175 nm prior to annealing. The sample has a specific resistivity of 18 mΩcm, the applied etching current density is 15 mA/cm², and the electrolyte is HF 40 wt. %.

The annealing duration does not affect the annealing experiments. Reorganization occurs in the first 15 min of the annealing. Longer experiments do not show any qualitative improvement in the reorganization. Temperatures for substrate annealing are below the melting point. Structural changes and porous reorganization are ob-

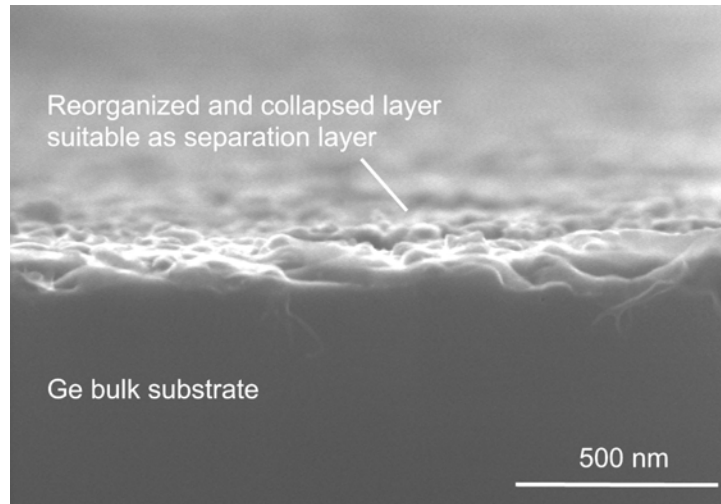


Figure 7.3: Collapsed PGe layer after 30 min annealing in H_2 atmosphere at $550^\circ C$. Porosity of the layer prior to annealing: 63 %.

servable for annealing temperatures exceeding $400^\circ C$. Temperatures in the 400 - $500^\circ C$ range do not drive to complete substrate reorganization, yielding a partially reorganized layer. Temperatures exceeding $500^\circ C$ are necessary in order to obtain the necessary reorganization of mesoporous Ge layers. Temperatures higher than $600^\circ C$ allow reorganization, but it is not homogeneously distributed in the sample. It can be stated that the optimum temperature for PGe reorganization lies in the $500^\circ C$ to $600^\circ C$ range. This contradicts the statement from Lomov *et al.* that concluded that temperatures of $600^\circ C$ were insufficient for structural changes in PGe [89].

7.3 Annealing in other atmospheres

7.3.1 Annealing in argon atmosphere

Argon atmosphere is used for porous Si annealing and reorganization. Argon is a noble gas, inert, and hence does not reduce oxides. Therefore it is necessary to perform an oxide removal step prior to annealing. The advantage of argon atmosphere is that the explosion hazard of the H_2 -atmospheres is not present. Argon is also less expensive than hydrogen.

Similarly to Ge hydrogen annealing, PGe layer annealing in argon atmosphere shows layer reorganization for temperatures exceeding $400^\circ C$, although temperatures exceeding $500^\circ C$ are necessary for complete reorganization. Temperatures exceeding $600^\circ C$ show inhomogeneous reorganization. The optimum temperature for sample annealing also lies in the 500 - $600^\circ C$ range.

Contrary to hydrogen annealing, native oxides are present at the surface of the sample after annealing in argon atmosphere, as confirmed with EDX and FTIR. Large rounded oxide accumulations appear at the surface of the reorganized PGe layer as shown in Figure 7.4. The sample has a specific resistivity of $25\text{ m}\Omega\text{cm}$, the applied etching current density is 1 mA/cm^2 , and the electrolyte is HF 50 wt. %. The PGe

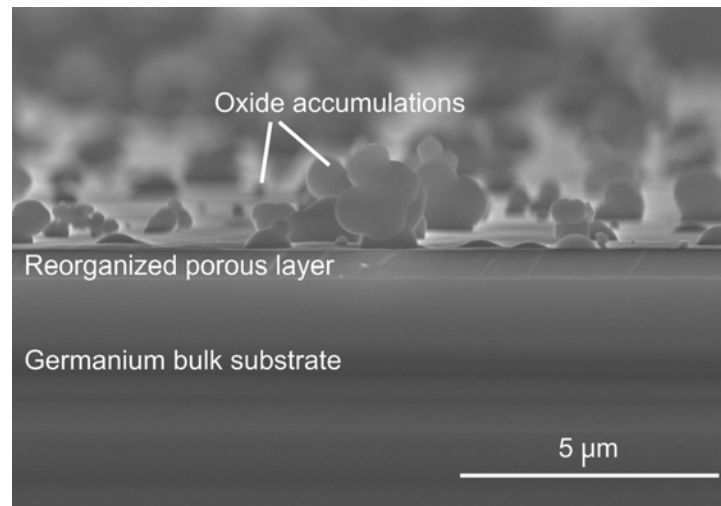


Figure 7.4: Reorganized and closed PGe layer after 15 min argon atmosphere annealing at 575 °C. Porosity of the layer prior to annealing: 28 %. Note the oxide accumulations caused by insoluble Ge oxides during annealing.

layer had a porosity of 28 % prior to annealing and a thickness of 750 nm. After annealing, the reorganized PGe layer has a porosity of nearly 0 % and a thickness of 595 nm.

The HF dip prior to annealing removes water soluble Ge oxides, but cannot remove the Ge oxide insoluble phases, which present a limited solubility in HF as shown in Section 6.2 and in Reference [77]. GeO insoluble phases evolve to water-soluble Ge oxides during subsequent annealing, causing thus the reorganized PGe layer to become water soluble and hence unstable for further processing. Various pre-treatments for oxide removal prior to the tempering process damaged the PGe layer and did not remove Ge insoluble oxides. Contrary to the silicon case, Ge oxides do not hinder reorganization.

7.3.2 Annealing in forming gas atmosphere

Forming gas is a mixture of up to 5 % hydrogen in nitrogen. Forming gas is commonly used for processes that require the presence of hydrogen but without explosion hazard. Other advantage is that it is not as expensive as hydrogen or argon gas. The optimum temperature lies in the 500-600 °C range, similarly to annealing experiments in hydrogen or argon atmospheres. Annealing temperatures between 400 °C and 500 °C yield a partially reorganized porous layer. The PGe layer presents colors on its top, characteristic of porous layers that have not been reorganized completely [79]. Temperatures exceeding 600 °C drive to an inhomogeneous layer reorganization.

Samples annealed in forming gas show oxide content as measured with EDX. Oxidized porous layers are unstable in water or HF dips. The amount of hydrogen in forming gas is not sufficient to reduce completely water insoluble oxides formed during electrochemical etching. Consequently, the PGe layer remains oxidized after annealing. Variations in the annealing time, temperature, and gas flow do not lead to complete removal of PGe.

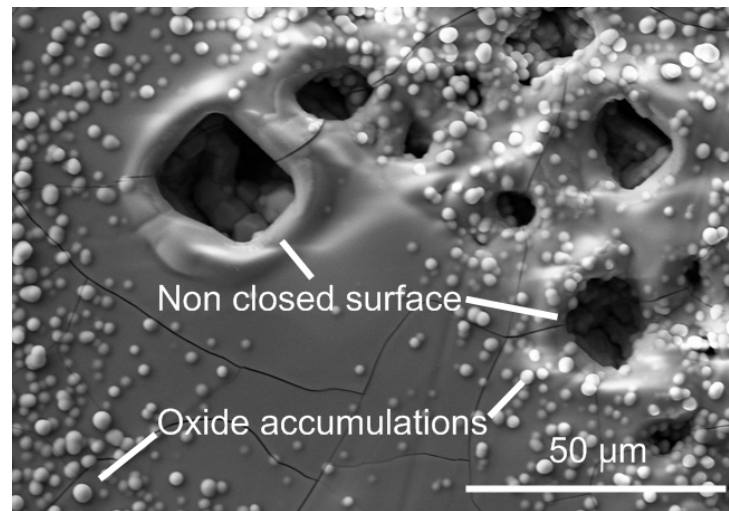


Figure 7.5: Plane view of a reorganized porous layer in forming gas 45 min at 650 °C. Note that the round-shaped accumulations are Ge water-soluble oxides.

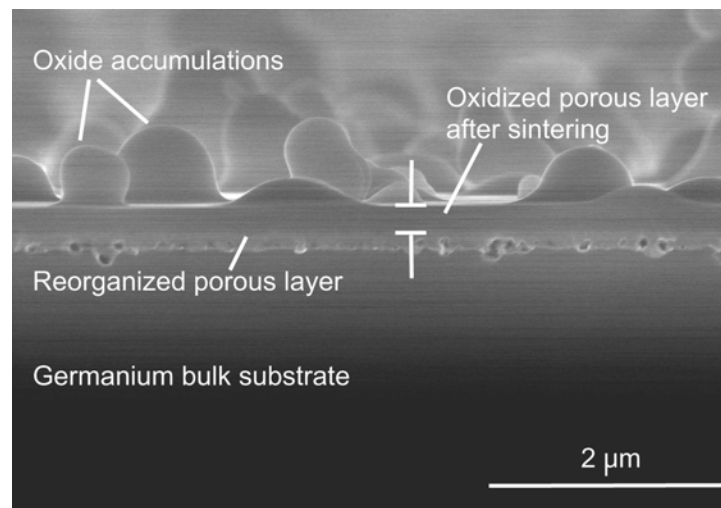


Figure 7.6: Cross section view of a PGe layer annealed in nitrogen atmosphere. Round-shaped oxide accumulations can be observed at the top of the reorganized layer. The darker region at the top of the layer has become oxidized. Note that the nitrogen flow is set to 5 L/min and the annealing duration to 45 min at 680 °C.

Figure 7.5 shows a plane view of a reorganized porous layer in forming gas. Large Ge rounded oxide accumulations cover the surface, proving thus that the forming gas does not remove the oxide. Large craters containing oxides form at the surface due to the non-optimized temperature and annealing time [79].

7.3.3 Annealing in nitrogen atmosphere

The results obtained under nitrogen atmosphere do not substantially differ from those obtained under forming gas atmosphere. All samples annealed in nitrogen atmospheres are still oxidized after annealing. Oxidized PGe layers cannot withstand water rinse or HF dip and they are therefore unstable. Any variation in the annealing time, temperature, and gas flow does not avoid PGe oxidation.

Figure 7.6 shows a PGe layer annealed in nitrogen atmosphere. Large rounded oxide accumulations appear at the surface of the layer. A darker region additionally appears at the upper part of the reorganized PGe layer. The dark region corresponds to an oxidized region. The oxide diffuses from pore walls during reorganization and moves to the upper part of the reorganized layer. Annealing and reorganization yield a PGe layer with two well defined regions: An oxidized and darker region at the upper part of PGe, and a non oxidized and reorganized region at the bottom of the PGe. A subsequent water or HF-dip removes the oxidized region and leaves the bottom part unaffected, as the oxide is only located at the top of the layer and is water soluble.

7.4 Lift-off of single porous layers

Section 5.2.3 shows that the porosity of PGe layers might vary throughout the layer. Long electrochemical etching experiments with low etching current densities cause the formation of PGe layers with large cavities as shown in Figure 5.13. Figure 7.7 shows the cross section of a reorganized PGe layer with varying porosity throughout the layer. The porous layer is etched 15 hours in HF 50 wt. % with an etching current density of 1 mA/cm². The substrate resistivity is 20 mΩcm. H₂-atmosphere serves for annealing 30 min at 575 °C.

Annealing of such layers causes the upper part of the porous layer to become closed and compacted. Figure 7.7.a shows a SEM cross section caption of a reorganized PGe layer. The lower part of the layer automatically detaches from the substrate due to increased porosity at the bottom of the porous layer and the presence of large cavities. Layer transfer is hence possible by adhering a sticky pad to the PGe layer as shown in Figure 7.7.b. EDX analysis confirms the presence of transferred PGe layer to the sticy pad. Figure 7.7.c shows the back side of the sticky pad and Figure 7.7.c shows the tracks of previous layer transfer experiments.

7.5 Surface characterization

Surface roughness is an important parameter for a subsequent epitaxy of III-V compounds. AFM analysis serves for surface characterization and roughness measurements. Figure 7.8 shows AFM 3-D scan micrographs with a size of 2x2 μm for each step of the

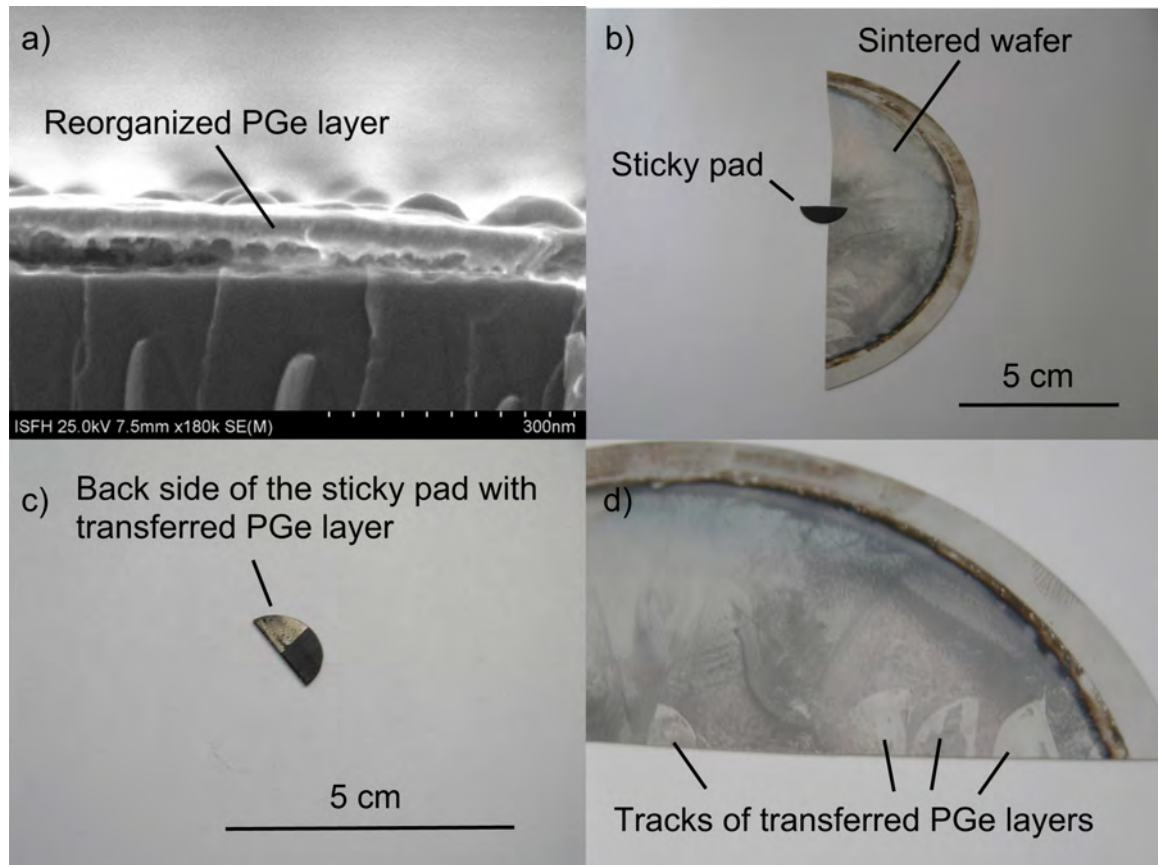


Figure 7.7: Figure a) shows a SEM caption of the reorganized PGe layer after annealing. The reorganized layer detaches from the substrate automatically. Figure b) shows a sticky pad adhered to a sintered wafer. In Figure c), the back side of the sticky pad shows the transferred PGe layer. Finally, Figure d) shows the marks of previous layer transfer experiments.

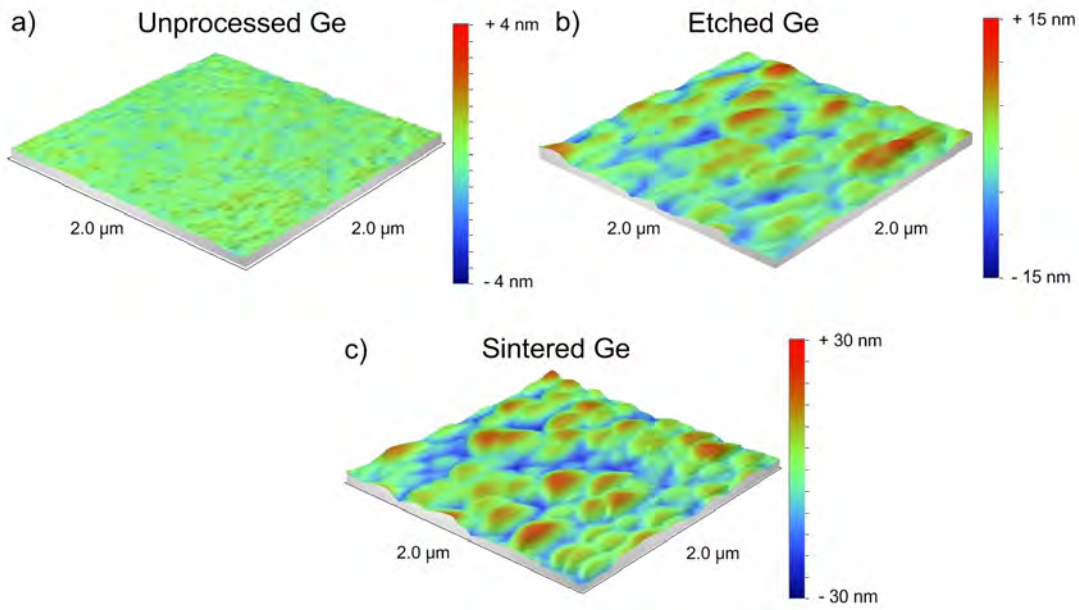


Figure 7.8: AFM 3-D scan micrographs of the surface of a) Ge blank wafer, b) Etched PGe wafer, and c) Reorganized PGe wafer in hydrogen atmosphere. Note that each measurement has a different height scale.

PSI process, i.e. Ge bulk substrates, as-etched substrates, and reorganized and closed PGe layers in hydrogen atmospheres. Figure 7.8.a shows the surface of unprocessed Ge. The maximum peak-valley height difference, i.e. the height difference between the highest and the deepest point of the surface, is 2.13 ± 0.1 nm. The average surface roughness is 0.31 ± 0.1 nm. Figure 7.8.b shows a mapping of the surface of a Ge wafer after electrochemical etching. The maximum height difference is 21.66 ± 0.1 nm and the mean surface roughness is 3.52 ± 0.1 nm. Figure 7.8.c shows the surface of PGe after etching and annealing in hydrogen atmosphere 15 min at 600 °C. The maximum height difference is 44.94 ± 0.1 nm and the average surface roughness is 7.85 ± 0.1 nm.

Figure 7.8.a shows an unprocessed Ge wafer that has a flat surface. This substrate roughness allows high quality epitaxial growth of III-V compounds. Figure 7.8.b shows the surface of an etched PGe wafer. The increased surface roughness is caused by strong electropolishing of the already formed porous layer. Substrate reorganization in hydrogen atmosphere yields a compacted layer with higher substrate roughness as in the etched state. This substrate roughness allows epitaxy but is not sufficient for high quality epitaxial growth. The surface roughness increases substantially after etching and after annealing in comparison to GaAs and Si as shown in Appendices A and B respectively.

μ -Raman confocal spectroscopy serves for structural analysis of PGe layers. Figure 7.9 shows a μ -Raman shift analysis of a PGe layer. The black line refers to a blank reference wafer without PGe layer. The dotted red line refers to a PGe etched layer and the green dashed line refers to a sintered and reorganized PGe layer. Independently of the intensity, no Raman shift is observable and all three peaks lie at the same value of 300 cm^{-1} , which is the characteristic Ge l-peak and has been already observed in

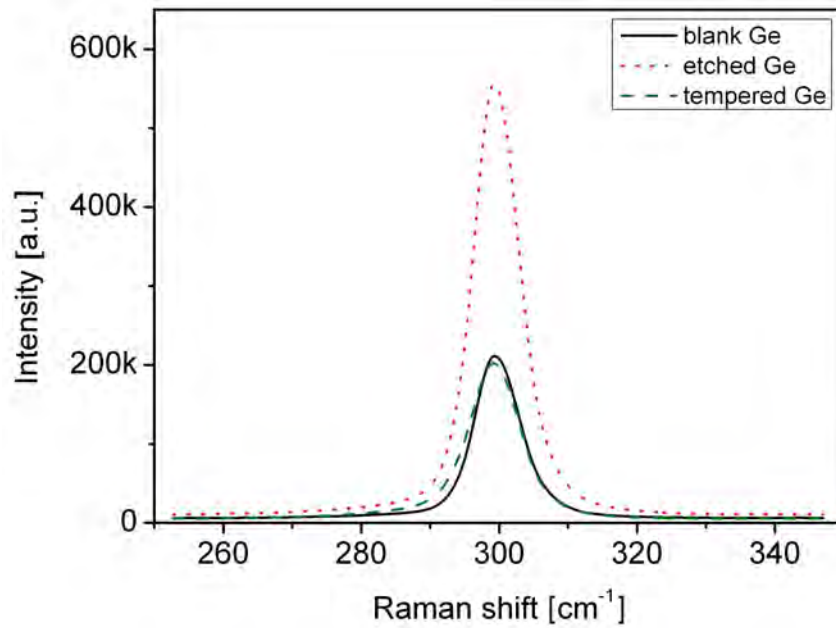


Figure 7.9: Detailed μ -Raman shift analysis of mesoporous Ge. No shift is observable and all three peaks lie at 300 cm^{-1} .

the literature for Ge bulk substrates [91]. This measurement confirms that etching and annealing of PGe do not affect the crystalline structure of the substrate and remains monocrystalline after reorganization.

7.6 MOCVD epitaxial growth of III-V compounds on reorganized PGe

MOCVD epitaxial growth of III-V compounds is carried out at the research group "III-V - Epitaxy and Solar Cells" lead by Dr. Frank Dimroth of the Fraunhofer Institute for Solar Energy Systems in Freiburg. Three GaInAs/GaInP stacks were grown on top of reorganized PGe layers at $600\text{ }^\circ\text{C}$ in hydrogen atmosphere for 1 hour. The porous layers are etched 3 hours in HF 50 wt. % at 1 mA/cm^2 . The PGe layer has a thickness of $90 \pm 5\text{ nm}$ and a porosity of $27 \pm 5\%$ prior to annealing. The thickness of each III-V compound layer is 300 nm. Two stacks are additionally grown on top of reference Ge wafers.

Figures 7.10.a and 7.10.b show the cross section of GaInAs/GaInP stacks grown on top of reorganized PGe layers. Each single layer is identifiable due to their different colour. The substrate roughness of the PGe layer prior to epitaxial growth propagates throughout the stack, causing irregular layer growth and void formation. Figure 7.10.c and 7.10.d show a detailed inspection of the layer structure. Enhanced substrate surface roughness prevents high quality epitaxial growth. Figure 7.10.d shows that the layers present a microcrystalline structure. Irregular PGe surface and defects diminish the quality of the III-V stack. Growth of III-V compounds on top of PGe layers is hence possible. However, the quality of the layers is not sufficient for highly efficient

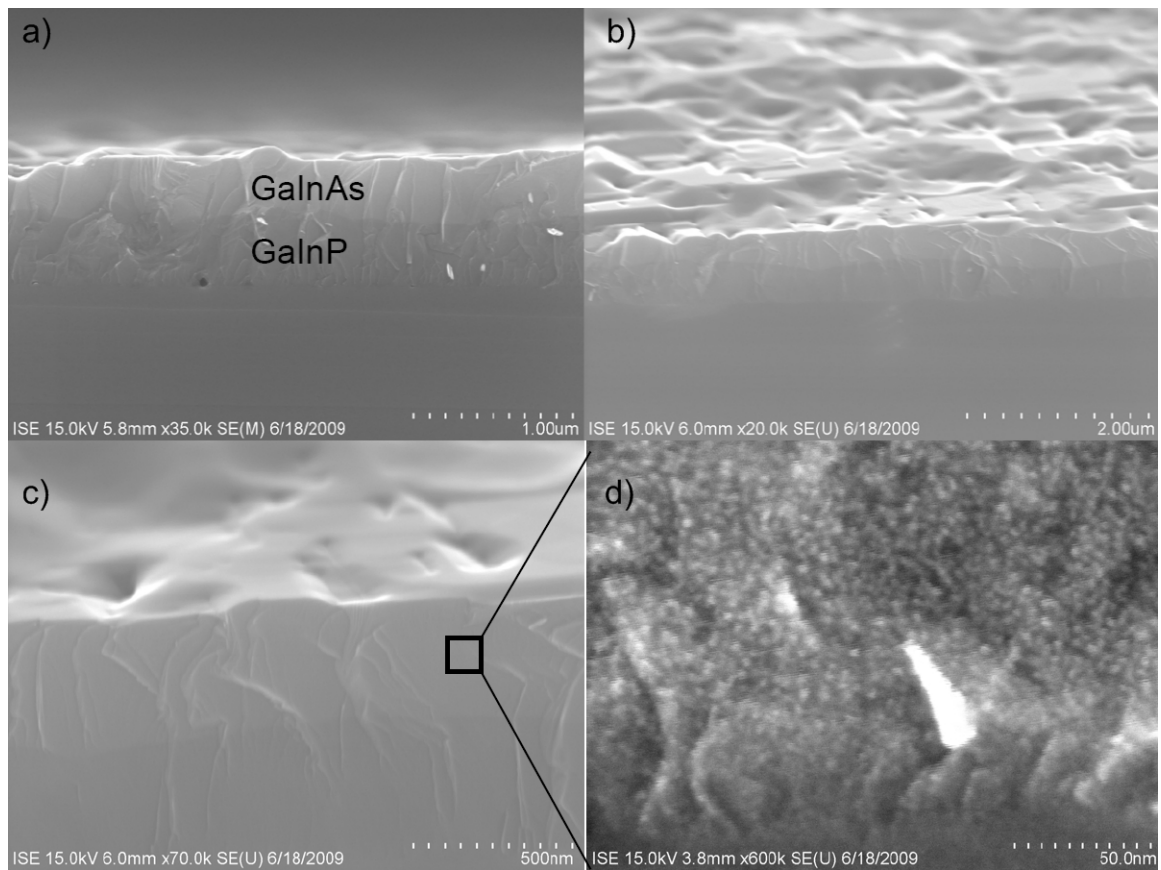


Figure 7.10: SEM cross section images of epitaxially grown GaInAs/GaInP stacks. Figures 7.10.a and 7.10.b show the III-V stack and Figure 7.10.c and 7.10.d show a microcrystalline structure. Figure from FhG-ISE in Freiburg.

multijunction space solar cells.

7.7 Outlook and conclusions to Chapter 7

Mesoporous Ge annealing in hydrogen atmospheres yields always a reorganized and non-oxidized PGe layer, which depending on the porosity, either compacts, gets closed ($P < 30\%$), and serves as starting layer, or collapses ($P > 50\%$) and serves as separation layer. Annealing in hydrogen atmosphere is compulsory in order to obtain a stable layer for further processing. Hydrogen reduces Ge oxides and avoids oxidation during annealing. The optimum reorganization temperature lies in the 550 °C to 600 °C range, contrary to the statement of Lomov *et al.*, who stated that 600 °C was insufficient for structural changes in PGe [89]. Structural changes are observable for temperatures as low as 300-400 °C.

Annealing in forming gas, nitrogen, or argon atmospheres yields an oxidized and reorganized PGe layer which dissolves in water or HF. Insoluble GeO phases formed during electrochemical etching evolve to water-soluble GeO during annealing. Ge oxides do not hinder reorganization of PGe contrary to the Si case [83]. Reorganized PGe layers in forming gas, argon, or nitrogen are unstable for further processing and therefore do not permit epitaxial growth.

Lift-off of layers with large voids and varying porosity is demonstrated. The surface roughness increases drastically after etching and annealing steps. III-V epitaxial growth is possible on top of reorganized PGe layers. The surface roughness is however not sufficient for high quality epitaxial growth. III-V stacks present very large surface roughness and microcrystalline structure derived from the PGe substrate. The quality of these layers is not sufficient for the fabrication of high-efficiency space solar cells. The initial objective of fabricating a very-thin highly-efficient space solar cell was set aside and the efforts were concentrated in obtaining other porous materials that allow high-quality epitaxial growth. Appendices A and B present the results derived from these investigations.

Chapter 8

Summary and conclusions

Multidisciplinary applications of porous Ge motivate this thesis. Porous Ge is of interest for optoelectronics, fuel cells, biomedical applications, and hydrogen purification. The porous silicon process allows, based on temperature-induced morphology changes of a mesoporous double layer, the separation of very-thin semiconductor films. Layer transfer processes based on porous materials similarly to the PSI process are interesting for the fabrication of very thin highly-efficient solar cells. This thesis explored the possibility of applying a layer transfer process for space solar cells based on mesoporous germanium, which might help to reduce the weight of the solar array and increment the available payload of the satellite.

Previous studies did not succeed to produce mesoporous Ge by electrochemical etching. Therefore, the thesis focussed first on PGe layer formation and morphology characterization. For the first time in the literature, uniform 4 inch mesoporous Ge layers formed by electrochemical etching of highly-doped Ge substrates in highly concentrated HF-based electrolytes with a concentration of 30-50 wt. %. The porosity strongly determines substrate reorganization and typically varied in a range of 25 % to 70 % as measured by gravimetric measurements. Layers with porosities exceeding 40 % serve as separation layer and are easily achievable, whereas layers with porosities below 30 % are interesting as starting layer and however, difficult to achieve. Low porosities require the combination of all three important etching parameters: Low etching current densities, high electrolyte concentrations, and substrate specific resistivities in the 17-30 m Ω cm range.

Porous Ge formation presents substantial differences to porous Si or GaAs formation. PGe formation was always accompanied by strong electropolishing effects, which caused the already-formed porous layer to dissolve. The usage, i.e. material/porous transforming efficiency, increased from 0.2 % to 98 % by periodically alternating the etching bias from anodic to cathodic, hence avoiding electropolishing and allowing a porous layer formation similar to Si. Alternating bias additionally allowed the formation of double- and multi-layers with varying thickness and porosity. Electrochemical etching with other electrolytes did not show mesoporous layer formation in any concentration. Otherwise, macropores and etch pits formed with varying size and orientation.

Based on experimental observations, this work presented a model describing Ge anodic dissolution and porous etching in highly concentrated HF electrolytes. Germanium's anodic dissolution differs from silicon's. Contrary to Si, the tetravalent is the

main dissolution mechanism for low etching currents in Ge. The divalent dissolution dominates for high etching current densities. This influences the etching velocity and causes low etching rates. The critical etching current density was determined using the etching rates. Faraday's law of electrolysis served for determining the dissolution valence number. Band bending simulation of Si- and Ge/electrolyte interfaces suggested that a flatter band bending in the Ge case was responsible of electropolishing, effect that was already observed by other authors.

Annealing of mesoporous Ge layers was investigated and various atmospheres and temperatures served for PGe reorganization. Hydrogen atmospheres yielded stable and reorganized porous layers, whose structural morphology varied depending on their porosity. On the contrary, samples annealed in nitrogen, forming gas, or argon always yielded an oxidized porous layer, hence water-soluble and unstable for further processing. Ge annealing and reorganization must be carried out in hydrogen atmosphere in order to ensure stable further processing. AFM served for surface characterization and showed an increased surface roughness after etching and annealing. Epitaxial growth of III-V compounds on top of reorganized and stable porous Ge layers was possible but showed high surface roughness, low quality, and microcrystalline structure. The growth of space solar cells on reorganized PGe layers requires more efforts.

Finally, Appendices A and B present alternatives to mesoporous Ge for layer transfer processes applicable to space solar cells that were investigated during this thesis. Appendix A presents the first time demonstration in the literature of mesoporous p-type GaAs single- and double layer formation. The demonstration for the first time in the literature of mesoporous Ge and GaAs formation by electrochemical etching in highly doped p-type substrates represents a significant advance to the previous porous materials knowledge. Inverted $\{111\}$ pyramids form at the porous layer/substrate interface by applying low etching current densities. High etching current densities avoids pyramid formation. The reduced substrate roughness of PGaAs in comparison to PGe suggests that high-quality epitaxial growth of III-V compounds is possible. Appendix B deals with mesoporous formation on PSi (100) substrates with a 6° miscut orientation towards (111). EBSD measurements indicate that the substrate orientation remains constant after etching and annealing. μ -Raman analysis do not show any peak shift, that indicates that the crystalline structure remains unaffected. AFM measurements demonstrate that the substrate roughness after etching and annealing is comparable to the bulk substrate, hence suggesting that high quality epitaxial growth of III-V compounds is possible. Both porous materials are interesting and open a new field of investigation.

Appendix A

Mesoporous GaAs

Other potential alternatives for layer transfer based on porous materials have been additionally studied simultaneously to the investigation regarding mesoporous Ge formation. The formation of porous GaAs has been extensively studied [92]-[99], specially focused in n-type substrates. The investigation has been mainly focused on optical properties for photonic crystals and photoluminescence emission of nanocrystals, but not on applying lift-off processes. Porous GaAs can be obtained by means of electrochemical etching in H_2SO_4 [100],[101], HCl [93],[92], and in HF [94]-[99]. This appendix presents for the first time in the literature a demonstration of mesoporous GaAs formation in highly doped p-type substrates. Mesoporous single- and double layers are obtained by means of electrochemical etching in highly concentrated HF-based electrolytes.

A.1 Experimental

The GaAs wafers used in this investigation are monocrystalline, 4 inch in diameter, and polished on both sides. The substrates have a thickness of (650 ± 50) μm . The substrate orientation is (100) and the specific resistivity is in a range of 1 $m\Omega cm$ to 5 $m\Omega cm$. A double container etching cell is used for anodizing the wafers. Aqueous hydrofluoric acid with a concentration varying in a range of 30 % to 50 % in weight serves as electrolyte. The potentiostat Elypor 3 (ET&TE Etch & Technology GmbH) allows various current or voltage time-profiles in either galvanostatic or potentiostatic mode. After etching, the samples are rinsed in deionized water and dried under N_2 stream. The morphology and thicknesses of the porous layers are inspected with a SEM and the surface roughness is investigated using an AFM.

The porosity is calculated by means of gravimetric measurements. The wafers are weighed before (m_1) and after (m_2) etching in order to determine the amount of gallium arsenide that has been removed during porous formation. Afterwards, the wafers are introduced for 10 sec in a $H_2O:H_2O_2:H_3PO_4$ (140:2.5:1) or a diluted CP_4 solution in order to remove the porous layer selectively. The remaining mass of the substrate is obtained by weighing the sample again (m_3). The porosity is thus determined as shown in Equation A.1.

$$P = \frac{m_1 - m_2}{m_1 - m_3} \quad (A.1)$$

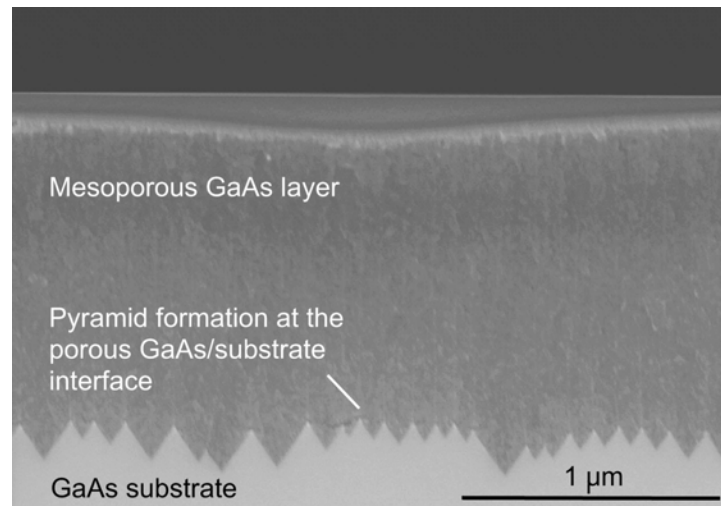


Figure A.1: Porous layer with a thickness of about 1.3 μm with well-defined $\langle 111 \rangle$ pyramids present at the porous layer/substrate interface. Etched 50 min at 1 mA/cm^2 in HF 45 wt. %. Etching rate of 24.9 nm/sec .

A.2 Mesoporous single- and double layer formation

Porous GaAs layers are obtained by anodization with different current densities. Randomly and uniformly distributed mesopores form at the surface of the sample during etching. Figure A.1 shows a cross-sectional SEM image of a GaAs sample after etching. Figure A.1 shows a porous layer etched 50 min in HF 45 wt. % with an etching current density of 1 mA/cm^2 , yielding a porous layer thickness of 1.3 μm with a porosity of 56 % and 100 nm-sized $\langle 111 \rangle$ -oriented pyramids at the porous layer/substrate interface. $\{111\}$ faceting is anisotropic and is caused by a smaller etching rate for $\{111\}$ than for $\{100\}$ planes. This effect has not been reported either for Si [3] or for Ge [21] mesoporous layer formation in highly concentrated HF electrolytes.

Porous formation with etching current densities below 7.5 mA/cm^2 shows pyramid formation whereas etching current densities exceeding 7.5 mA/cm^2 do not show pyramid formation as shown in Figure A.2. The high etching current density dominates the etching process and overcomes the resistance of the stable $\{111\}$ planes. The porous GaAs/substrate interface flattens and the pyramids do not appear. The porous layer/substrate interface has a roughness of less than 50 nm as determined by AFM measurements after chemically removing the porous double layer.

Figure A.3 shows a mesoporous GaAs double layer. The upper layer, with a thickness of 412 nm, is obtained in aqueous HF electrolyte 45 wt. % by applying an etching current density of 5 mA/cm^2 for 5 min. The etching rate is 91.33 nm/min and the layer has a porosity of 58 %. The buried layer is subsequently etched in aqueous HF with a concentration of 35 wt. %. The etching current density is abruptly increased to 25 mA/cm^2 for 1 sec, resulting in a porous layer with a thickness of about 260 nm, a porosity of 74 % and an etching rate of 260 nm/sec . The porous starting layer is not further dissolved during this current pulse due to the passivation of the pore walls with hydrogen atoms. There are no pyramids observable at the porous layer/substrate interface. The increased etching current density required for the high porosity layer dominates

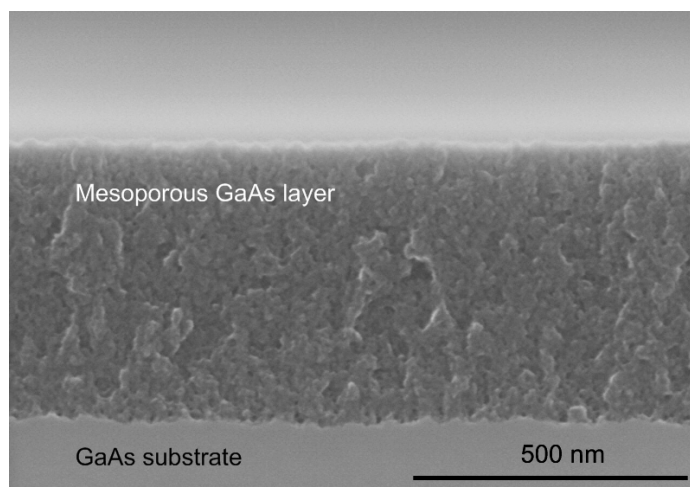


Figure A.2: Porous layer with a thickness of about 650 nm without any pyramids present at the porous layer/substrate interface. Etched 4 sec at 10 mA/cm² in HF 45 wt. %. Etching rate: 177.5 nm/sec.

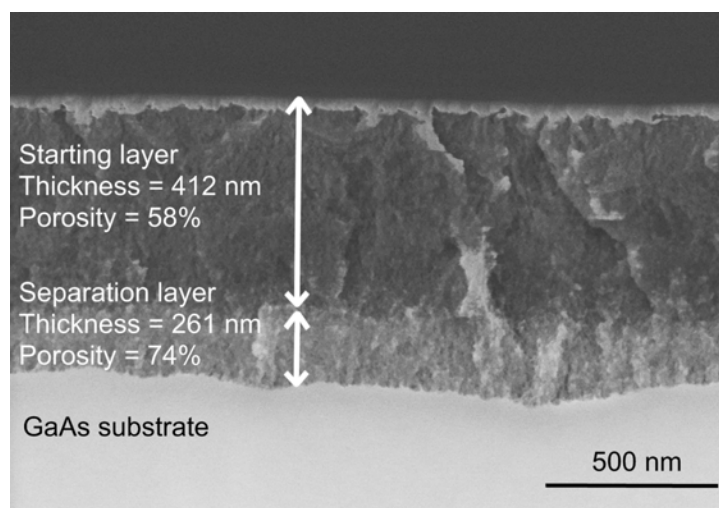


Figure A.3: Mesoporous GaAs double layer. Two well-defined porous layers with different porosities can be observed. Starting layer: 5 min at 5 mA/cm² in HF 45 wt. %; Buried layer: 10 sec at 100 mA/cm² in HF 35 wt. %.

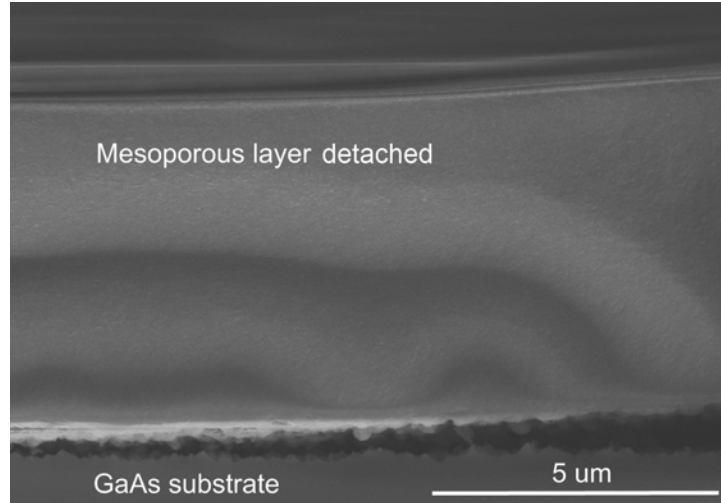


Figure A.4: Mesoporous layer detached from the substrate. Etched for 20 sec at 25 mA/cm² in HF 45 wt. %. Etching rate: 356 nm/sec.

over the influence of the crystallographic orientation. The porous layer/substrate interface has a roughness of less than 100 nm as determined by AFM measurements after chemically removing the porous double layer.

Uniform single- and double porous layers with a thickness of up to 7 μm form reproducibly. The porous layers are composed of micro- and mesopores with a diameter in the range of 1 nm to 38 nm as measured by SEM with an image recognition software. The porous layers automatically detach from the substrate when the thickness of the porous layer exceeds 7 μm , hence forming a self-standing porous layer. These porous layers cannot be thus utilized for a subsequent epitaxy and layer transfer processes. Figure A.4 shows a self-standing mesoporous layer that has been detached from the substrate.

A.3 Porous GaAs layer characterization

The porous layer etching rate is determined for varying etching current densities with a substrate specific resistivity of 1 m Ωcm and an electrolyte concentration of 45 wt. %. Figure A.5 shows that the porous GaAs etching rate lies in a range of 1.7 nm/sec to 1.7 $\cdot 10^3$ nm/sec for etching current densities of 0.1 mA/cm² to 100 mA/cm² with an electrolyte concentration of 45 wt. %. The etching rate increases linearly with increasing etching current density. Similarly to the anodization of p-type Si with the same substrate resistivity and without illumination, the etching rate increases with (i) increasing etching current density and (ii) increasing electrolyte concentration.

Figure A.6 shows the dependence of the porosity on the etching current density. Porosity values in the 55-70 % are obtained for an electrolyte concentration of 45 wt. % and a substrate resistivity of 1 m Ωcm . This effect has been already observed in Si [40] and Ge [22]. Figure A.7 shows the porosity in dependence on the electrolyte concentration for an etching current density of 1 mA/cm². Porosities lie in a range of 69 % to 53 % for etching current densities ranging from 30 wt. % to 50 wt. %. The

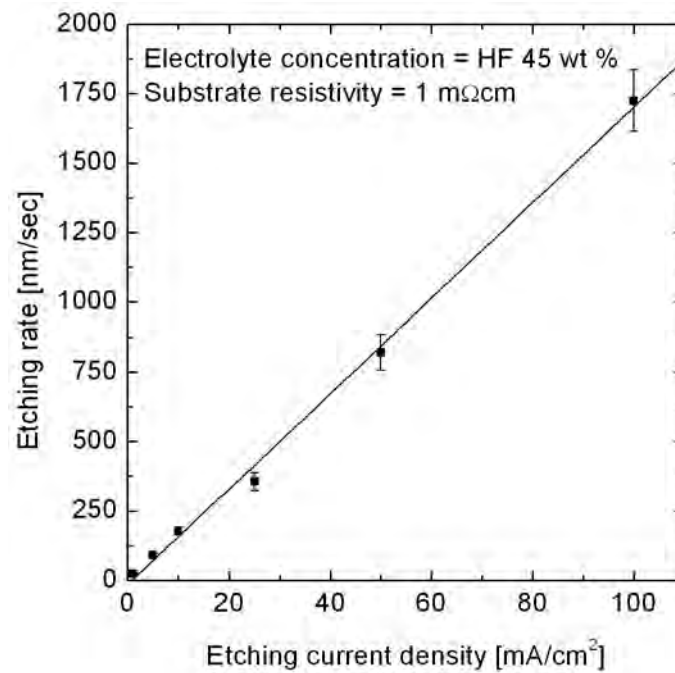


Figure A.5: Etching rate vs. etching current density for an HF electrolyte concentration of 45 wt. %. Note that the solid line is a linear fit to the experimental data.

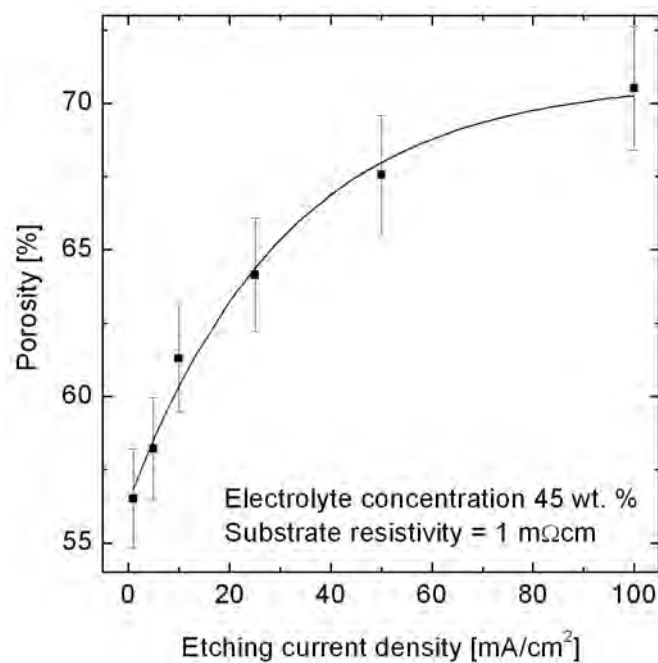


Figure A.6: Porosity vs. etching current density for an HF electrolyte concentration of 45 wt. %. Note that the solid line is a guide for the eye.

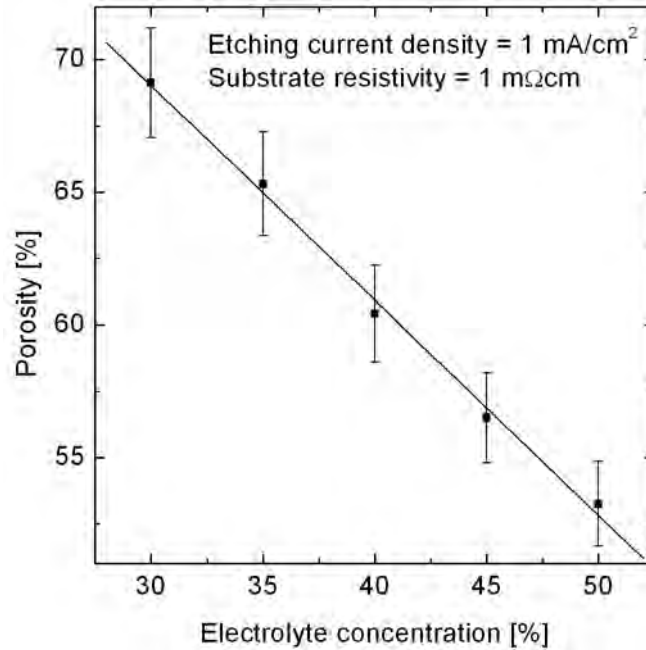


Figure A.7: Porosity vs. electrolyte concentration for an etching current density of 1 mA/cm^2 and a substrate resistivity of $1 \text{ m}\Omega\text{cm}$. The solid line is a linear fit to the experimental data.

porosity decreases nearly linearly with increasing electrolyte concentration. This effect has been already observed in Si [40] and Ge [24]. Similarly to the anodization of p-type Si with the same substrate resistivity and without illumination, the porosity increases with (i) increasing etching current density and (ii) decreasing electrolyte concentration.

Figure A.8 shows three dimensional surface AFM scans of GaAs samples with an area of $1 \mu\text{m}^2$. The mean surface roughness of the non-processed GaAs wafer is 0.15 nm with a maximum height difference of 1.21 nm . The surface roughens slightly after etching to a mean roughness value of 0.24 nm and a maximum height difference of 3.12 nm . The surface roughness values are however much lower than those of porous Ge as shown in Section 7.5.

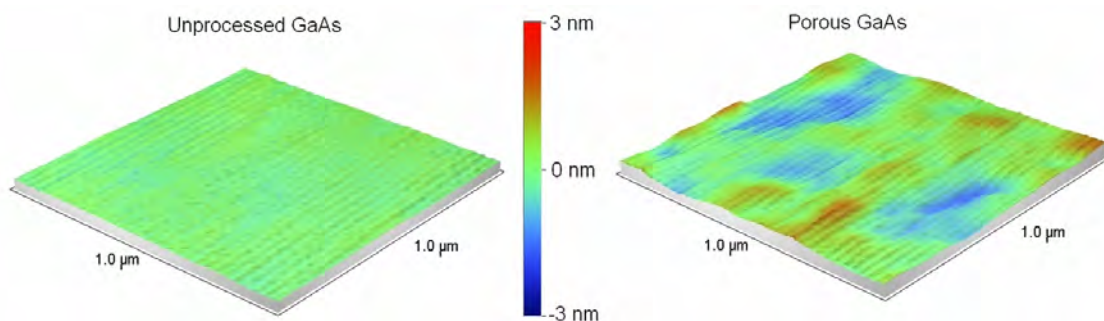


Figure A.8: Surface AFM scans of GaAs wafers with a resistivity of $1 \text{ m}\Omega\text{cm}$. At the left, unprocessed GaAs bulk wafer. At the right, porous GaAs after etching. Note that the scale varies in a range of -3 nm to $+3 \text{ nm}$.

A.4 Summary and conclusions to Appendix A

Mesoporous GaAs double layers with different porosities and thicknesses up to 7 μm are formed on highly doped p-type 4 inch GaAs substrates by means of electrochemical etching in highly concentrated HF electrolytes. Porous layers with thicknesses exceeding 7 μm automatically detach from the substrate and form self-standing porous layers. Small $\langle 111 \rangle$ oriented pyramids form at the interface between porous layer and substrate if etching current densities below 7.5 mA/cm^2 are applied. The facetting at the porous layer/substrate interface disappears by increasing the etching current density above 7.5 mA/cm^2 . Porous double layers with different porosities are obtained by varying simultaneously the etching current density and the electrolyte concentration.

The etching rate of the porous layers lies in the range of 1.7 nm/sec to $1.7 \cdot 10^3$ nm/sec for etching current densities of 0.1 mA/cm^2 to 100 mA/cm^2 with an electrolyte concentration of 45 wt. %. The porosity of the porous GaAs layers behaves similarly to porous Si or Ge. The porosity increases from 56 % to 70 % in the 1 mA/cm^2 to 100 mA/cm^2 range and decreases nearly linearly from 69 % to 53 % with electrolyte concentrations increasing from 30 wt. % to 50 wt. % respectively. The etching process increases the mean roughness of the porous layer surface from 0.15 nm to 0.24 nm , although it is very small in comparison to the roughness values of porous Ge and hence promising for the achievement of a layer transfer process. The etching rates and thicknesses achieved indicate that this technique may be compatible with standard processes in the space solar cells industry. Future investigations will show whether this porosity step is already sufficient for a layer transfer process.

Appendix B

Mesoporous Si (100) with 6° off towards (111)

This chapter deals with the preservation of the 6° off orientation towards (111) after annealing of porous Si double layers. Reproducible layer transfer of double layers and the preservation of the substrate orientation open them the possibility of applying a successful layer transfer of III-V compounds grown epitaxially on top of reorganized mesoporous Si. Wafers with 4 inch diameter are used, which is the standard substrate size in space solar cell production. The surface roughness and the crystalline orientation of the substrate are investigated by means of AFM measurements and EBSD analysis respectively. μ -Raman confocal microscopy analysis is carried out as well.

B.1 Experimental

The sample preparation for the PSI process starts with boron-doped, monocrystalline one-side polished Si wafers with 100 mm diameter. Their thickness is $(525 \pm 25) \mu\text{m}$, their orientation is (100) with a miscut of 6° off towards (111), and the specific resistivity is $(10 \pm 2) \text{m}\Omega\text{cm}$.

The double-container etching cell shown in Section 4.1 serves for anodizing the wafers. The electrolyte is a 2:1 vol solution of HF 50 wt. % in ethanol. The silicon wafer is immersed in the solution and the electrical contact is obtained due to the high dopant concentration of the substrate. The potentiostat Elypor 3 (ET&TE Etch & Technology GmbH) allows different etching profiles in either galvanostatic or potentiostatic mode with anodic or cathodic bias. The starting layer is etched for 100 sec at 5mA/cm^2 . The separation layer is etched for 3 sec at 200mA/cm^2 . After etching, the substrates are rinsed in deionized water, dried under an N_2 stream, and introduced in a H_2 furnace for sintering. The sintering of porous Si is always carried out at temperatures below the melting point, typically at $1100 \text{ }^\circ\text{C}$. The annealing step lasts 1 hour. After annealing, the starting layer is attached to a glass carrier. By applying mechanical stress to the glass carrier, the separation layer detaches from the substrate.

The morphologies and thicknesses of the porous layers are investigated in a high resolution Hitachi S-4800 SEM. The porosity is calculated by means of gravimetric measurements. A MultiMode AFM (Digital Instruments) with a Nanoscope III con-

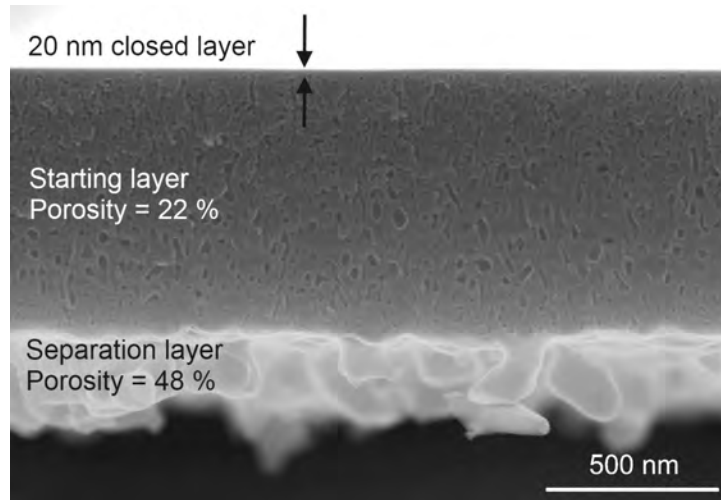


Figure B.1: Cross section SEM image of a reorganized and detached porous layer after the sintering step of 1 h in H_2 -atmosphere. Note the 20 nm closed layer at the top of the starting layer.

troller serves for surface roughness investigation and a SEM/FIB Dual Beam Strata DB235 with DigiView 1612 CCD Camera (TSL Company) serves for EBSD analysis. The μ -Raman confocal spectroscopy setup consists of a Impex-MSL50 diode-pumped solid-state laser with a wavelength of 532 nm, whose beam is focused using an objective OBJ Plan SL 100x (Mitutoyo). The scattered light after interaction with the sample is coupled with a monochromator Holospec f/1.8i (KOSI) and detected with a CCD Camera (Andor Newton).

B.2 Porous double layer formation and characterization

The PSI process ensures a layer transfer on (100) Si substrates and is highly interesting for the space industry. However, there are some drawbacks for the application of the PSI process to the epitaxial growth of III-V compounds on Si (100) substrates: The 4 % large lattice mismatch between GaAs and Si, the large thermal expansion coefficient difference of $3.1 \cdot 10^{-6} K^{-1}$, and the incompatibility of polar and nonpolar materials. Most of these obstacles are eliminated by the utilization of Si substrates with a miscut of 2-6° off oriented towards (111), which avoids the formation of anti-phase domains and boundaries that are caused by the nonpolarity of Si and the lattice mismatch. High quality III-V compound epitaxial growth is hence possible on such substrates. The orientation miscut shows a step-like shaped surface. This substrates are hence interesting due to their potential applications in the space and concentrator solar cells industry.

Mesoporous Si double layer formation is investigated on substrates with an orientation of (100) with a miscut of 6° off towards (111). Figure B.1 shows a reorganized porous double layer after lift-off formed on a 4 inch wafer with orientation (100) with 6° off towards (111). The porous Si stack has a thickness of about 1.2 μm and consists

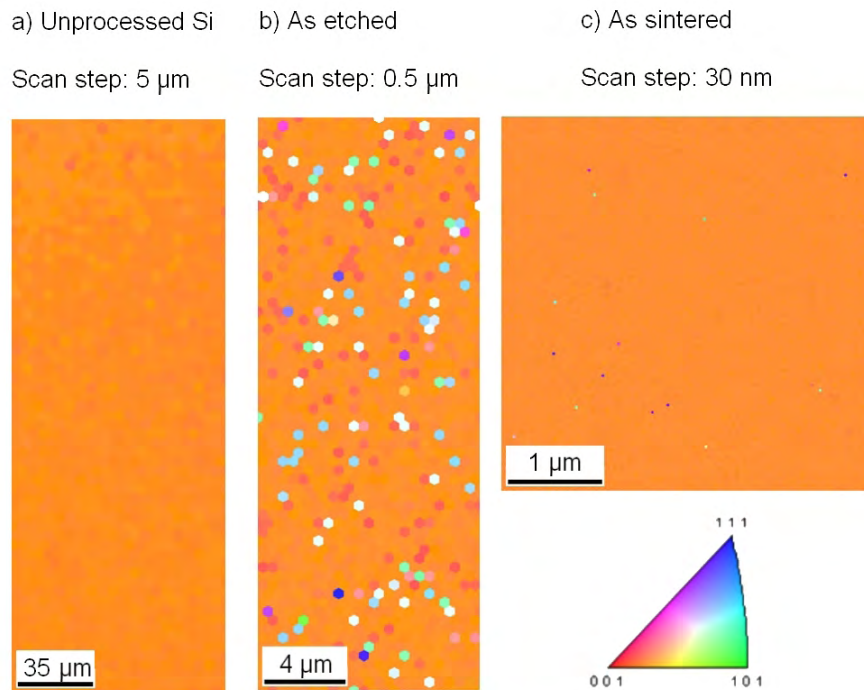


Figure B.2: EBSD analysis of the Si surface a) before etching, b) porous silicon, c) after sintering. Note that the scan step and the scanned area vary for the different images.

of two layers with different porosities. The starting layer has a thickness of about 900 nm and is composed of micro- and mesopores with a porosity of 22 %. Porosities below 30 % are necessary for the starting layer in order to obtain porous reorganization and surface closure for the epitaxial growth. Low porosities improve the quality of the epitaxial layer. The separation layer has a thickness of about 370 nm and a porosity of 48 %. Porosities exceeding 40 % are desired for the bottom layer to allow separation of the epitaxial layer from the substrate, since the mechanical strength of the layer decreases with increasing porosity.

The sintering step is necessary for the reorganization of the porous layers that finally leads to a closed surface that is suitable for high-quality epitaxy. A 20 nm thick reorganized and closed layer appears at the top of the starting layer. Substrates are sintered in H_2 atmosphere because the hydrogen reduces oxides at the pore walls that would otherwise hinder porous reorganization by decreasing the mobility of the Si atoms [83].

EBSD measurements serve for investigating the crystal orientation of the substrate after all three steps of the PSI process in order to determine whether the crystal orientation varies after the electrochemical etching and the annealing steps. Figure B.2 shows EBSD mappings of the unprocessed polished Si wafers, as-etched porous Si, and sintered porous Si. Figure B.2.a shows a homogeneous colour distribution that implies that the orientation of the substrate is constant throughout the surface. Figure B.2.b shows the EBSD mapping after etching. The etched substrate has predominantly the same orientation as the unprocessed Si. However, points of different orientations

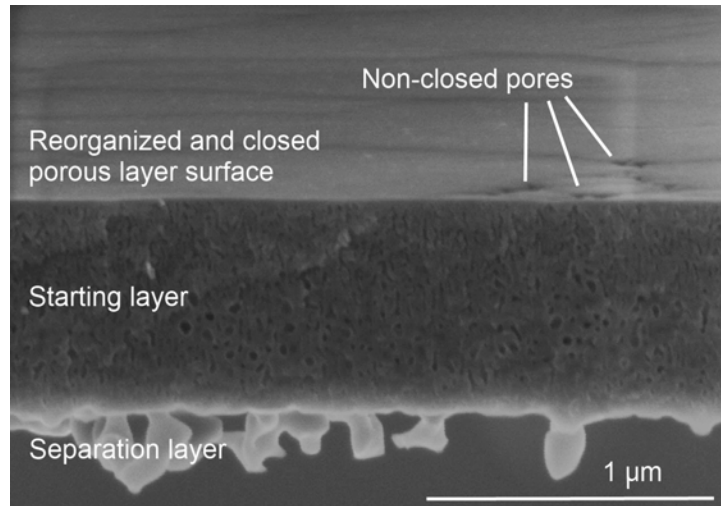


Figure B.3: SEM cross sectional image of a porous double layer with an accumulation of non-closed pores, responsible of local changes in the orientation in Figure B.3.c.

are present at the surface. Figure B.2.c shows the substrate orientation after etching and sintering. The predominant colour in all figures confirms that the orientation has not varied and only very few points of different orientation appear. The pole figures of each measurement additionally confirm that the substrate orientation is (100) with 6° off towards (111) in all cases.

The surface of the etched sample substantially differs from the unprocessed sample. Detailed analysis shows that the points of different orientations in Figure B.2.b are errors caused by optical effects due to pore accumulation: Pores distort the electron beam, showing an apparent change of the substrate orientation. However, the etching process only removes atoms selectively from the crystal structure and therefore does not change the crystal orientation. Very small points with different substrate orientation are also present in Figure B.2.c. After sintering, the surface of the sample is closed. However, the reorganisation of the randomly arranged pores of different size can cause locally an open surface due to e.g. the lack of silicon. The electron beam is thus disturbed as shown in Figure B.2.b. Figure B.3 shows a tilted cross sectional image of a porous double layer after lift-off with local accumulations of non-closed pores.

μ -Raman confocal spectroscopy analysis gives additional information regarding the crystallinity of the Si wafer at different states of the PSI process. Figure B.4 shows the Raman shift of unprocessed Si (continuous line), porous Si (dotted line), and reorganized porous Si (dashed line). Characteristic transverse-optical (TO) and longitudinal-optical (LO) phonon modes are clearly identifiable at 301 cm^{-1} and 522 cm^{-1} respectively. Native oxide formation after sample processing causes the peak in the 940-980 cm^{-1} range.

Figure B.5.a shows a detailed analysis of the TO mode of Si at 301 cm^{-1} . Unprocessed Si shows the highest intensity signal. The intensity of the signal significantly decreases for the electrochemically etched porous silicon, but there is not a Raman shift observable. The sample after the annealing step also presents a peak at 301 cm^{-1} . The intensity increases substantially in comparison to the porous silicon sample although it remains at a lower level than unprocessed silicon, pointing out that the reorganization

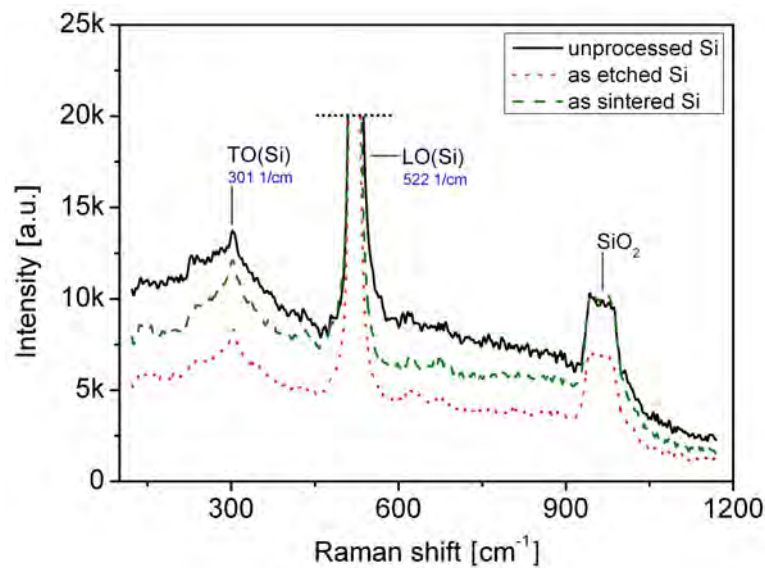


Figure B.4: Raman shift of unprocessed Si, porous Si, and reorganized porous Si. The black line S1 is related to unprocessed silicon. The red dotted line S2 is related to porous etched silicon. The green dashed line S3 is related to sintered silicon.

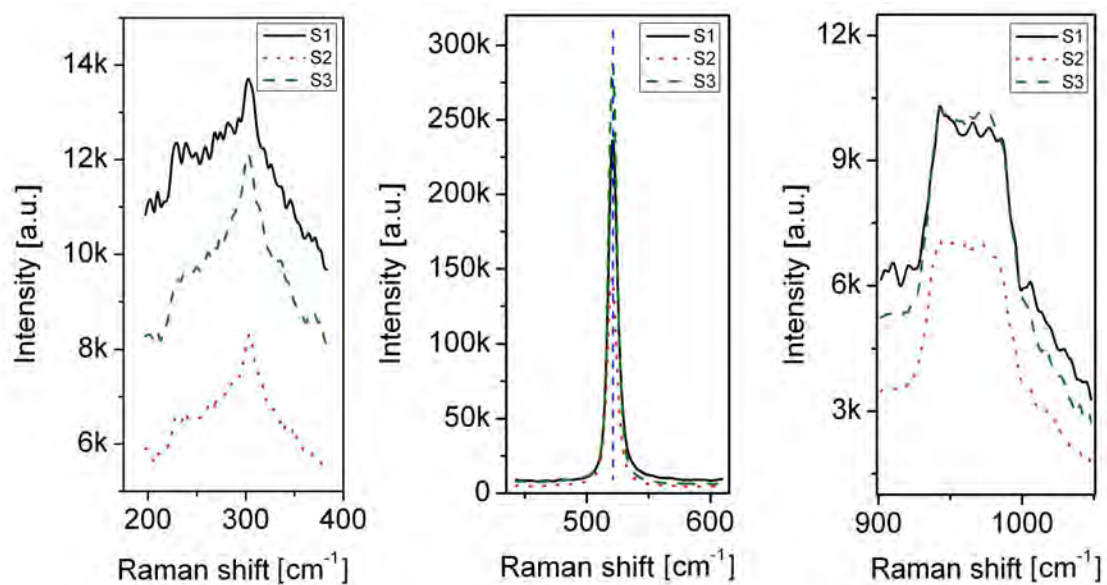


Figure B.5: Detailed μ -Raman shift analysis of important peaks. The black line S1 represents unprocessed silicon, the red dotted line S2 represents porous etched silicon, and the green dashed line S3 represents sintered silicon.

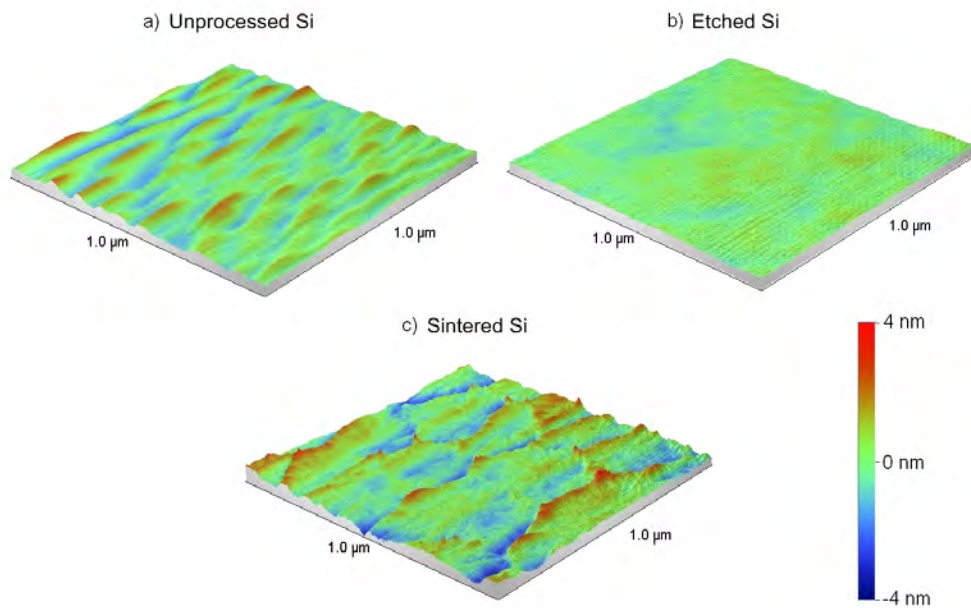


Figure B.6: Surface AFM scans of Si wafers a) before etching, b) porous silicon c) after sintering. Note that the scale varies in a range of -4 nm to $+4 \text{ nm}$ and the scans have an area of $1 \text{ } \mu\text{m}^2$.

does not decrease substantially the quality of the layer and no mechanical stress and amorphous phases appear. Figure B.5.b is related to the LO mode of silicon at 522 cm^{-1} . No peak shift is either observed in this case. The intensity of sintered silicon exceeds the intensity of porous etched silicon, confirming thus that the reorganization increases the intensity and therefore the quality of the chemically etched porous layer. Finally, Figure B.5.c is related to the SiO_2 peak. The intensities of both unprocessed and sintered silicon are similar and once again, higher than the intensity of etched silicon.

Figure B.6 shows surface AFM scans of unprocessed Si, porous Si, and sintered Si and the colour scale varying in a range of -4 nm to $+4 \text{ nm}$. Figure B.6.a shows the surface of unprocessed silicon. The surface has the characteristic step-like shape of substrates with miscut, with an average height roughness of 0.55 nm and a maximum height difference of 4.90 nm . The waves have a maximum height of 4 nm and are up to 100 nm large. Figure B.6.b shows the mapping of an as-etched surface. The mean surface height roughness is 0.27 nm and has a maximum height difference of 2.45 nm . The mean surface height roughness decreases after etching due to the typical electropolishing step prior to porous Si formation. The step-like surface becomes first electropolished. Afterwards, porous formation takes place and a mesoporous layer covers the surface of the substrate. Single mesopores are not observable in Figure B.6.b due to the high pore density. The lateral resolution hence diminishes and the surface has a flat appearance. Figure B.6.c shows the surface after etching and annealing. The surface has steps of the same shape as the unprocessed polished samples. The maximum height difference is 7.93 nm . The steps have a size in the $50\text{-}400 \text{ nm}$ range, thus larger than unprocessed. The average height roughness increased up to 0.78 nm .

The unprocessed sample has a wavy-shaped surface, characteristic of substrates with orientation miscut. After etching, the surface roughness decreases caused by the nucleation phase prior to porous formation. The surface becomes electropolished until pore formation starts, causing the wavy surface to disappear. The porous layer has a much flatter surface than unprocessed silicon and a lowered average surface height roughness. The annealing step causes the atoms to reorganize into a configuration with lower surface energy. The mean roughness hence increases and the surface rearranges into a step-like shape similar to unprocessed silicon with the same orientation of the starting substrate. The surface roughness of sintered samples is acceptable for an epitaxial growth of III-V compounds with comparable quality to unprocessed Si, with the advantage that the porous double layers allow detachment.

B.3 Summary and conclusions to Appendix B

Uniform and reproducible thick mesoporous double layers form on (100) substrates with 6° miscut towards (111) by means of electrochemical etching in ethanoic-based HF electrolytes. The 6° off orientation of the substrate is preserved after each step as measured by EBSD. μ -Raman confocal spectroscopy analysis does not show any peak shift, hence confirming that the PSI process does not substantially affect the quality of the substrate. The intensity of the Raman lines varies throughout the PSI process, decreasing after etching and increasing after subsequent annealing. AFM measurements show that the mean surface roughness decreases from 0.55 nm to 0.27 nm after etching due to electropolishing prior to porous formation. The reorganized porous layer shows an only slightly increased average surface roughness of 0.78 nm, which is acceptable for epitaxial growth. The preservation of the orientation and surface quality as well as reproducible layer transfer opens a new possibility of applying a layer transfer process of III-V compounds based on mesoporous Si with 6° off miscut towards (111).

Appendix C

Mixture of electrolytes

This appendix describes the procedure to obtain the electrolyte concentration desired for the experimental work. All the concentration values presented in this text are given in weight percentage. Electrolyte solutions are commonly prepared by diluting highly concentrated acids like hydrofluoric acid (40 wt. % or 50 wt. %) or hydrochloric acid (37.5 wt. %) in water, wetting agents, or organic compounds. Wetting agents are typically ethanol ($\text{CH}_3\text{CH}_2\text{OH}$) or acetic acid (CH_3COOH). The wetting agent increases the wettability of the substrate, helping thus to remove hydrogen bubbles evolving from the substrate during the dissolution process. Ethanoic solutions increase the depth uniformity of porous layers because ethanol molecules infiltrate into pores and homogenize porous formation. Dimethylformamide (DMF, $\text{C}_3\text{H}_7\text{NO}$) or dimethyl sulfoxide (DMSO, $\text{C}_2\text{H}_6\text{OS}$) serve as organic solvents and are used for macropore formation.

The concentration values are converted to volume values by preparing the electrolyte solutions in order to simplify the experimental work. Following equations serve to determine the amount of solvent needed to obtain the desired concentration assuming that the volume variation caused by the mixture of acid and solvent is negligible. c_{acid} [%] represents the starting acid concentration, c [%] is the final concentration of the electrolyte, xx [kg] is the amount of acid (in weight), yy [kg] is the amount of solvent (in weight), ρ_{acid} [$\frac{g}{cm^3}$] is the acid's mass density, and finally ρ_{water} [$\frac{g}{cm^3}$] is the water's mass density, which is equal to $1 \frac{g}{cm^3}$. Hydrofluoric acid's mass density is equal to $1.16 \frac{g}{cm^3}$ according to supplier's indications.

$$c = \frac{c_{acid} \cdot xx}{xx + yy} = \frac{c_{acid} \cdot \rho_{acid} \cdot x}{\rho_{acid} \cdot x + \rho_{water} \cdot y} = \frac{c_{acid}}{1 + \frac{\rho_{water} \cdot y}{\rho_{acid} \cdot x}} \quad (\text{C.1})$$

$$\frac{x}{y} = \frac{\rho_{water}}{\rho_{acid} \cdot \left(\frac{c_{acid}}{c} - 1 \right)} \quad (\text{C.2})$$

Bibliography

- [1] M. Meusel, W. Bensch, T. Bergunde, R. Kern, V. Khorenko, W. Köstler, G. La Roche, T. Torunski, W. Zimmermann, G.F.X. Strobl, W. Guter, M. Hermle, R. Hoheisel, G. Siefer, E. Welser, F. Dimroth, A. W. Bett, W. Geens, C. Baur, S. Taylor, G. Hey, Development and Production of European III-V Multi-Junction Solar Cells, in *Proceedings of the 22nd European Photovoltaic Solar Energy Conference*, (WIP, Milano, 2007), pp. 16-21.
- [2] J. F. Geisz, S. Kurtz, M. W. Wanlass, J. S. Ward, A. Duda, D. J. Friedman, J. M. Olson, W. E. McMahon, T. E. Moriarty, and J. T. Kiehl, High-efficiency GaInP/GaAs/InGaAs triple-junction solar cells grown inverted with a metamorphic bottom junction, *Appl. Phys. Lett.* **91**, 023502 (2007).
- [3] R. Brendel, A novel process for ultrathin monocrystalline silicon solar cells on glass, in *Proceedings of the 14th European Photovoltaic Solar Energy Conference*, (WIP, Barcelona, 1997), pp. 1354-1357.
- [4] H. C. Choi and J. Buriak, Preparation and Functionalization of Hydride Terminated Porous Germanium, *Chem. Comm.*, pp. 1669-1670 (2000).
- [5] J. Buriak, Organometallic Chemistry on Silicon and Germanium Surfaces, *Chem. Rev.* **102**, pp. 1271-1308 (2002).
- [6] J. Shieh, H. L. Chen, T. S. Ko, H. C. Cheng, and T. C. Chu, Nanoparticle-Assisted Growth of Porous Germanium Thin Films, *Adv. Mater.* **16**, No. 13, pp. 1121-1124 (2004).
- [7] L. K. van Vugt, A. F. van Driel, R. W. Tjerkstra, L. Bechger, W. L. Vos, D. Vanmaekelbergh, and J. J. Kelly, Macroporous germanium by electrochemical deposition, *Chem. Comm.*, pp. 2054-2055 (2002).
- [8] G. Flamand, J. Poortmans, and K. Dessein, Formation of porous Ge using HF-based electrolytes, *Phys. Stat. Sol. (C)* **2**, No. 9, pp. 3242-3247 (2005).
- [9] S. Langa, M. Christophersen, J. Carstensen, I. M. Tiginyanu, and H. Föll, Electrochemical pore etching in Ge, *Phys. Stat. Sol. (A)* **195**, pp. R4-R6 (2003).
- [10] S. Langa, J. Carstensen, M. Christophersen, K. Steen, S. Frey, I. M. Tiginyanu, and H. Föll, Electrochemical pore etching in Ge, *J. Electrochem. Soc.* **152**, (8), pp. C525-C531 (2005).

- [11] S. Langa, J. Carstensen, I. M. Tiginyanu, and H. Föll, Nucleation and growth of macro pores on (100) n-type Ge, *Phys. Stat. Sol. (C)* **2**, No. 9, pp. 3237-3242 (2005).
- [12] H. Föll, J. Carstensen, and S. Frey, Porous and Nanoporous Semiconductors and Emerging Applications, *J. of Nanomaterials* (**1**), pp. 1-10 (2006).
- [13] C. Fang, H. Föll, and J. Carstensen, Long Germanium Nanowires Prepared by Electrochemical Etching, *Nano Letters* **6**, No. 7, pp. 1578-1580 (2006).
- [14] C. Fang, H. Föll, and J. Carstensen, Electrochemical pore etching in germanium, *J. Electroanal. Chem.* **589**, pp. 259-288 (2006).
- [15] C. Fang, H. Föll, J. Carstensen, and S. Langa, Electrochemical pore etching in Ge - An overview, *Phys. Stat. Sol. (A)* **204**, No. 5, pp. 1292-1296 (2007).
- [16] D. Sun, A. Riley, A. Cadby, E. Richman, S. Korlann, and S. Tolbert, Hexagonal nanoporous germanium through surfactant-driven self-assembly of Zintl clusters, *Nature* **441**, pp. 1126-1130 (2006).
- [17] G. Armatas and M. Kanatzidis, Mesostructured germanium with cubic pore symmetry, *Nature* **441**, pp. 1122-1125 (2006).
- [18] G. S. Armatas and M. G. Kanatzidis, High-Surface-Area Mesoporous Germanium from Oxidative Polymerization of the Deltahedral $[\text{Ge}_9]^{4-}$ Cluster: Electronic Structure Modulation with Donor and Acceptor Molecules, *Adv. Mat.* **20**, 3, pp. 546-550 (2008).
- [19] G. S. Armatas and M. G. Kanatzidis, Mesoporous germanium-rich chalcogenido frameworks with highly polarizable surfaces and relevance to gas separation, *Nature Materials* **8**, pp. 217-222 (2009).
- [20] C. Jing, C. Zhang, X. Zang, W. Zhou, W. Bai, T. Lin, and J. Chu, Fabrication and characteristics of porous germanium films, *Sci. Technol. Adv. Mater.* **10**, 065001 (2009).
- [21] E. Garralaga Rojas, H. Plagwitz, B. Terheiden, J. Hensen, C. Baur, G. La Roche, G. F. X. Strobl, and R. Brendel, Mesoporous Germanium Formation by Electrochemical Etching, *J. Electrochem. Soc.* **156**, 8, pp. D310-D313 (2009).
- [22] E. Garralaga Rojas, B. Terheiden, H. Plagwitz, J. Hensen, C. Baur, G.F.X. Strobl, and R. Brendel, Formation of Mesoporous Germanium Double Layers by Electrochemical Etching for Layer Transfer Processes, *Electrochem. Comm.* **12**, 2, pp. 231-233 (2010).
- [23] E. Garralaga Rojas, B. Terheiden, H. Plagwitz, J. Hensen, J. Carstensen, H. Föll, and R. Brendel, A Model Describing Anodic Dissolution and Formation of Mesoporous p-Type Ge in Highly Concentrated HF Electrolytes, (2010), to be published.

- [24] E. Garralaga Rojas, J. Hensen, C. Baur, and R. Brendel, Sintering and Reorganization of Electrochemically Etched Mesoporous Germanium Layers in Various Atmospheres, *Sol. Ener. Mat. Sol. Cells*, **95**, pp. 292-295 (2011).
- [25] S. M. Sze, *Semiconductor Devices Physics and Technology*, (Wiley, New York, 2001).
- [26] S. M. Sze and Kwok K Ng, *Physics of Semiconductor Devices*, Wiley, New York (2006).
- [27] S. R. Morrison, *Electrochemistry at Semiconductor and Oxidized Metal Electrodes*, (Plenum Press, New York, 1980)
- [28] C. Hamann, W. Vielstich, *Elektrochemie*, ISBN-13: 978-3-527-31068-5 (Wiley-VCH, Weinheim, 2005)
- [29] A. Goetzberger, J. Knobloch, and B. Voss, *Crystalline Silicon Solar Cells: Technology and Systems Applications*, Wiley (1998).
- [30] H. von Helmholtz, Studien über elektrische Grenzschichten, *Wied. Ann.* **7**, 337 (1879).
- [31] L. G. Gouy, Sur la constitution de la charge à la surface d' un électrolyte, *Compt. Rend.* **149**, 654 (1909).
- [32] D. L. Chapman, A contribution to the theory of electrocapillarity, *Phil. Mag.* **25**, 475 (1913).
- [33] O. Stern, Zur Theorie der elektrischen Doppelschicht, *Z. Elektrochemie* **30**, 508 (1924).
- [34] A. Uhlir Jr., Electrolytic Shaping of Germanium and Silicon, *Bell System Tech. J.* **35**, pp. 333-347 (1956).
- [35] L. T. Canham, Silicon quantum wire array fabrication by electrochemical and chemical dissolution of wafers, *Appl. Phys. Lett.* **57**, pp. 1046-1048 (1990).
- [36] L. T. Canham and A. J. Groszek, Characterization of microporous Si by flow calorimetry: Comparison with hydrophobic SiO₂ molecular sieve, *J. Appl. Phys.* **72**, pp. 1558-1565 (1992).
- [37] H. Tayanaka and T. Matsushita, Separation of thin epitaxial Si films on porous Si for solar cells, in *Proceedings of the 6th Sony Research Forum*, 556 (1996).
- [38] J. Rouquerol, D. Avnir, C. W. Fairbridge, D. H. Everett, J. H. Haynes, N. Pernicone, J. D. F. Ramsay, K. S. W. Sing, K. K. Unger, Recommendations for the characterization of porous solids, *Pure Appl. Chem.* **66**, pp. 1739-1758 (1994).
- [39] A. Wolf, Sintered Porous Silicon - Physical Properties and Applications for Layer-Transfer Silicon Thin-Film Solar Cells, PhD Thesis, Leibniz University of Hannover (2007).

- [40] V. Lehmann, *Electrochemistry of Silicon*, Wiley-VCH, Weinheim, Germany (2002).
- [41] V. Lehmann, R. Stengl, and A. Luigart, On the morphology and the electrochemical formation mechanism of mesoporous silicon, *Materials Science and Engineering B* **69-70**, pp. 11-22 (2000).
- [42] H. Föll, Properties of silicon-electrolyte junctions and their application to silicon characterization, *Appl. Phys. A* **53**, pp. 8-19 (1991).
- [43] J. Carstensen, R. Prange, G. S. Popkirov, and H. Föll, A model for current oscillations in the Si-HF system based on a quantitative analysis of current transients, *Appl. Phys. A* **67**, pp. 459-467 (1998).
- [44] J. Carstensen, R. Prange, and H. Föll, A Model for Current-Voltage Oscillations at the Silicon Electrode and Comparison with Experimental Results, *J. Electrochem. Soc.* **146**, 3, pp. 1134-1140 (1999).
- [45] V. Lehmann and U. Gösele, Porous silicon formation: A quantum wire effect, *Appl. Phys. Lett.* **58**, pp. 856-858 (1991).
- [46] S. Ottow, G. S. Popkirov, and H. Föll, Determination of flat-band potentials of silicon electrodes in HF by means of ac resistance measurements, *J. Electroanal. Chem.* **455**, pp. 29-37 (1998).
- [47] V. Lehmann and R. Rönnebeck, The physics of macropore formation in low-doped p-type silicon, *J. Electrochem. Soc.* **146**, pp. 2968-2975 (1999).
- [48] V. Lehmann, The physics of macropore formation in low-doped n-type silicon, *J. Electrochem. Soc.* **140**, pp. 2836-2843 (1993).
- [49] V. Lehmann and U. Grüning, The limits of macropore array formation, *Thin Solid Films* **297**, pp. 13-17 (1997).
- [50] X. G. Zhang, Mechanism of pore formation on n-type silicon, *J. Electrochem. Soc.* **138**, pp. 3750-3756 (1991).
- [51] Y. H. Ogata, N. Yoshimi, R. Yasuda, T. Tsuboi, T. Sakka, and A. Otsuki, Structural change in p-type porous silicon by thermal annealing, *J. Appl. Phys.* **90**, pp. 6487-6492 (2001).
- [52] J. E. Geguzin, *Physik des Sinterns*, VEB Deutscher Verlag für Grundstoffindustrie, Leipzig (1973).
- [53] G. Müller and R. Brendel, Simulated annealing of porous Si, *Phys. Stat. Sol. (A)* **182**, 1, pp. 313-318 (2000).
- [54] G. Müller, M. Nerding, N. Ott, H. P. Strunk, and R. Brendel, Sintering of porous Si, *Phys. Stat. Sol. (A)* **197**, 1, pp. 83-87 (2003).

- [55] T. Yonehara, K. Sakaguchi, and N. Sato, Epitaxial layer transfer by bond and etch back of porous Si, *Appl. Phys. Lett.* **64**, 16, pp. 2108-2110 (1994).
- [56] G. Kuchler, D. Scholten, G. Müller, J. Krinke, R. Auer, and R. Brendel, Fabrication of textured monocrystalline Si-films using the porous silicon (PSI)-process, in *Proceedings of the 16th European Photovoltaic Solar Energy Conference*, (WIP, Glasgow, 2000), pp. 1695-1698.
- [57] R. Brendel, R. Auer, K. Feldrapp, D. Scholten, M. Steinhof, R. Hezel, and M. Schulz, Crystalline thin-film Si cells from layer transfer using porous Si (PSI-Process), in *Proceedings of the 29th IEEE Photovoltaic Specialists Conference*, (IEEE, New Orleans, 2002) pp. 86-89.
- [58] K. Feldrapp, R. Horbelt, R. Auer, and R. Brendel, Thin-film (25.5 μm) solar cells from layer transfer using porous silicon with 32.7 mA/cm^2 , *Prog. Photovolt. Res. Appl.* **11**, pp. 105-112 (2003).
- [59] R. Horbelt, B. Terheiden, R. Auer, and R. Brendel, Manifold use of growth substrate in the Porous Silicon - layer transfer - process, in *Proceedings of the 31st IEEE Photovoltaic Specialists Conference*, (IEEE, Florida, 2005) pp. 1193-1196.
- [60] B. Terheiden, R. Horbelt, and R. Brendel, Thin-film solar cells and modules from the porous Si process using 6" Si substrates, in *Proceedings of the 21st European Photovoltaic Solar Energy Conference*, (WIP, Dresden, 2006), pp. 742-745.
- [61] P. J. Goodhew, J. Humphreys, and R. Beanland, Electron Microscopy and Analysis, Third Edition, (Taylor & Francis, London, 2000).
- [62] L. Reimer, Scanning Electron Microscopy: Physics of Image Formation and Microanalysis (Springer Series in Optical Sciences), (Springer, Heidelberg, 1998).
- [63] R. W. Wild, P. E. J. Flewitt, Physical Methods for Materials Characterization, (IOP Publishing Ltd, London, 2003).
- [64] F. Jirsa, Über die anodische Auflösung des Germaniums, *Z. Anorg. Chem.*, **268**, 84 (1952).
- [65] C. Garrett and W. Brattain, Physical Theory of Semiconductor Surfaces, *Phys. Rev.* **99**, 2, pp. 376-387 (1955).
- [66] W. Brattain and C. Garrett, Experiments on the Interface between Germanium and Electrolyte, *Bell Syst. Techn. J.* **34**, 129 (1955).
- [67] D. R. Turner, Anode Behavior of Germanium, *J. Electrochem. Soc.* **103**, pp. 252-256 (1956).
- [68] F. Beck and H. Gerischer, Zum Mechanismus der anodischen Auflösung von Germanium in alkalischer Lösung, *Z. Elektrochem.* **63**, pp. 500-510 (1959).
- [69] F. Beck and H. Gerischer, Redoxvorgänge an Germanium-Elektroden, *Z. Elektrochem.* **63**, pp. 943-950 (1959).

- [70] P. F. Schmidt, and C. Church, Recombination Radiation from an N-Type Germanium Cathode in Heavy Water, *J. Electrochem. Soc.* **108**, 3, pp. 296-296 (1961).
- [71] D. R. Turner, Electrochemical Reactions at Semiconductor Electrodes, in *Symposium on Electrochemical Processes, Fuel Chemistry Division of the American Chemical Society*, Spring Meeting in Miami, pp. 19-22 (1967).
- [72] M. I. J. Beale, J. D. Benjamin, M. J. Uren, N. G. Chew, and A. G. Cullis, An experimental and theoretical study of the formation and microstructure of porous silicon, *J. Cryst. Growth* **73**, pp. 622-636 (1985).
- [73] H. Unno, K. Imai, and S. Muramoto, Dissolution reaction effect on porous-silicon density, *J. Electrochem. Soc.* **134**, pp. 645-648 (1987).
- [74] D. R. Lide, Editor, *CRC Handbook of Chemistry and Physics* CRC Press, Boca Raton, FL (2005).
- [75] S. M. Sze, *Physics of semiconductor devices*, (Wiley, New York, 2001).
- [76] A. Froitzheim, R. Stangl, M. Kriegel, L. Elstner, W. Fuhs, in *Proceedings of the 3rd World Conference on Photovoltaic Energy Conversion*, (IEEE, Osaka, 2003), pp. 1556-1559.
- [77] M. Pourbaix, Atlas of Electrochemical Equilibria in Aqueous Solutions, pp. 464-474, Pergamon Press Ltd. (1966).
- [78] P. W. Loscutoff and S. T. Bent, Reactivity of the Germanium Surface: Chemical Passivation and Functionalization, *Annu. Rev. Phys. Chem.* **57**, pp. 467-495 (2006).
- [79] A. Dimoulas, E. Gusev, P. C. McIntyre, M. Heyns (Eds.), Advanced Gate Stacks for High-Mobility Semiconductors Series: Springer Series in Advanced Microelectronics, Vol. 27, XXII, 383 pp. 292 illus. (2007), Hardcover, ISBN: 978-3-540-71490-3.
- [80] M. I. J. Beale, N. G. Chew, M. J. Uren, A. G. Cullis, and J. D. Benjamin, Microstructure and formation mechanism of porous silicon, *Appl. Phys. Lett.* **46**, pp. 86-88 (1985).
- [81] O. Bisi, S. Ossicini, and L. Pavesi, Porous silicon: A quantum sponge structure for silicon based optoelectronics, *Surf. Sci. Rep.* **38**, pp. 1-126 (2000).
- [82] P. M. Hoffmann, I. E. Vermeir, and P. C. Searson, Electrochemical etching of n-type silicon in fluoride solutions, *J. Electrochem. Soc.* **147**, pp. 2999-3002 (2000).
- [83] R. Herino, A. Perio, K. Barla, and G. Bomchil, Microstructure of porous silicon and its evolution with temperature, *Mater. Lett.* **2**, pp. 519-523 (1984).
- [84] D. J. Eaglesham, A. E. White, L. C. Feldman, N. Moriya, and D. C. Jacobson, Equilibrium shape of Si, *Phys. Rev. Lett.* **70**, pp. 1643-1646 (1993).

- [85] N. Ott, M. Nerding, G. Müller, R. Brendel and H. P. Strunk, Structural changes in porous silicon during annealing, *Phys. Stat. Sol. (A)* **197**, 1, pp. 93-97 (2003).
- [86] G. Kartopu, V. A. Karavanskii, U. Serincan, R. Turan, R. E. Hummel, Y. Ekinci, A. Gunnaes, and T. G. Finstad, Can chemically etched germanium or germanium nanocrystals emit visible photoluminescence?, *Phys. Stat. Sol. (A)* **202**, No. 8, pp. 1472-1476 (2005).
- [87] G. Kartopu, S. C. Bayliss, V. A. Karavanskii, R. J. Curry, R. Turan, and A. V. Sapelkin, On the origin of the 2.2-2.3 eV photoluminescence from chemically etched germanium, *Jour. of Luminescence* **101**, pp. 275-283 (2003).
- [88] V. A. Karavanskii, A. A. Lomov, A. G. Sutyryn, V. A. Bushuev, N. N. Loikho, N. N. Melnik, T. N. Zavaritskaya, and S. Bayliss, Observation of nanocrystals in porous stain-etched germanium, *Phys. Stat. Sol. (A)* **197**, No. 1, pp. 144-149 (2003).
- [89] A. A. Lomov, V. A. Bushuev, V. A. Karavanskii, and S. Bayliss, Characterization of the structure of porous germanium layers by high-resolution X-ray diffractometry, *Crystallography Reports* **48**, No. 2, pp. 326-334 (2003).
- [90] V. A. Karavanskii, A. A. Lomov, A. G. Sutyryn, V. A. Bushuev, N. N. Loikho, N. N. Melnik, T. N. Zavaritskaya, and S. Bayliss, Raman and X-ray studies of nanocrystals in porous stain-etched germanium, *Thin Solid Films* **437**, pp. 290-296 (2003).
- [91] S. Wen, J. Jan, M. Lance, J. Bentley, and G. Pharr, Nanoidentation-Induced Phase Transformations in Ge Studied by Electron Microscopy and Raman Spectroscopy, *Microsc. Microanal.* **11**, 2, pp. 792-793 (2005).
- [92] G. Oskam, A. Natarajan, P. C. Searson, and F. M. Ross, The formation of porous GaAs in HF solutions, *Appl. Surf. Sci.* **119**, pp. 160-168 (1997).
- [93] D. J. Lockwood, P. Schmuki, H. J. Labbé, and J.W. Fraser, Optical properties of porous GaAs, *Physica E* **4**, pp. 102-110 (1999).
- [94] L. Beji, L. Sfaxi, B. Ismail, S. Zghal, F. Hassen, and H. Maaref, Morphology and photoluminescence studies of electrochemically etched heavily doped p-type GaAs in HF solution, *Microelectron. J.* **34**, 10, pp. 969-974 (2003).
- [95] L. Beji, A. Missaoui, A. Fouzri, H. Ben Ouada, H. Mareef, and A. Bouazizi, Nanostructurale nature of the porous GaAs layer formed on p^+ -GaAs substrate by electrochemical anodization, *Microelectron. J.* **37**, 8, pp. 783-785 (2006).
- [96] L. Beji, L. Sfaxi, H. Ben Ouada, and H. Maaref, Investigation of porous GaAs layers formed on n^+ -type GaAs by electrochemical anodization in HF solution, *Phys. Stat. Sol. (A)* **202**, No. 1, pp. 65-71 (2005).
- [97] L. Beji, T. Ben Jomaa, Z. Harrabi, A. Laribi, A. Missaoui, A. Bouazizi, DC and AC electrical characteristics of porous GaAs/ p^+ -GaAs heterostructure, *Vacuum* **80**, 5, pp. 480-487 (2006).

-
- [98] S. Ben Khalifa, B. Gruzza, C. Robert-Goumet, L. Bideux, G. Monier, F. Saidi, R. M'Ghaieth, M. Hjiri, R. Hamila, F. Hassen, H. Maaref, G. Bremond, and L. Bèji, Study of porous III-V semiconductors by electron spectroscopies (AES and XPS) and optical spectroscopy (PL): Effect of ionic bombardment and nitridation process, *Surf. Sci.* **601**, 18, pp. 4531-4535 (2007).
- [99] S. Ben Khalifa, B. Gruzza, C. Robert-Goumet, G. Bremond, M. Hjiri, F. Saidi, L. Bideux, L. Bèji, and H. Maaref, Morphology and optical properties of p-type porous GaAs (100) layers made by electrochemical etching, *J. Lumin.* **128**, 10, pp. 1611-1616 (2008).
- [100] P. Schmuki, L. E. Erikson, D. J. Lockwood, J. W. Fraser, G. Champion, and H. J. Labbé, Formation of visible light emitting porous GaAs micropatterns, *Appl. Phys. Lett.* **72**, No. 9, pp. 1039-1041 (1998).
- [101] H. Föll, S. Langa, J. Carstensen, M. Christophersen, and I. M. Tiginyanu, Pores in III-V semiconductors, *Adv. Mater.* **15**, No. 3, pp. 183-189 (2003).

List of publications

Journal papers

1. E. Garralaga Rojas, H. Plagwitz, B. Terheiden, J. Hensen, C. Baur, G. La Roche, G.F.X. Strobl, and R. Brendel, Mesoporous Germanium Formation by Electrochemical Etching, *J. Electrochem. Soc.* **156**, 8, pp. D310-D313 (2009).
2. E. Garralaga Rojas, B. Terheiden, H. Plagwitz, C. Hampe, D. Tutuc, R. Haug, and R. Brendel, Mesoporous GaAs Double Layers for Layer Transfer Processes, *Phys. Stat. Sol. (A)* **206**, No. 12, pp. 2872-2875 (2009).
3. E. Garralaga Rojas, B. Terheiden, H. Plagwitz, J. Hensen, C. Baur, G.F.X. Strobl, and R. Brendel, Formation of Mesoporous Germanium Double Layers by Electrochemical Etching for Layer Transfer Processes, *Electrochem. Comm.* **12**, 2, pp. 231-233 (2010).
4. E. Garralaga Rojas, J. Hensen, C. Baur, and R. Brendel, Sintering and Reorganization of Electrochemically Etched Mesoporous Germanium Layers in Various Atmospheres, *Sol. Ener. Mat. Sol. Cells*, **95**, pp. 292-295 (2011).
5. E. Garralaga Rojas, J. Hensen, J. Carstensen, H. Föll, and R. Brendel, Mesoporous Germanium Multilayers, *Phys. Stat. Sol. (C)* (2010), accepted for publication.
6. E. Garralaga Rojas, B. Terheiden, H. Plagwitz, J. Hensen, V. Wiedemeier, G. Berth, A. Zrenner, and R. Brendel, Lift-off of mesoporous layers on silicon substrates with 6° off, *Thin Solid Films* (2010), submitted.

Specialised Conferences

1. E. Garralaga Rojas, H. Plagwitz, C. Hampe, and R. Brendel, Formation of Mesoporous Gallium Arsenide for Lift-off Processes by Electrochemical Etching, in *Proceedings of the 34th IEEE Photovoltaic Specialists Conference*, Philadelphia, USA (IEEE, New York, 2009). Oral presentation.
2. E. Garralaga Rojas, B. Terheiden, J. Hensen, G.F.X. Strobl, W. Köstler, W. Zimmermann, H. Plagwitz, and R. Brendel, Formation of Mesoporous Germanium by Electrochemical Etching for Lift-Off Processes, *Proceedings of the 24th European Photovoltaic Solar Energy Conference*, pp. 684-687, Hamburg, Germany (WIP, Munich, 2009). Visual presentation.
3. E. Garralaga Rojas, H. Plagwitz, B. Terheiden, J. Hensen, C. Baur, G.F.X. Strobl, and R. Brendel, Mesoporous Germanium Double Layers by Electrochemical Etching for Lift-Off Processes, *19th International Photovoltaic Science and Engineering Conference*, Jeju, South Korea (2009). Oral presentation.

4. N.-P. Harder, E. Garralaga Rojas, T. Brendemühl, A. Merkle, V. Mertens, and R. Brendel, Development of Back-Contacted Solar Cells at the Institute for Solar Energy Research in Hamelin, *19th International Photovoltaic Science and Engineering Conference*, Jeju, South Korea (2009). Oral presentation.
5. E. Garralaga Rojas, J. Hensen, C. Baur, G.F.X. Strobl, and R. Brendel, Mesoporous Ge Layers by electrochemical etching for lift-off processes, *NanoDay 2009*, Hannover, Germany (2009). Visual presentation.
6. E. Garralaga Rojas, J. Hensen, H. Plagwitz, B. Terheiden, C. Baur, W. Köstler, G. La Roche, G.F.X. Strobl, and R. Brendel, Mesoporous Germanium Layers by Electrochemical Etching for Lift-Off Processes, in *Proceedings of the Photovoltaik Symposium zum 29. Tag der Niedersachsen*, (2009). Visual presentation.
7. E. Garralaga Rojas, J. Hensen, J. Carstensen, and R. Brendel, Mesoporous Germanium Multilayers, *7th International Conference on Porous Semiconductors - Science and Technology*, Valencia, Spain (2010). Oral presentation.
8. E. Garralaga Rojas, B. Terheiden, H. Plagwitz, J. Hensen, C. Baur, G.F.X. Strobl, and R. Brendel, Production of Low Weight Space Solar Cells by Applying a Layer Transfer Process from the Ge Growth Substrate, *1st Networking/Partnering Day*, European Space Agency - ESTEC, Noordwijk, the Netherlands (2010). Oral presentation.
9. E. Garralaga Rojas, J. Hensen, C. Baur, G.F.X. Strobl, and R. Brendel, Mesoporous Ge Layers by electrochemical etching for lift-off processes, *1st Networking/Partnering Day*, European Space Agency - ESTEC, Noordwijk, the Netherlands (2010). Visual presentation.

Awards

1. Best Poster Award at NanoDay 2009 in Hannover, Germany (2009)
2. SEMITool Award at the 7th International Conference on Porous Semiconductors - Science and Technology in Valencia, Spain (2010)

Scientific referee

1. Applied Physics Letters
2. Physica Status Solidi (A)
3. Journal of the Electrochemical Society

Patent applications

1. E. Garralaga Rojas, J. Hensen, B. Terheiden, H. Plagwitz, *Verfahren zum Herstellen eines Bauelementes, insbesondere einer Solarzelle, auf Basis einer Germaniumschicht*, 10 2009 004560.0.

2. E. Garralaga Rojas, J. Hensen, B. Terheiden, H. Plagwitz, C. Hampe, Verfahren zum Herstellen eines Bauelementes, insbesondere einer Solarzelle, auf Basis einer Halbleiterdünnschicht mit einem direkten Halbleiter, 10 2009 004559.7.
3. E. Garralaga Rojas, J. Hensen, B. Terheiden, H. Plagwitz, C. Hampe, Verfahren zum Herstellen eines Halbleiterbauelementes, insbesondere einer Solarzelle, auf Basis einer Germanium- oder Halbleiterdünnschicht mit einem direkten Halbleiter, 10 2009 018773.1.

Curriculum Vitae

Personal details

Name	Enrique José Garralaga Rojas
Adress	Vitoria nº 8, 4º Izda, 26005 Logroño (La Rioja), Spain
Date of birth	October 17 th , 1980 in Zaragoza, Spain
Citizenship	Spanish
Marital status	Single
Parents	Enrique Javier and M ^a del Carmen Esther

Qualifications

- 1986 - 1998** *High school*
Centro Sagrado Corazón in Logroño (La Rioja), Spain
- 1998 - 2004** *Licenciado en Ciencias Físicas* at Universidad de Zaragoza, Spain
Exchange student at Universität Paderborn, Germany
during the academic course 2003-2004
- 2004 - 2005** *MSc. Physik* at Universität Paderborn, Germany
Master thesis title: "Production of photonic structures by means of electron beam lithography"
- 2005 - 2006** *European MSc. in Renewable Energies*
Specialization in Photovoltaics
- Core provider: Universidad de Zaragoza, Spain
 - Specialisation provider: Northumbria University, UK
 - Research centre: ISFH, Germany
- Master thesis title: "Porous layer formation on Si and Ge wafers for thin-film solar cells from layer transfer processes"

2007 - 2010 *Doctoral work (Dr. -Ing.) in Engineering*

Technischen Fakultät Christian-Albrechts-Universität zu Kiel.

Work carried out at the ISFH, Germany (Jan07-Jul10).

Research internship at the Solar Generator Section of the European Space Agency (ESA) - ESTEC, Noordwijk, the Netherlands (May09-Nov09).

Doctoral thesis title: "Mesoporous Germanium Layer Formation by Electrochemical Etching".

Professional experience

2006 - now *TAGEX Technischer Handel GmbH & Co. KG*

Free-lance photovoltaics and solar thermal consultant.

Photovoltaic and Solar Thermal system design. Coordination of the solar section for the Spanish market.

2008 - now *Ingeniería e Instalaciones Vega S.L.P.*

Co-founder of the bureau of engineers. Responsible of solar thermal and photovoltaic business development.

2010 - now *Renewables Academy (RENAC) AG*

Free-lance lecturer of photovoltaic engineering courses.

Courses taught in Germany, Saudi Arabia, and Oman.

Thanks a lot!

Hereby I would like to thank all the people that have helped me to complete this work:

First I would like to acknowledge **Prof. Dr. Helmut Föll** for the supervision and correction of this thesis as well as for allowing me to finish my PhD studies in Kiel. Many thanks as well to **Prof. Dr. Rainer Adelung** and to **Prof. Dr. Lorenz Kienle** for the correction of my work and their participation in the evaluating commission.

I would like to express my sincere gratitude to **Prof. Dr.-Ing. Rolf Brendel** for the PhD position at the ISFH and his support for the completion of the work and his patient correction of my publications. I appreciate the support from **Dr. Barbara Terheiden** and **Dr. Heiko Plagwitz** during my staying at the ISFH. Their academic advice, constant encouragement, and magnificent direction helped me a lot during the first part of my PhD.

Many thanks as well to **Prof. Dr. Jan Schmidt** for inviting me to work at the ISFH and for offering me the PhD position. I would also like to thank **Dr. Carsten Hampe** for the good practical tips and ideas regarding GaAs, patents, and project management as well as interesting "scientific" discussions.

Particularly I want to render special thanks to my best work colleague: **Jan Hensen**. I want to thank you for the exceptional working atmosphere, for the nice time that we have spent together (in- and outside the photolithography room), the PSSST conference in Valencia, and for all the memories that I will always keep in mind!. Many thanks as well to **Bianca Gehring** for her valuable technical help and obviously to all the Silicon Thin-film Research Group members.

I would like to thank my office colleagues: **Tobi, Stefan, Till, Jan, Christian, Matthias, Florian, Ralph, and Sebastian** (the greatest fan of Dirk Nowitzki, the player who never won a title!) and obviously to the other PhD students and coworkers at the ISFH: **Felix, Rob, Christoph, David, Klaus, Michael, Ulli, Sonja, Marco, Stefan P., Tobi (laser fuzzi No. 1), Stefan E., Till (laser fuzzi No. 2), Peter E., Peter G. (laser fuzzi No. 3), Peter P., Karsten, Yu, Ralph, Christian, Yevgenya, Verena M., Verena S., Marita, Renate, Mirjam, Jörg, Florian, Matthias, Andi W., Martin W., Stefan B., Rene, Willy,...** and other ISFH members I do not mention by name. I do not want to finish this part without remembering the nice "Japan Research Group" in Fukuoka 2007: **Felix, Rob, Christoph, and Klaus**.

I specially appreciate the support of the spanish-speaking group at the ISFH: **Dr. Rafel Ferré and Prof. Dr. Juan Carlos Cedrón**, that helped me so much!. Many thanks to both of them and specially to **Rafa** for the nice time, coffees, and discussions (in Spanish) that we had about life, relationships, politics, work, Spain

(and Catalonia), and (only sometimes) about solar energy and PV. It has been a pleasure for me to meet you and I wish you all the best!

I really enjoyed my staying at the Solar Generator Section of the European Space Agency - ESTEC in the Netherlands, and that is thanks to **Dr. Carsten Baur**. I strongly appreciate your guidance during the PhD and the interesting discussions that we had in Noordwijk. I certainly have to thank specially to **Lothar Gerlach** for his courage in pushing new approaches and technologies in the solar space field. It has been a pleasure to learn from you!. Many thanks as well to **Dr. Mariel Triggianese** (my dear room colleague), **Sylvia Spanring**, and **Emilio Fernández** for their help and advices during my staying in ESTEC. Obviously, this acknowledgment would not be completed without my thanks to **Rubén, Itziar, Berta, Gonzalo, José Antonio, and Mamen** and all other Spanish ESTEC colleagues for their help, advices, and support during my staying at ESTEC.

I appreciate the support of the members of the "Chair for General Materials Science" of the Christian-Albrechts-Universität zu Kiel. Specially I want to thank **PD Dr. Jürgen Carstensen** for the help with paper correction and with the electrochemical etching setup. Many thanks as well to **Jörg Bahr, Emmanuel Ossei-Wusu, Dr. Ala Cojorcaru, Andreas Schütt**, and **Malte Leisner** for they support during my staying in Kiel and the PSST 2010 in Valencia.

Many thanks as well to the AZUR Space Solar Power GmbH team: **Dr. Gerhard Strobl, Günther La Roche, Dr. Wolfgang Köstler, Dr. Matthias Meusel, and Dr. Walter Zimmerman** for the pleasant co-work in the L-Quad project. Thanks as well to **Dr. Frank Dimroth** and his team from the FhG-ISE for the epitaxial growth on top of reorganized porous layers. I esteem the help of **Prof. Dr. Rolf Haug** and **Daniel Tutuc** from the Nanostructures group at the Leibniz Universität Hannover with AFM measurements and **Dr. -Ing. Flavio Soldera** from the Universität des Saarlandes for his help with the EBSD measurements. I also appreciate the help of **Dr. Gerhard Berth, Volker Wiedemeier**, and **Prof. Artur Zrenner** from the Nanostructure Optoelectronics group at the University of Paderborn for the Raman measurements.

Thanks a lot to my flat-mates (**Christian** and **Alex**) for their emotional support during these years. It has been a pleasure to have such a nice, different, and funny shared flat.

Finalmente, y ya en español, quiero dar las gracias a mi querida familia por ayudarme, apoyarme, guiarme y ser mi inspiración para completar este trabajo. Quiero dedicar este trabajo especialmente a mis padres (**Carmen** y **Enrique**), abuelos (**Carmen** y **Aquilino, Pilar** y **Enrique**), a mi hermana **Mamen** y al resto de mi familia por su cariño y amor, por su apoyo incondicional (antes y durante los estudios), por la paciencia, por la motivación que me han dado y por aceptar mi ausencia lejos de casa a lo largo de todos estos años de estancia en el extranjero.

Quiero también agradecer sinceramente a mi novia **Vera** su amor, el apoyo emocional y la paciencia que ha demostrado conmigo durante este periodo de mi vida tan centrado en el trabajo, consiguiendo que me sintiese como en casa pese a estar tan lejos.

Os agradezco mucho todos vuestros esfuerzos y paciencia conmigo. Sin vuestro amor, apoyo y motivación, todo ésto no hubiese sido posible y sin duda merecéis este título de doctorado mucho más que cualquier otra persona. ¡Muchísimas gracias por todo y espero que podamos disfrutarlo en compañía!.

Thank you all very much!!!

Statement

Hereby I certify that I have completed this work without unauthorized help.

Hameln, 31.07.2010

Enrique Garralaga Rojas